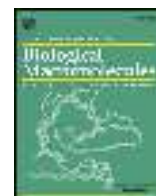


### List of Publications along with papers ( Any Two)

1. **Dugam Shailesh**, Jain R\*, Dandekar P\*, Silver nanoparticles loaded triple-layered cellulose-acetate based multifunctional dressing for wound healing, International Journal of Biological Macromolecules, Volume 276, Part 1, IF 7.7
2. Desai Ranjeet, Jaiswal Rahul, Manchekar Triveni, **Dugam Shailesh**, Jain R\*, Dandekar P\*, Enhancing monoclonal antibody stability during protein chromatography B using 2-methyl imidazolium dihydrogen phosphate, Journal of Chromatography B, Volume 1773, IF 3.21
3. Padwal Vijay, Narvekar Aditya, **Dugam Shailesh**, Pachpore Radhika, **Dandekar P\***, Jain R\*. Elucidating the role of 2-methyl imidazolium dihydrogen phosphate in preventing aggregation of Bevacizumab: a biophysical investigation, Journal of Molecular Liquids, 390, 122968, 2023. IF: 6.0
4. **Dugam Shailesh**, Nangare Sopan, Gore Anil, Wairkar Sarika, Patil Pramod, Choudary Latika, Jadhav Namdeo\*, Crystallinity modulated silk fibroin electrospun nanofibers based floating scaffold as a candidate for controlled release of felodipine, International Journal Polymeric Materials and Polymeric Biomaterials, 2022, vol. 71, no. 18, 1393–1406, if 3.2
5. **Dugam Shailesh**, Tade Rahul, Dhole Rani and Nangare Sopan \*, Emerging era of microneedle array for pharmaceutical and biomedical applications: recent advances and toxicological perspectives, Future Journal of Pharmaceutical Sciences (2021) 7:19, IF 2.6
6. Nangare Sopan, Vispute Yogita, Tade Rahul, **Dugam Shailesh**, Pravin Patil\*, Pharmaceutical applications of citric acid, Future Journal of Pharmaceutical Sciences (2021) 7:54, IF 2.6
7. **Dugam Shailesh**, Nangare Sopan, Patil Parvin, Jadhav Namdeo\* Carbon dots: A novel trend in pharmaceutical applications, Annales Pharmaceutiques Françaises, Volume 79, Issue 4, Page Number 335-345, IF 1.36
8. Nangare Sopan, **Dugam Shailesh**, Patil Pravin, Tade Rahul, Jadhav Namdeo\*, Silk industry waste protein: isolation, purification, and fabrication of electrospun silk protein nanofibers as a possible nanocarrier for floating drug delivery, Volume 32, 3, IF 2.9
9. Rathod Prashant, More Harinath, **Dugam Shailesh**, Velapure Pallavi, Namdeo Jadhav Namdeo\*, Fibroin-Alginate Scaffold for Design of Floating Microspheres Containing Felodipine, Journal of Pharmaceutical Innovation (2021) 16:226–236, IF 2.48
10. Shitole Mayuri, **Dugam Shailesh**, Tade Rahul, Nangare Sopan\*, Pharmaceutical applications of silk sericin, Annales Pharmaceutiques Françaises, Volume 78, Issue 6, Page Number 469-489, IF 1.36
11. **Dugam Shailesh**, Nangare Sopan\*, Smart invasome synthesis, characterizations, pharmaceutical applications, and pharmacokinetic perspective: a review, Future Journal of Pharmaceutical Sciences (2020) 6:123, IF 2.6
12. Shitole Mayuri, **Dugam Shailesh**, Desai Neha, Tade Rahul, Nangare Sopan\*, Pharmaceutical applications of electrospun nanofibers: As state-of-the-art-review, Asian Journal of Pharmacy and Technology 10 (3), 187-201, 2020

13. Nangare Sopan\*, Tade Rahul, **Dugam Shailesh**, Shitole Mayuri, Progress in erectile dysfunction therapy through drug delivery system, Thai Journal of Pharmaceutical Sciences (TJPS), Volume 44, Issue 2



# Silver nanoparticles loaded triple-layered cellulose-acetate based multifunctional dressing for wound healing

Shailesh Dugam<sup>a</sup>, Ratnesh Jain<sup>b,\*</sup>, Prajakta Dandekar<sup>a,\*</sup>

<sup>a</sup> Department of Pharmaceutical sciences and technology, Institute of Chemical Technology, Mumbai, India

<sup>b</sup> Department of Biological sciences and biotechnology, Institute of Chemical Technology, Mumbai, India

## ARTICLE INFO

### Keywords:

Biopolymers  
Electrospinning  
Nanofiber  
Bandage  
Antibacterial  
Wound healing

## ABSTRACT

Chronic wounds present considerable challenges which delay their effective healing. Currently, there are several biomaterial-based wound dressings available for healing diverse wound types. However, most of commercial wound dressings are too expensive to be affordable to the patients belonging to the middle and lower socio-economic strata of the society. Thus, in this investigation affordable triple layered nanofibrous bandages were fabricated using the layer-by-layer approach. Here, the topmost layer comprised of a hydrophilic poly vinyl alcohol layer, cross-linked with citric acid. The middle layer comprising of cellulose acetate was loaded with silver nanoparticles as an antibacterial agent, while the lowermost layer was fabricated using hydrophobic polycaprolactone. The triple-layered nanofibrous bandages having a nano-topography, exhibited a smooth, uniform and bead-free morphology, with the nanofiber diameter ranging between 200 and 300 nm. The nanofibers demonstrated excellent wettability, slow *in vitro* degradation, controlled release of nano-silver and potent antibacterial activity against Gram-negative (*E.coli*) and Gram-positive (*S. aureus*) bacteria. The fabricated bandages had excellent mechanical strength upto  $12.72 \pm 0.790$  M. Pa, which was suitable for biomedical and tissue engineering applications. The bandage demonstrated excellent *in vitro* hemocompatibility and biocompatibility. *In vivo* excisional wound contraction, along with H and E and Masson's Trichrome staining further confirmed the potential of the nanofibrous bandage for full-thickness wound healing. Pre-clinical investigations thus indicated the possibility of further evaluating the triple-layered nanofibrous dressing in clinical settings.

## 1. Introduction

The skin plays an imperative role in protecting the body from microbes, radiations, thermal, biological and mechanical assaults and maintaining its physicochemical functions [1,2]. However, the structural hallmarks and functions of the skin can be affected due to external factors such as cuts, burns, surgery, physical forces, chemical-induced damage and metabolic disorders like diabetes, which may induce wounds [3,4]. The complex process of wound healing comprises of various stages like coagulation and homeostasis, inflammation, migration, proliferation and maturation [5]. However, any hinderance occurring during the wound healing process leads to the development of chronic wounds. The complexity of pathological and physiological conditions, in case of chronic wounds, complicates complete skin regeneration, sometimes leading to massive infections and amputations in patients [1].

Currently, diverse types of wound dressings are commercially

available to treat various wound types. The conventionally available wound dressings, like foam and gauze, adsorb fluids and exudates from the wound area, without keeping the wound moist. This leads to their adherence to the wound, causing pain during their removal [5]. On the other hand, wound dressings prepared using sodium hypochlorite and hydrogen peroxide, in the form of soaks, normally act only as a temporary barriers against haemostasis and infections [5]. Thus, to overcome these limitations of the traditional wound dressings, various delivery systems have been previously explored, which include hydrogels and hydrocolloids. [2,6]. The hydrocolloids are generally useful for managing acute and chronic paediatric wounds, to promote faster healing. However, the hydrogel-based dressings contain significant amount of water and hence cannot adsorb large amounts of exudates and are thus applicable only for low exuding wounds. Additionally, these present handling limitations due to their low mechanical strength, due to excessive presence of liquids [2,6]. Hence, in the last decade, natural and synthetic skin grafts were employed for skin regeneration

\* Corresponding authors.

E-mail addresses: [rd.jain@ictmumbai.edu.in](mailto:rd.jain@ictmumbai.edu.in) (R. Jain), [pd.jain@ictmumbai.edu.in](mailto:pd.jain@ictmumbai.edu.in) (P. Dandekar).

<https://doi.org/10.1016/j.ijbiomac.2024.133837>

Received 4 March 2024; Received in revised form 7 June 2024; Accepted 11 July 2024

Available online 14 July 2024

0141-8130/© 2024 Elsevier B.V. All rights are reserved, including those for text and data mining, AI training, and similar technologies.

[7]. But their high cost, requirement of expertise and extensive care during handling and the inability to retain the original skin structure, has largely limited treatments with grafts. Thus, there is an urgent need to develop a multi-functional wound dressing, that may be efficacious yet cost-effective as compared to the traditional dressings, which was the focus of this study.

An ideal wound dressing, should be able to provide a moist environment, allow adequate gas exchange, adsorb excess exudates and blood from the wound site, prevent wounds from bacterial infections, allow painless removal. Moreover, it should be easy to apply, be non-toxic, non-allergic, should have significant mechanical strength and be able to promote cell proliferation and migration to accelerate the wound healing process [8]. Thus owing to this prerequisite required for ideal wound dressing, researchers have been focusing on the use of nanotechnology for fabricating innovative wound dressings. Some of the nanosystems that have been reported as useful include liposomes, carbon or quantum dots, carbon nanotubes, silver and gold nanoparticles, dendrimers and nanofibers *etc.* [9]. Nanofiber-based interventions have gained worldwide attention due to their unique properties like small pore size, high pore volume, high drug payload, high encapsulation efficacy, low density, high surface area-to-volume ratio for solvation and release of drugs and functional molecules [10]. A number of approaches have been adopted for the fabrication of nanofibers, like self-assembly, template synthesis, and electrospinning *etc.* However, researchers have inferred electrospinning as a versatile technique for fabrication of nanofibers due to the ease of application, high chances of scalability, ability to use wide range of materials and tune their physicochemical properties as nanofibers [11]. A wide range of synthetic, semi-synthesis, natural polymeric materials, either alone or in combination, have been explored for the fabrication of electrospun nanofibers [12]. The mesh-like fibrous structure of the electrospun nanofibers promotes cellular adhesion, cell proliferation, cell respiration, moisture retention, removal of exudates and haemostasis [13]. Their high surface area-to-volume ratio, along with a matrix structure, allows tailored release of encapsulated antimicrobial and therapeutic agents [14]. Additionally, small pore size and large surface area governs better fluid absorption and greater oxygen permeability. The porous nature of electrospun nanofibers prevents the tissue from dehydration, maintaining adequate moisture at the wound site. Nanofibrous mats also provide significant physical and mechanical protection to the skin [15]. Thus, electrospun nanofibers are able to provide all the essential requirements for wound healing and hence are considered as potential candidates for wound healing. Earlier, single layered electrospun nanofiber dressing, incorporating anti-bacterial agents, was investigated for wound healing properties. Muhammad Qamar Khan et al., investigated silver sulfadiazine loaded cellulose acetate nanofibers for burn-related wounds. These nanofibers had a smooth and uniform morphology and exhibited significant antibacterial activity, along with the desired physicochemical and structural properties for wound healing [16]. However, single-layered nanofibrous dressing required frequent changing due to excessive exudate absorption in the case of chronic wounds, which was especially painful for the older people [17]. Additionally, due to the inability of single layered sheets to mimic the behaviour of extracellular matrix, multi-layered nanofiber dressings attracted much attention [18]. Layer-by-layer electrospinning approach has been widely accepted for fabrication of multi-layered dressing. Here, one layer was electrospun at a time, which acted as the base for the next layer that was electrospun over it. Serdar Torta et al. fabricated tri-layered nanofibrous dressing wherein, the first and second layers were fabricated using alginate and chitosan. The third co-axial layer consisted of collagen/PCL at the core and doxycycline in polyethylene oxide as the shell. The developed wound dressing comprised of aligned nanofibers, which exhibited a bioadhesion value of 0.485 mJ/cm<sup>2</sup> over the rat skin, an excellent tensile strength of 2.76 MPa, and a porosity of 52.3 %, with good wettability and no cytotoxic effect towards the keratinocytes. Thus, the three-layered wound dressing acted as good intervention for wound healing

applications. [19]. However, application of these dressing restricted due to the risks associated with the pathogen transmission, which varied with the collagen source and enzymatic degradation of collagen, ultimately leading to a lower dressing stability [20,21]. Thus, there is need to develop alternative multi-layered wound dressing.

In this investigation, we have fabricated a triple-layered electrospun nanofiber bandage using the layer- by-layer approach, wherein, the top layer was fabricated using PVA and cross-linked with citric acid, the middle layer was comprised of CEA and loaded with AgNPs, while the basal layer was composed of hydrophobic PCL. The topmost layer was fabricated using poly vinyl alcohol (PVA) due to its versatile properties, relatively low cost, wide availability, significant solubility in aqueous solutions, ability to prevent dehydration and excellent mechanical strength [22]. However, to achieve a slow degradation and to improve its mechanical strength, this layer was cross-linked with the green crosslinker, citric acid (CA). The use of CA to cross-link the PVA layer not only improved its stability but also provided an acidic milieu at the wound site, which helped to alter the protease activity in the wound area and led to detoxification of its toxic end products. Moreover, the acidic pH may also have enhanced the flux of oxygen within the wound niche and may have accelerated the healing rate. Furthermore, the use of CA was thought to promote re-epithelialisation and angiogenesis (due to enhanced oxygen uptake), resulting in faster formation of healthy granulation tissue and hence rapid wound healing [23]. The middle layer consisted of cellulose acetate (CEA) and incorporated silver nanoparticles (AgNPs) as an anti-bacterial agent. CEA due to its excellent biocompatibility, slow biodegradability, a high thermal stability, coagulation properties water absorption abilities, regenerative potential and thus exudate adsorption and ability to interact with the skin cells may have accelerated wound healing [24]. However, poor antibacterial activity and low mechanical strength limit the application of this polymer. Thus, inclusion of AgNPs and the mechanical support provided by the overlying PVA layer improved the functional properties of the CEA layer. The presence of free radicals and bacteria lead to harmful cytotoxic effects, triggering oxidative stress and delaying the wound healing process [25]. Therefore, the use of an appropriate anti-bacterial and anti-oxidant may be an important strategy to improve wound healing by reducing excess free radicals and persistent inflammation. AgNPs, with their ability to oxidise in the aqueous environment, and ability to provide a broad range anti-bacterial effect over prolonged period, through a slow release from the polymeric matrix, assisted in the wound healing process. Finally, the basal layer was fabricated using the hydrophobic polycaprolactone (PCL) to achieve a good adhesion to the skin cells and avoid the painful removal of the bandage. Also, the porous structure of the PCL layer mimicked the extracellular matrix of the skin and provided significant oxygen permeability, for effective wound healing [26,27]. Moreover, each of these layers was synthesized using widely and commercially available polymers, that are well accepted in the pharmaceutical industry, using a scalable and commercially feasible manufacturing process. Thus, considering the unique properties of these electrospun layers, each having a nano-topography, we hypothesized that the unique PVA/CEA/PCL multi-layered dressing, containing AgNPs, could collectively provide an effective, wound-healing solution.

## 2. Materials and methods

### 2.1. Materials

Cold water soluble PVA (MW ~ 160000 g/mol; degree of hydrolysis ~86.50–89 mol%) was purchased from Himedia Laboratories Pvt. Ltd., Mumbai, India. Cellulose acetate CEA (MW ~ 30000 g/mol) was purchased from Sigma Aldrich Ltd. (USA), polycaprolactone PCL (MW ~ 80000 g/mol) was purchased from Sigma Aldrich Ltd. (USA), dimethyl sulphoxide (DMSO) analytical grade (AN), N, N dimethyl formamide (DMF) AR grade, methanol, tetra hydrofuran (THF), acetone, chloroform AR grade, ethylene diamine tetra acetic acid dipotassium salt LR

grade (EDTA), citric acid (CA) were purchased from SD Fine Chemical Limited, Mumbai. Silver nitrate ( $\text{AgNO}_3$ , MW  $\sim 169.87$  g/mol) and sodium borohydride ( $\text{NaBH}_4$ , MW  $\sim 37.83$ ) was purchased from Avra synthesis, Hyderabad (India), *Escherichia Coli* ATCC 25922 and *staphylococcus aureus* ATCC 25923 were obtained as gift samples from Khalsa college, Mumbai (India). Nutrient broth (N.B.), agar-agar, Dulbecco's Modified Eagle Medium-High glucose (DMEM), human dermal fibroblast (HDF) cell line, 3-(4,5-dimethylthiazol-2-yl)-2,5-diphenyltetrazolium bromide (MTT) and EZ Blue cell assay kit were obtained from Himedia Laboratories Pvt. Ltd., Mumbai, India. Fetal bovine serum (FBS) was procured from Invitrogen, USA, while 1 % antibiotic-antimycotic was from Life Technologies, Mumbai. Human ELISA kit -TAT was acquired from (Biogenuix medystem, India). The human keratinocyte (HaCaT) cell line was kindly gifted by ACTREC, Mumbai, India. Deionized and double-distilled water (Milli-Q Plus system, Millipore, Bedford, MA, USA) was used in all the experiments. The electrospinning unit, EspinNano-2, was purchased from Physics equipment, Chennai, India.

## 2.2. Fabrication of PVA nanofibers as the top layer and its cross-linking with CA

PVA nanofibers were fabricated as per a previously reported method, with slight modifications, as needed [28]. Initially, 9 % w/v of PVA was dissolved in distilled water by continuous stirring for 4 h, till a homogenous solution was obtained. Further, the homogenous solution was loaded into a 5 mL of syringe, fitted with a 18 G needle, and the nanofibers were electrosun using optimized electrospinning process parameters. The flow rate was maintained at 1 mL/h, voltage at 20 kV, while the distance between the collector drum and the tip of the needle was kept at 10 cm, at the temperature of  $30 \pm 2^\circ\text{C}$  and relative humidity range of  $40\% \pm 2\%$  to  $60\% \pm 2\%$ . The nanofibers were collected over a collector drum, on an aluminium foil. The layered nanofibrous sheet was peeled off and further cross-linked using citric acid (CA). The nanofibrous mats was cross-linked with various weight percentages of CA, ranging from 1 % to 5 % (w/v), to enhance their mechanical property. The cross-linked nanofibrous mats were treated in vacuum oven with vapours of CA, at  $90^\circ\text{C}$ , for 15 min. Here, the heat treatment was crucial to complete the cross-linking process [29]. The cross-linked nanofibrous sheets were then used for further characterization.

## 2.3. Fabrication of silver nanoparticle loaded (AgNPs) CEA nanofibers as the middle layer

Initially, AgNPs were synthesized in-house using a unique micellar technology, based on the chemical reduction of 10 mM of silver nitrate ( $\text{AgNO}_3$ ) using 3 mM of sodium borohydride ( $\text{NaBH}_4$ ). Here,  $\text{NaBH}_4$  was used as the reducing agent while poly ethylene glycol (PEG) was used as the capping agent. The method for formulation for AgNPs was optimized with respect to process parameters like the residence time (sec), flow rate of the  $\text{AgNO}_3$  solution ( $\mu\text{L}/\text{min}$ ), flow rate of the  $\text{NaBH}_4$  solution ( $\mu\text{L}/\text{min}$ ), flow ratio of the  $\text{AgNO}_3$  and  $\text{NaBH}_4$  and the concentration of the capping agent. The detailed optimization protocol and methods for the characterization of AgNPs have been described in the supporting information. The AgNPs were further dispersed in water, at the concentration of 200 ppm. This dispersion was added in a dropwise manner into the polymeric solution of cellulose acetate (CEA, 16 % w/v) solution, in dimethylformamide (DMF) and acetone, at the ratio of 1: 3 v/v. The suspension was continuously stirred at 500 rpm to obtain a homogenous dispersion of AgNPs in CEA. The AgNPs loaded CEA nanofibers were fabricated by slightly modifying a previously described electrospinning protocol [16]. The dispersion of AgNPs in water, at the concentration of 200 ppm, was mixed with the CEA solution in DMF (16 % w/v) and acetone, at the ratio of 1: 3 v/v. Further, this mixture was filled into 5 mL syringe, fitted with 18 G needle, and the solution was electrosun over the previously collected PVA layer. The optimized

electrospinning parameters included a voltage of 16 kV, flow rate of 0.7 mL/h and the distance between collector drum and tip of needle of 10 cm, the temperature of  $30 \pm 2^\circ\text{C}$  and relative humidity range between  $40\% \pm 2\%$  to  $60\% \pm 2\%$ . The developed sheet was used for further characterization.

## 2.4. Fabrication of polycaprolactone nanofiber as the lower layer

Porous PCL layer was fabricated by modifying a previously reported electrospinning method based on non-solvent induced phase separation mechanism (NIPS) [30]. Initially, PCL was dissolved at the concentration of 10 % w/v in a mixture of chloroform and dimethyl sulfoxide, at the volume ratio of 3:1 (good/bad solvent), at  $25^\circ\text{C}$ . This solution was fed into 5 mL syringes, fitted with 18 G needle, and the solution was electrospun on formerly collected CEA layer. The optimized parameters for the electrospinning process was flow rate of 1 mL/h, voltage of 20 kV, syringe tip-to-collector distance of 10 cm, temperature of  $30 \pm 2^\circ\text{C}$  and relative humidity range of  $40\% \pm 2\%$  to  $60\% \pm 2\%$ . The fabricated matrices were peeled off and used for further characterization.

## 2.5. Morphological evaluation using SEM and TEM

Morphological analysis of the electrosun, non-crosslinked (PVA NFs) and crosslinked PVA nanofibers (PVA CA NF), CEA nanofibers (CEA NF) and PCL nanofibers (PCL NF), individually, and as cross-section of AgNPs loaded the triple layered nanofibrous sheet (TNF) was conducted after sputtering with gold coating (Denton gold sputter unit for 120 s). A field emission electron microscope (FEI Quanta 2000, Netherlands) operating at a 10 kV acceleration voltage was used for the analysis. Using ImageJ software, the average diameter of the nanofibers ( $n = 50$ ) was determined. The CEA electrosun nanofibers loaded with AgNPs were first submerged in acetone. The separated nanofibers were next seen in transmission electron mode (FEI Tecnai 12, Netherlands) at an acceleration voltage of 200 kV for ten minutes on a carbon-coated TEM grid.

## 2.6. Attenuated total reflectance infrared spectroscopy (ATR-FTIR)

To comprehend any potential chemical interactions between the polymers or the creation of ester bonds during cross-linking, structural investigation has been performed using by Attenuated Total Reflectance Fourier Transform Infrared Spectroscopy (ATR FTIR, JASCO FT/IR-4000). The spectra were obtained between the wave numbers 400 to  $4000\text{ cm}^{-1}$ .

## 2.7. Thermo gravimetric analysis (TGA) of the TNF

Thermo gravimetric analyses of PVA, PVA NF, CA, PVA CA NF, CEA, CEA NF, PCL, PCL NFs, and TNF were performed to study their thermal behaviour and decomposition temperature. The investigations were carried out utilizing a thermogravimetric/differential thermal analysis (TGA/DTA) device (DTG-60H SHIMADZU, Japan), which was capable of measuring both simultaneously. All the samples were analysed in the temperature range of  $30\text{--}600^\circ\text{C}$ , at the heating rate of  $10^\circ\text{C}/\text{min}$ , in a nitrogen atmosphere, at the flow rate of 100 mL/min.

## 2.8. Crystal structure elucidation by X-ray diffraction (XRD)

The X-ray diffraction patterns of PVA, PVA NF, CA, PVA CA NF, CEA, CEA NF, PCL, PCL NF, and TNF sheets were recorded using (Lab X XRD-6100 SHIMADZU, Japan), equipped with  $\text{Cu K}\alpha$  radiation ( $\lambda = 1.54\text{ \AA}$ ). The XRD patterns were characterized in the  $2\theta$  range of  $5\text{--}50^\circ$ , with a step size of  $0.02^\circ$  and a counting time of 5 s/step. The generator voltage was maintained at 40 kV, and the generator current was 30 mA.



## 2.9. Water uptake study

During the water uptake study, the PVA CA NF, CEA NF, PCL NF and TNFs, weighing 20–30 mg, were immersed in 10 mL of 1X phosphate buffer saline (PBS), over a period of 7 to 15 days. The mats were immersed separately in glass vials [31]. The water uptake of the NFs was calculated on the basis of wet and dry weights using Eq. (1). The excess water from the mats was removed with a filter paper, before calculating the water uptake. All the measurement was recorded in triplicates ( $n = 3$ )

$$\text{Water uptake ability} = \frac{(W_f - W_i)}{W_i} * 100\% \quad (1)$$

where,  $W_i$  represented the initial dry weight of the nanofibrous mats and  $W_f$  represented the wet weight of the nanofibrous.

## 2.10. Water vapor transmission rate

The water vapor transmission rate (WVTR) was measured using the rate of change of mass of water in the vials. The PVA CA NF, CEA NF, CEA AgNPs NF, PCL NF and TNF sheets were cut into pieces having dimension of 3 cm × 3 cm and thereafter were mounted on the mouth of a cylindrical glass vial containing distilled water. The vials with samples were sealed using a paraffin tape and then placed in an incubator, at 50 % relative humidity. The weight change of water was measured manually, at the interval of 24 h and the WVTR was calculated using Eq. (2). The initial weights of the vials were recorded and the final weights were measured after 24 h. All the measurements were recorded in triplicates ( $n = 3$ ).

$$\text{Moisture uptake} = \Delta W A \quad (2)$$

where,  $\Delta W$  was the difference in initial and final weight (g) of the water in the glass vials,  $A$  was the surface area exposed ( $\text{m}^2$ ) for 24 h and WVT was expressed as  $\text{g}/\text{m}^2/\text{day}$  [32].

## 2.11. Porosity evaluation

The porosity of the PVA CA NF, CEA NF, CEA AgNPs NF, PCL NF and TNF sheets was measured by the liquid displacement method [33]. The samples mentioned above absorb ethanol without becoming swollen. The each mat were submerged for 5 min in a known volume of ethanol ( $v_1$ ) within a graduated cylinder. The entire volume of ethanol that penetrated the NFs sheets was then recorded as volume ( $v_2$ ). After removing the ethanol-penetrated nanofiber mats from the cylinder, the quantities of ethanol that remained were noted ( $v_3$ ). Eq. (3) was utilized in the computation of porosity.

$$\% \text{Porosity} = \frac{V_1 - V_3}{V_2 - V_3} * 100 \quad (3)$$

## 2.12. Water contact angle measurement

Water loving and hating properties of the PVA CA NF, CEA NF, PCL NF and TNF sheets were measured using KYOWA interFace Measurement and Analysis System- FAMAS. The samples were placed on the stage, following which a droplet of deionized water (2  $\mu\text{L}$ ) was placed on the surface of the sample. The image of water droplet on each sample was captured and the contact angles were measured by using ImageJ program.

## 2.13. Mechanical strength analysis

The tensile strength of the nanofibrous mats was studied using a Electroforce 5500 model (TA, instruments USA). For determination of the mechanical strength for non-crosslinked, and crosslinked PVA NF, CEA NF, AgNPs loaded CEA NFs and PCL NF, individually, and the TNFs.

The 3 cm × 3 cm nanofibrous mats were put in the sample holder, and the force at which the mats began to deform was measured as well as the tensile strength at room temperature (25 °C) under a load of 20 N and a crosshead speed of 50 mm/s. The mechanical strength of nanofibrous mats were calculated using Eq. (4).

$$\text{Mechanical strength} = \frac{\text{Force required to break the sheet}}{\text{cross sectional area of sheet}} \quad (4)$$

## 2.14. In vitro degradation studies of the nanofibrous mats

After calculating the initial weight of the mats, degradation tests of PVA CA NF, CEA NF, CEA AgNPs NF, PCL NF, and TNF were conducted. The mats were then incubated at 37 °C with 10 mL of phosphate buffer saline (pH 7.4) containing lysozyme (0.25 mg/mL, 10,000 U/mL). The concentration of the enzyme that was utilized was comparable to that of human serum. [34]. In order to retain mat activity, 10 mL of fresh lysozyme was introduced every 3 days. After that, the samples were mixed with 0.2 mL of 0.25 M EDTA to inactivate any remaining lysozyme. The samples were taken out at the conclusion of each degradation period, freeze-dried, and cleaned three times using distilled water in order to determine the weight loss. Eq. (5) was used to compute the weight reduction.

$$\% \text{weight loss} = \frac{W_i - W_f}{W_f} * 100 \quad (5)$$

where,  $W_i$  is the initial weight of the samples and  $W_f$  is the final weight of the samples.

## 2.15. Evaluation of cellular toxicity using MTT assay

The cellular cytotoxicity of PVA CA NF, CEA NF, CEA AgNPs NF, PCL NF and TNF mats were evaluated to confirm their safety towards the human dermal fibroblasts (HDF) and human keratinocyte cells (HaCaT) using the MTT assay [35]. The cells were cultured in a 24-well plate, in DMEM High Glucose medium, supplemented with 10 % fetal bovine serum (FBS) and 1 % antibiotic-antimycotic solution. The medium was changed every 72 to 96 h. After trypsinizing the cells, an automatic cell counter (Countless 3FL, Invitrogen India) was used to count the number of cells. Following a 5 min centrifugation at 20 °C, the resultant cell suspension was again suspended in the enriched medium. For the MTT assay, all the non-crosslinked and crosslinked PVA NF, CEA NF and PCL NF, individually, and the TNF sheet were sterilized using ethylene oxide sterilization (gas concentration used – 90 % ethylene oxide and 10 %  $\text{CO}_2$ , temperature – 60 °C and time 6 h). The 20 mm × 20 mm nanofibrous sheets were seeded with  $3 \times 10^5$  cells in 2 mL of the supplemented media, and they were then incubated for 24 h at 37 °C, with 5 %  $\text{CO}_2$  and 99 % relative humidity. Incubation took place for 4 h after the old medium was removed from the wells and replaced with 2 mL of fresh medium, wherein 500  $\mu\text{L}$  of the MTT reagent were added. Under a microscope, formazan crystal growth was seen. After dissolving the formazan crystals in each well with 500  $\mu\text{L}$  of cell culture grade DMSO, the absorbance was measured at 570 nm, with the background absorbance measured at 690 nm, using a multimode microplate reader (VICTOR® Nivo™ PerkinElmer, Singapore). Relative % cellular viability was calculated by Eq. (6).

$$\% \text{cell viability} = \frac{(A_{570} - A_{690}) \text{ cells treated with NF sheet}}{(A_{570} - A_{690}) \text{ control cells}} * 100 \quad (6)$$

## 2.16. Cellular proliferation study using EZ blue assay

The cellular proliferation over the PVA CA NF, CEA NF, CEA AgNPs NF, PCL NF and TNF mats were evaluated using the human dermal fibroblast (HDF) and human keratinocyte cells (HaCaT), using the Alamar blue assay [36]. The cells were cultured in a 24-well plate, in DMEM

High Glucose supplemented with 10 % fetal bovine serum (FBS) and 1 % antibiotic-antimycotic solution. The medium was replaced every 72 to 96 h. The cells were trypsinized and the cell count was measured using an automated cell counter (Countless 3FL, Invitrogen India). The resulting cell suspension was centrifuged for 5 min, at 20 °C, and resuspended in the supplemented medium. For the EZ blue assay, all the non-crosslinked and crosslinked PVA CA NF, CEA NF, CEA AgNPs NF, PCL NF and TNF mats were sterilized ethylene oxide sterilization (gas concentration used –90 % ethylene oxide and 10 % CO<sub>2</sub>, temperature –60 °C and time 6 h). The nanofibrous sheets having the dimension of 20 mm × 20 mm were seeded with cells, at the density of  $3 \times 10^5$  cells in 2 mL of the supplemented medium and incubated at 37 °C, in presence of 5 % CO<sub>2</sub> and 99 % relative humidity. The constructs were evaluated using EZ Blue assay on days 1, 2 and 3. The media was replaced with 2 mL of fresh medium containing 10 % EZ Blue dye (10 % EZ Blue blue, 80 % medium and 10 % FBS v/v) and incubated for 3 h. Later, 300 mL of the medium was pipetted out to measure the absorbance at the wavelength of 570 nm, keeping 600 nm as the reference wavelength, in the microplate reader (VICTOR® Nivo™ PerkinElmer, Singapore). The manufacturer's protocol was followed to calculate the percent dye decrease which are a sign of cellular proliferation.

#### 2.17. Thrombin generation assay to assess the haemostasis activity

The thrombin generation assay was conducted using heparinized samples of whole human blood obtained in EDTA coated 50 mL tubes. The samples PVA NF, PVA CA NF, CEA NF, CEA AgNPs NF, PCL NF, and TNF mats in comparison with gauze were tested for thrombin generation. One millilitre of blood was incubated on the sterile mats for one hour at 37 °C. To prevent the creation of new thrombin, 0.3 mL of sodium citrate solution (0.633 M) was combined with the blood sample. Next, the entire blood was separated from the plasma by centrifuging it for 20 min at 28 °C at 4000 rpm. The plasma obtained was subjected to further treatment to determine thrombin generation throughout 1 h, using the thrombin-antithrombin complex human ELISA kit TAT, as per the manufacturer's instructions.

#### 2.18. Loading and release characteristics of AgNPs

AgNPs were dispersed and added to the electrospinning solution for the CEA layer at a 200 ppm concentration. The precise concentration of silver (30 mg) in the form of Ag<sup>+</sup> ions was measured on a 3 cm × 3 cm CEA mat prior to the *in vitro* release tests. By dissolving the samples in 95 % nitric acid (HNO<sub>3</sub>; 5 mL) and adding the release medium (PBS, pH 7.4) containing lysozyme (10,000 U/mL in PBS pH 7.4, 10 mL) to duplicate the presence of enzymes in injured tissues, the amount of silver contained in CEA mat was ascertained. Using 0.1 N NaOH, the medium's pH was brought to neutral. The inductively coupled plasma atomic emission spectroscopy (ICP-MS) was used to detect the concentration of liberated silver from the TNF mat. [37]. Over 7 days, the quantity of silver released was measured at predetermined intervals. Measurements were done in triplicate at each time point. The amount of silver contained in the specimens before they were submerged in the release medium was used to compute the cumulative silver release, which was determined after carefully analysing the data that was collected. Eq. (7) provides the formula for computing cumulative silver release.

$$\text{Cumulative amount of silver release (\%)} = \frac{M_t}{M_i} \times 100 \quad (7)$$

where  $M_i$  was the quantity of silver in the samples prior to the release studies, and  $M_t$  was the amount of silver released at time  $t$ . The release profile AgNPs from TNF was analysed by PCP-Disso-V3.08 software. Here, to describe the dissolution profile in a model-dependent manner, the zero-order, first-order, Higuchi, Hixson-Crowell, Korsmeyer, and Peppas's equations were chosen. Three key factors were considered for

the release mechanism study: the  $n$ -release exponent, the  $k$ -release rate constant, and the  $r^2$  correlation coefficient. [33]

#### 2.19. Antibacterial evaluation

The disc diffusion method, were used to investigate the anti-bacterial activity of AgNPs incorporated TNF against two common bacteria present in infected wounds, *Escherichia coli* and *Staphylococcus aureus*, in order to determine its potential utility as a functional wound dressing. [38]. *Staphylococcus aureus* ATCC 25923 and *Escherichia coli* ATCC 25922 cultures were used to create the bacterial inoculums. The cultures were serially diluted with peptone water, after being cultured in nutrient broth for 24 h, at 37 °C. The resulting microbial suspensions were flooded over petri plates containing nutrient agar. Untreated microorganisms served as the negative control, whereas AgNP dispersion (0.3 ppm) was employed as the positive control. After applying TNF (2 cm × 2 cm) over the plate surface, it was incubated at 37 °C, for 24 h. The zone of inhibition in each plate was measured in centimetres, after incubation.

#### 2.20. In-vivo wound healing efficacy of the multi-layered nanofibrous mat

This study aimed to compare the therapeutic efficacy of cotton gauze, a typical dressing, with AgNPs laden TNF mats. In this work, the wound healing process was examined using the partial thickness wound model in Sprague-Dawley rats. The Institutional Animal Ethics Committee (IAEC) approved the acquisition of eighteen male Sprague-Dawley rats, which were obtained from the National Institute of Biosciences in Pune (Approval No.: ICT/IAEC/2022/M02/P17). Each animal was kept in a separate plastic cage and given water and sterile rodent chow for food. The rats were given seven days to acclimate before the trials began. Rats were given intraperitoneal injections of ketamine-xylazine in an 80:20 v/v ratio, with a dose of 80 mg/kg ketamine and 20 mg/kg xylazine, to induce anaesthesia. Using a clipper, the hair was removed from the dorsal region of the rat, and fine hair was removed using a shaving razor and depilatory cream without causing any injury to the skin. Afterwards, surgical spirit was used to clean and disinfect the affected area. A total of six male Sprague Dawley rats were randomly assigned to three groups. The first group was used as a negative control, in which the wounds were left untreated. The second group was a positive control, in which cotton gauze treatment was applied. While, the third group was used as a test group, having TNF mats with AgNPs inserted over the rat skin. A partial thickness wound model in the dorsal region of the rat, with each wound having an 8 mm diameter, made with a sterile biopsy punch. Each rat's dorsal region was cleaned with diluted iodine, and the wounds were then dressed appropriately and secured with medical tape. Further dressing was changed on day 3, 7 and 10.

#### 2.21. Wound area measurement

The wound dressing was taken off on days 3, 7, and 10, and the areas of the wounds were measured using a clear polyethylene sheet. The region was marked with a marker pen and the sheet was left over the wound. The highlighted region was then moved to a graph sheet so that the precise measurements could be ascertained. The wound was photographed concurrently. Eq. (8), based on the image, was used to compute the rate of wound healing and quantify the area of the wound using Image J software.

$$\% \text{rate of wound healing} = \frac{A_{wi} - A_{wn}}{A_{wi}} \times 100 \quad (8)$$

where,

$A_{wi}$  was the initial area of wound

$A_{wn}$  was the remaining area of wound on the  $n^{\text{th}}$  day of wounding

## 2.22. Haematoxylin and eosin/Masson's Trichrome staining

The damaged rat's skin was cut into 5 × 5 cm pieces on day 10. To stop the skin tissue from deteriorating, it was submerged in a 10 % formalin solution. After that, tissue-embedding paraffin blocks were ready. The paraffin slices were placed on super freeze slides, dried on a hot plate, and then submerged in three sets of xylenes for 10 min each to get ready for H&E staining. Following that, the object was cleaned with three sets of 100 % ethanol for 10 min each, and then it was rinsed with tap water. The portions had to be dehydrated and the wax removed. After 5 min in haematoxylin, the slides were carefully washed under tap water for a duration of roughly 4–5 min. After adding 1 % acid alcohol (1 % HCl in 70 % v/v alcohol) for 5 s and washing with tap water, excess haematoxylin was eliminated. Scott's tap water was used to wash the pink haematoxylin stain for around 10 s, or until the sections turned blue. After rinsing the slides in tap water, they were stained for 15 s with 1 % w/v eosin and then rinsed for 1 to 5 min under running tap water. After that, the sections were dehydrated for 10 min each using two washes of pure alcohol and two washes of xylene. Afterward, they were mounted in DPX mount and protected with glass cover slips. After that, the slides were examined under a microscope. Additionally, Masson's Trichrome staining was used to examine and quantify the expression of collagen in wound tissues. The proportion of the wound that was blue was used to measure collagen expression.

## 2.23. Statistical analysis

Statistical analysis was conducted by using the Student's *t*-test approach and GraphPad Prism, Windows version 8.2 (GraphPad Prism San Diego California USA). The format of the data was mean ± standard deviation (SD). At the probability level, *P*-values <0.05 were considered statistically significant, and those <0.001 were considered extremely significant.

## 3. Result and discussion

### 3.1. Standardisation of the electrospinning and the cross-linking methods

The morphology of electrospun nanofibers depends on various properties of the polymeric solutions, such as their viscosity, polymer concentration, conductivity and surface tension, as well as various electrospinning process parameters, like voltage, flow rate, syringe translation movement, and distance between the tip of the needle and the collector drum. All three layers, viz. the topmost PVA layer, the middle CEA layer, and the bottom-PCL layer, were optimized with respect to the polymeric solution characteristics and electrospinning parameters at which uniform nanofibers were obtained. Since, PVA nanofibers, due to their inherent hydrophilic properties, were rapidly degraded in aqueous solution, they were unable to maintain their porous structure. Thus, PVA NFs were further cross-linked to impart them water stability. A number of approaches have been employed for cross-linking PVA, including formation of its blend with hydrophobic polymers and the use of chemical cross-linkers. Various cross-linkers, like glutaraldehyde [39], glyoxal [40], malic anhydride [41] etc. have been used for cross-linking of PVA. However, these crosslinkers are toxic at higher concentrations and also do not offer the required level of stability [42]. On the other hand, organic acids such as citric acid, are biocompatible and can provide desired properties and improve the adhesion and proliferation of cells [43]. In this study, cross-linking of PVA nano-mats was conducted using CA, at different concentrations (1–5%w/v), along with thermal treatment. Further, the effect of cross-linking on the morphology of PVA NF mats was studied using SEM. Also, cross-linking with CA was confirmed using FTIR spectroscopy.

### 3.2. Morphological analysis using SEM and TEM

Morphological analyses of PVA NF, PVA CA NF, CEA AgNPs NF, PCL NF and TNF were performed using SEM. Field emission electron microscopic images of different nanofibrous layers and their diameter distributions have been presented in Fig. 1 A–H. The individual layers of the TNF dressing comprised of nano-ranged fibres, having uniform, smooth, and bead-free structure. The average diameter of the PVA NF in the top layer of the TNF mats was found to be  $132.46 \pm 15.32$  nm (Fig. 1 A). SEM images (Fig. 1 B–D) showed that the nanofiber mats, when cross-linked with 1–3 % w/v citric acid, resulted in smooth and uniform nanofibers, with slight bigger average fiber diameter as compared to the fibres in the non-cross-linked mats. Further, upon increasing the concentration of the citric acid from 4 to 5 % w/v, it was found that the fibres formed were thick, non-uniform, rough, and exhibited bead formation, as seen in Fig. 1 E and F. Thus, the PVA NF mats were crosslinked with 3 % w/v of CA in all the further investigations. The nano-mats cross-linked with appropriate concentration of CA were able to preserve a web-like structure. The average diameter of the NFs in the CEA layer containing the AgNPs was found to be  $161.23 \pm 12.23$  nm, as seen in Fig. G. While, Fig. 1H, confirms that the average diameter of NFs in the PCL layer was  $212.56 \pm 27.23$  nm. It was anticipated that the web-like structure of the fabricated NF mats could help in significant cellular respiration and prevent the wound from being dehydrated. Also, the structure suggested a high surface area-to-volume ratio, which was hypothesized to enable higher absorption of the wound exudates. Additionally, the AgNPs loaded CEA layer NFs were assessed using a transmission electron microscope, which confirmed the presence of AgNPs within the NFs, as shown in Fig. 1 I–J. The sizes of the optimized AgNPs were analysed by TEM (Fig. S2). Further, the loading of NPs was also confirmed by elemental analysis (EDAX) (Fig. S3). Additionally, the cross-section of the TNF sheet was assessed using SEM. Fig. 1 K confirmed that all the three nanofibrous layers were successfully preserved by the layer-by-layer approach and resulted in adequate adhesion with the adjacent layers.

### 3.3. Attenuated total reflectance infrared spectroscopy (ATR-FTIR)

Attenuated Total Reflectance Infrared Spectroscopy was used to investigate the functional groups in the manufactured mats, and to study any unfavourable interactions between the polymers during the electrospinning process. The spectra of PVA, CA, CEA and PCL were used as the controls and were compared with the spectra of the electrospun PVA NFs, cross-linked PVA NFs, CEA NFs and PCL NFs. The FTIR spectra, as shown in Fig. 2Aa, revealed the characteristic bands for PVA, exhibiting the presence of hydroxyl group (–OH) at  $3297.60$   $\text{cm}^{-1}$ , the –CH alkyl stretch at  $2975.62$   $\text{cm}^{-1}$ , the alcohol stretch at  $1284.078$   $\text{cm}^{-1}$  and the C–O stretching at  $1033.45$   $\text{cm}^{-1}$  [44]. The FTIR spectrum for the PVA NFs (Fig. 2Ab) exhibited absorption bands at similar wavelengths, with slight shifts. The hydroxyl group resulted in a band at  $3288.43$   $\text{cm}^{-1}$ , the alkyl stretch was visible at  $2983.33$   $\text{cm}^{-1}$ , the alcohol stretch was seen at  $1288.15$   $\text{cm}^{-1}$ , while the C–O stretching was observed at  $1048.32$   $\text{cm}^{-1}$ , which confirmed the absence of any unwanted chemical interactions during the electrospinning process. The FTIR spectrum for CA (Fig. 2Ac) exhibited a large and intense band at  $3494.30$   $\text{cm}^{-1}$ , which was attributed to the O–H Stretching. The vibration bands observed at  $3019.00$   $\text{cm}^{-1}$  and  $2558.00$   $\text{cm}^{-1}$  corresponded to the C–H stretching. The peaks at  $1753.19$   $\text{cm}^{-1}$  and  $1721.83$   $\text{cm}^{-1}$  were assigned to the shift in the C=O vibration, due to the symmetric stretching of the COOH group of CA [45]. In case of the cross-linked PVA NFs (Fig. 2Ad), all vibration bands of PVA were observed, in addition to the vibration band for C=O stretching of the COOH group of CA at  $1733.00$   $\text{cm}^{-1}$  and  $1715.09$   $\text{cm}^{-1}$ , which confirmed that the PVA NF mats were successfully cross-linked with CA. The FTIR spectra of CEA (Fig. 2Ae) and CEA NF (Fig. 2Af) samples exhibited same bands, a smaller band at  $2945$   $\text{cm}^{-1}$  due to the C–H stretching vibration in CA, the adsorption peak at



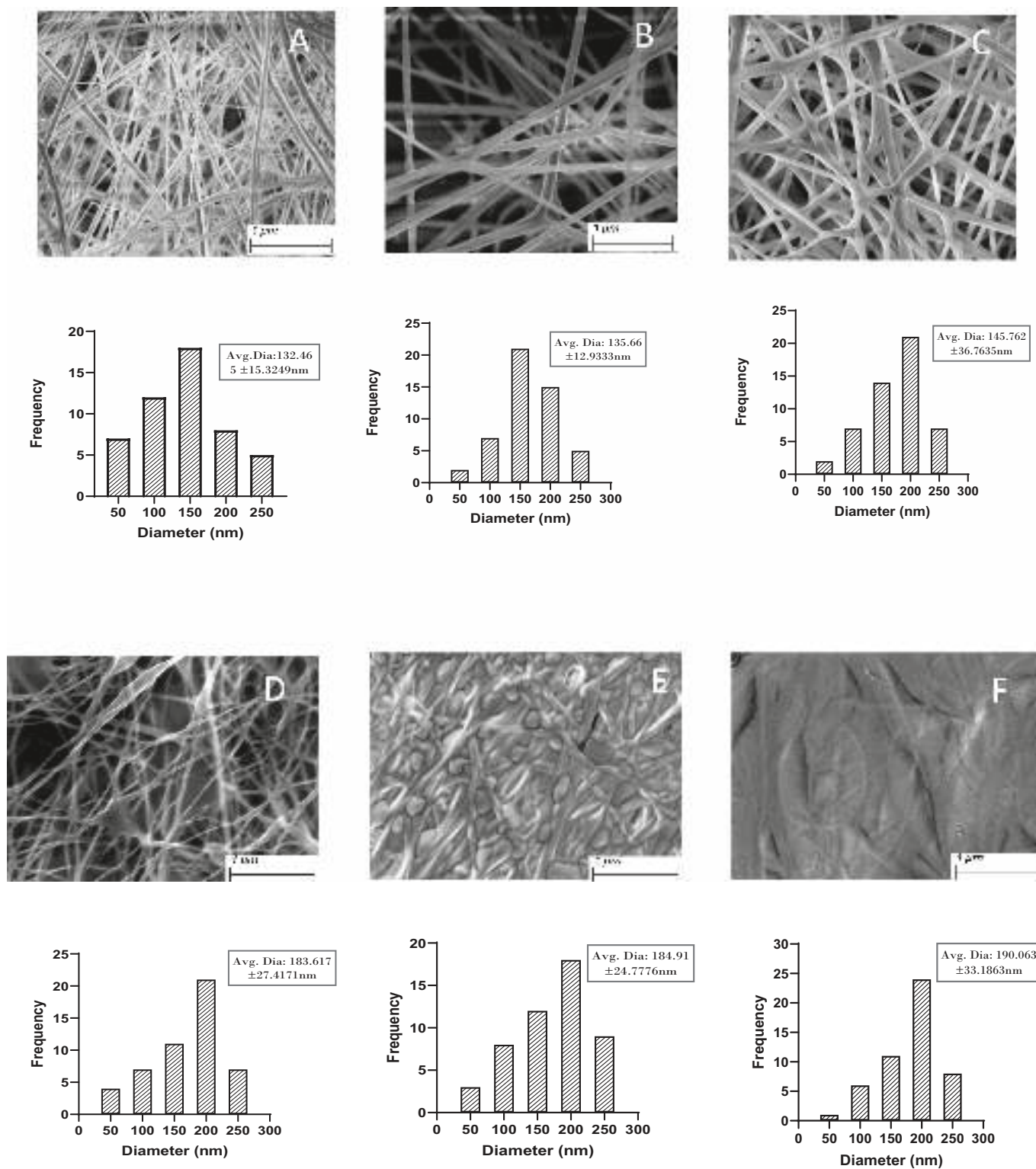


**Fig. 1.** A) SEM image and diameter of the non-crosslinked PVA NF, B) crosslinked PVA NF (1%CA) C) cross-linked PVA NF (2%CA) D) crosslinked PVA NF (3%CA) E) cross-linked PVA NFs (4%CA) F) cross-linked PVA NFs (5%CA) G) AgNPs loaded CEA NFs H) the PCL NFs I-J) TEM image of AgNPs loaded in CEA NFs K) SEM image of the cross-section of TNF.

1730–1737  $\text{cm}^{-1}$  due to the C=O stretching vibration of ester, the C–O and C–H bending vibrations at around 1228 and 1368  $\text{cm}^{-1}$ , respectively. The C–O stretching in CEA was seen as a wide band at 1050  $\text{cm}^{-1}$  [46]. Similarly, the FT-IR spectra of PCL (Fig. 2Ag) and PCL NF (Fig. 2Ah) mats showed two characteristic peaks at 2943–2940  $\text{cm}^{-1}$

and 2863–2855  $\text{cm}^{-1}$ , which corresponded to the stretching bands of the  $\text{CH}_2$  groups. The absorption peak at 1730  $\text{cm}^{-1}$  was ascribed to the stretching of the C=O groups, while the peaks at 1250–1300  $\text{cm}^{-1}$  and 1150–1200  $\text{cm}^{-1}$  belonged to the asymmetric and symmetric stretching of the C–O–C groups, respectively [47]. Thus, the FTIR spectra of the

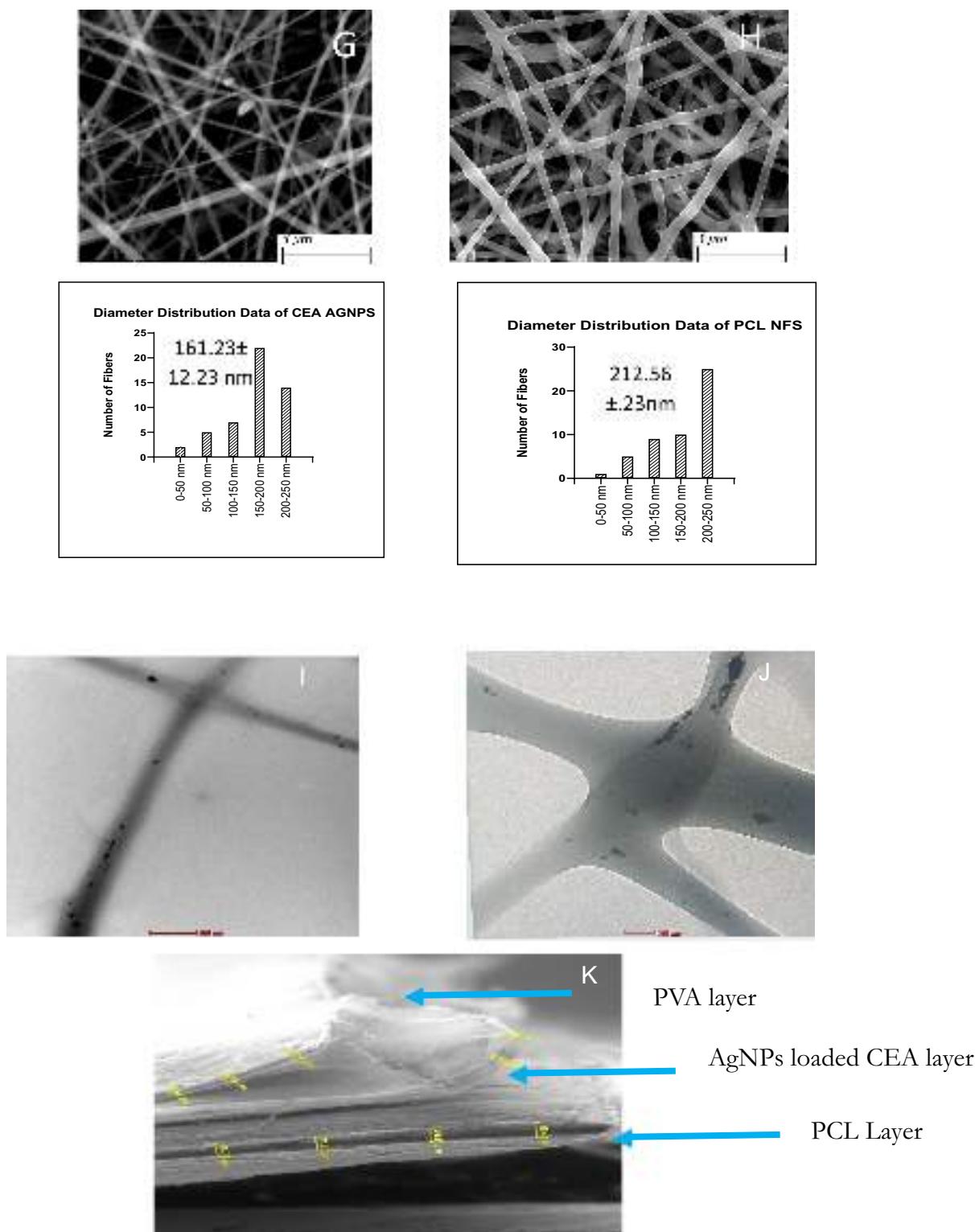


Fig. 1. (continued).

CEA NFs and the PCL NFs demonstrated the structural hallmarks as that of the pristine CEA and PCL, which suggested that there were no unwanted polymeric interactions that occurred during the electrospinning process.

### 3.4. Thermo-gravimetric analysis (TGA) of the nanofibrous mats

The thermal stability of the PVA, PVA NF, CA, PVA CA NF, CEA, CEA

NF, NF, PCL and PCL NFs and TNF was assessed using TGA analysis. The degradation thermograms have been depicted in Fig. 2B. The thermogram of PVA exhibited a three-stage degradation. The first loss of water molecules trapped in the hydrophilic PVA was observed at around 100 °C. The second loss occurred in the range of 200–380 °C, which was due to the loss of –OH groups and deacetylation of the PVA chains. The third degradation step was observed at 400–500 °C, which was attributed to the breakage of C–C and C–O bonds [48]. The thermogram of the

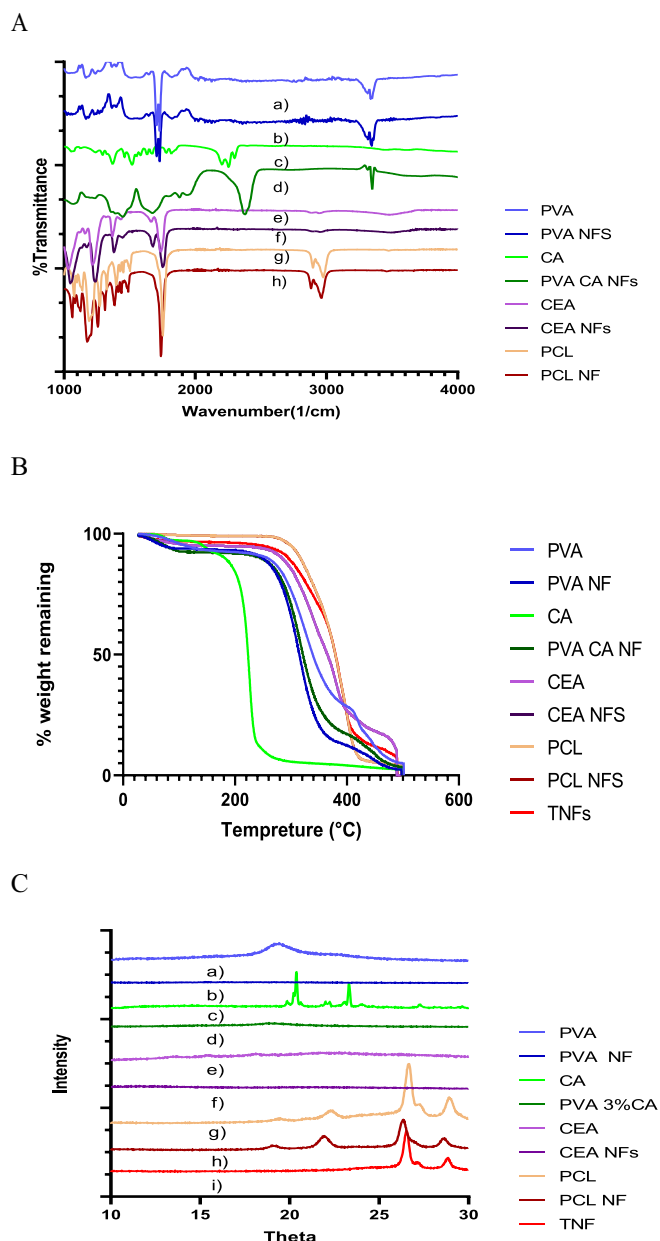


**Fig. 2.** A) Overlay of FTIR spectra of PVA, PVA NF, CA and PVA CA NF, CEA NF, PCL and PCL NF  
 B) Overlay of thermograms of PVA, PVA NF, CA, PVA CA NF, CEA, CEA NF, CEA AgNPs NF, PCL, PCL NF and TNF  
 C) Overlay of diffractograms of PVA, PVA NF, CA, PVA CA NF, CEA, CEA NF, PCL, PCL NF and TNF.

PVA NFs showed a similar degradation profile as that of the pure PVA. The thermogram of CA revealed that the thermal decomposition of CA occurred in a single step, at 150–230 °C [49]. However, the thermogram of the cross-linked PVA NFs indicated a better thermal stability as compared to the non-crosslinked PVA NFs, due to polymeric interactions between the free -OH groups of the PVA and the COOH groups of CA. As shown in Fig. 2B, the thermogram of pure CEA showed three degradation steps. The first loss from the hydrophobic CEA was observed at around 100 °C, which was attributed to the presence of moisture. The second intensive peak at 250–350 °C was observed due to the loss of -COO groups and deacetylation of CEA. The third degradation step was observed at 350–450 °C, which was attributed to the breakage of C—C and C—O bonds [50]. However, the thermal decomposition profile of the CEA NFs exhibited better thermal stability as compared to the native

CEA. The gravimetric analysis of PCL, PCL NFs, showed two stage degradation, as depicted in Fig. 2B. The first loss was observed in the range of 200–300 °C, due to the loss of C=O groups, while the second degradation step observed at 400–500 °C was attributed to the breakage of C—C and C—O bonds [51]. Thus, the spectra revealed that the PCL layer had greater thermal stability. The thermogram of TNF demonstrated slower thermal degradation and greater thermal stability, as compared to single polymeric sheets, which was attributed to the interaction between the polymers constituting the different layers during electrospinning, which led to polymer chain elongation.

### 3.5. X-ray crystallographic analysis

The crystalline or amorphous nature of PVA, PVA NF, CA, PVA CA NF, CEA, CEA NF, PCL and PCL NF were successfully studied using powder XRD, as shown in Fig. 4. The XRD of pure PVA (Fig. 2Ca) exhibited characteristics of crystalline and amorphous phases of conventional semi-crystalline polymers. It showed several distinct crystalline peaks at  $2\theta = 11.211^\circ$ ,  $19.450^\circ$ ,  $20.654^\circ$ ,  $23.520^\circ$  [52]. These peaks were not observed in the PVA NF (Fig. 2Cb), which indicated that the crystalline state of PVA was converted into an amorphous one after electrospinning. The X-ray diffraction pattern of pure CA (Fig. 2Cc) exhibited peaks at  $2\theta = 14^\circ$ ,  $19^\circ$ ,  $26^\circ$ , with high intensity [53]. However, no characteristic peaks were observed for CA at  $2\theta = 14^\circ$ ,  $19^\circ$ ,  $26^\circ$  in the cross-linked mats (Fig. 2Cd). The X-ray diffraction pattern of CEA exhibited peaks at  $2\theta = 14^\circ$ ,  $20^\circ$  and  $25^\circ$ , with slight intensity, as depicted in Fig. 2Ce [54]. However, no characteristic peaks were observed for CEA NF (Fig. 4f). Fig. 4g depicts the XRD patterns of PCL, with three significant diffraction peaks at  $2\theta = 21.3^\circ$ ,  $27^\circ$  and  $29^\circ$  [55], which were also observed in PCL NF (Fig. 2Ch). Thus, the XRD pattern of PVA, PVA NF, CEA and CEA NFs revealed that during the electrospinning process, the semi-crystalline and crystalline polymers were converted into the amorphous form, possibly due to polymer chain entanglement or polymer chain scission during electrospinning. However, the PCL NFs were able to withstand their crystalline structure even after electrospinning, which allowed for controlled release of AgNPs. Finally, the semi crystalline nature of the TNF mat was depicted by the diffraction pattern observed at  $2\theta = 29^\circ$  (Fig. 2Ci).

### 3.6. Water uptake by the nanofibers

The NFs' capacity to absorb water is essential for controlling nutrient delivery, infiltration, and cell adhesion. In the present study, the water absorption capacity of the PVA CA NF, CEA NF, CEA AgNPs NF, PCL and TNF mats were evaluated over 14 days. Fig. 3 shows the percentage of water uptake for fabricated nanofiber mats. The samples were weighed at specific time intervals and the percent weight gain was calculated. In case of all the NF mats, the water retention properties increased till 7 days. After 7 days, there was no significant increase in water retention by all the mats. This may have been due to the bonding between the free COOH groups of the cross-linked PVA with the OH groups of water. Since after 7 days there was saturation of the available COOH groups for interaction with the OH groups of water, there was a decrease in the water retention properties of the mats after a week [56]. Also, CEA NF without AgNPs exhibited greater water retention as compared to the CEA NF loaded with AgNPs. This was attributed to the bonding of AgNPs with the nano porous structure of the NF mats [57]. Also, PCL exhibited lower water retention as compared to the CEA NF due to its super-hydrophobic nature. However, the combination of these layers in the TNF sheets, loaded with AgNPs, resulted in water uptake capability of upto 200 %, till 15 days. There was no significant difference in the water uptake of PVA NF, CEA NF, CEA AgNPs, PCL NFs, as compared to TNF AgNPs ( $P > 0.05$ ). However, values obtained indicated that the fabricated sheet exhibited sufficient water uptake for wound healing applications [58].

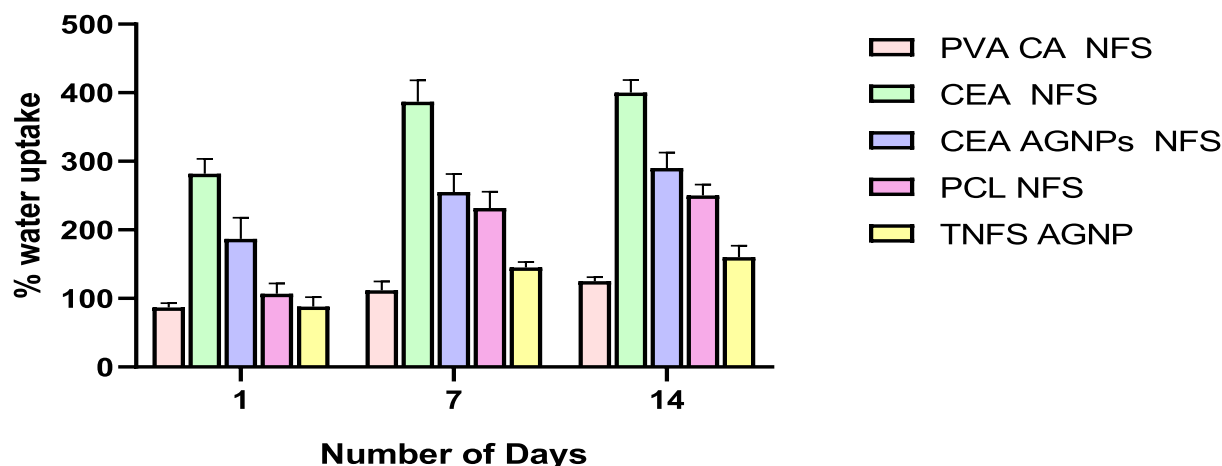


Fig. 3. Graphical Representation for water uptake study of PVA CA NF, CEA NF, CEA AgNPs NF, PCL NF and TNF.

### 3.7. Water vapor transmission rate

Reduction in the risk of and faster healing are largely dependent on the permeability of the wound dressings to absorb oxygen and wound exudates. The optimum dressing should be permeable enough to prevent excessive evaporation and collection of wound exudates, as this could cause the wound site to dry out and cause pain when the dressing is changed. [59]. The WVTR can be used to assess a dressing's capacity to reduce water loss. By using different wound dressings with varied WVTRs, the wound surface moisture can be controlled. Previous research indicates that the evaporation rate in healthy skin ranges from 204 to 250 g/(m<sup>2</sup>·day), but depending of the type of damage, it can reach 5000 g/(m<sup>2</sup>·day). According to research, the optimal weight-to-rapidity ratio (WVTR) for wound dressings to provide proper moisture retention at the wound site and avoid secretion accumulation is between 2000 and 2500 g/(m<sup>2</sup>·day) [60,61]. In the present investigation, the WVTR of the NF mats was evaluated using the water cup method, as reported in the literature, with slight modifications. The loss of weight of water was calculated at an interval of 24 h and transmission rate was evaluated. The values for WVTR for PVA CA NF, CEA NF, CEA AgNPs NF, PCL and TNF have been stated in Table 1. We concluded that the TNF sheet dressing with a WVTR of approximately 192.50 ± 3.189 g/m<sup>2</sup>/24 h g/m<sup>2</sup>/24 h could maintain the optimal moisture content required for cellular proliferation and functioning of human keratinocyte cells.

### 3.8. Porosity of nanofibrous sheets

The films' porosity, an essential structural component for biomedical applications, was assessed in the study. By examining the material's porosity, the nanofibrous dressing's absorption capacity was calculated. The porosity of dressings between 60 and 90 % permits oxygen permeability, cellular adhesion, migration, and proliferation for skin regeneration. It also inhibits bacterial infiltration [62]. On the other hand, wound dressings with a porosity of <60 % may prevent gas permeability, vascularization, cellular ingrowth, and nutrient diffusion, while those with a porosity of >100 % may find it more difficult for cells

Table 1

Water vapor evaporation rate and % porosity of PVA CA NF, CEA NF, CEA AgNPs NF, PCL NF, TNF.

Sample name	Water vapor transmission rate (g/m <sup>2</sup> /24 h)	% Porosity
PVA CA NF	192.70 ± 1.020	90.52 ± 2.42
CEA NF	192.30 ± 4.55	87.01 ± 1.36
CEA AgNPs NFs	191.2 ± 1.523	88.86 ± 2.72
PCL	200.8° ± 3.800	93.6 ± 1.70
TNF	192.50 ± 3.189	85.75 ± 1.80

to occupy the voids in the structure. [62]. In the present study, porosity of PVA CA NF, CEA NF, CEA AgNPs NF, PCL and TNF were investigated using liquid displacement method. Incorporation of AgNPs increased porosity of CEA NF due to reduction in water uptake of CEA AgNPs NFs, which in turn may significantly affect the wettability, biocompatibility, and cell growth over the nanofibers [57,63]. The porosity values of PVA CA NF, CEA NF, CEA AgNPs NF, PCL and TNF have been stated in Table 1, which revealed that the fabricated NF mats had appropriate porosity for wound healing properties.

### 3.9. Contact angle measurement

The hydrophilic and hydrophobic properties of the NF mats was successfully measured and has been shown in Fig. S4. The contact angle for PVA NF, CEA NF and PCL layer were found to be 36.88°, 65.59°, and 106.9.0°. Thus, the top layer of the TNF mat was hydrophilic due to the presence of PVA, the middle layer was hydrophobic because of the presence of CEA, while the bottom layer was super hydrophobic because of the presence of PCL. The contact angle of the TNF was found to be 55.66°. Since, the inner layer of PCL shows hydrophobic behaviour, it would play an imperative role in significant adhesion of cells and protect the mats from getting wet, rendering the TNF mat suitable for wound healing applications.

### 3.10. In vitro degradation studies

The presence of enzymes in biological fluid cause the NFs to begin deteriorating as soon as it comes into touch with bodily fluids. Therefore, prior to doing an *in vivo* investigation, it is imperative to examine the material's *in vitro* deterioration. Examining the rate of degradation and the amount of time needed for the produced NF mats to degrade, as well as whether the mats could last the 15 days needed for natural skin regeneration, was the primary goal of the *in vitro* degradation analysis. The degradation of mats was studied in a medium containing the enzyme that is present at the wound sites. The medium was chosen to mimic the natural environment (pH) of the body fluids. The mats were incubated at 37 °C in phosphate buffer saline having a pH of 7.4, which contained chicken lysozyme (10,000 U/mL in PBS). The degradation was analysed on days 1, 7, and 14 by measuring the loss of their initial mass of the NF mats. Fig. 4 depicts the degradation percentage of the PVA CA NF, CEA NF, CEA AgNPs NF, PCL NF, TNF. The PVA CA NF demonstrated faster degradation rate, as compared to the CEA and PCL NF mats, due to the hydrophilic nature of the PVA. Fascinatingly, due to cross-linking of the PVA NF, they were able to maintain its stability till 15 days. The PCL NF exhibited slower degradation rate as compared with the other NF mats due to its superhydrophobic nature. While the



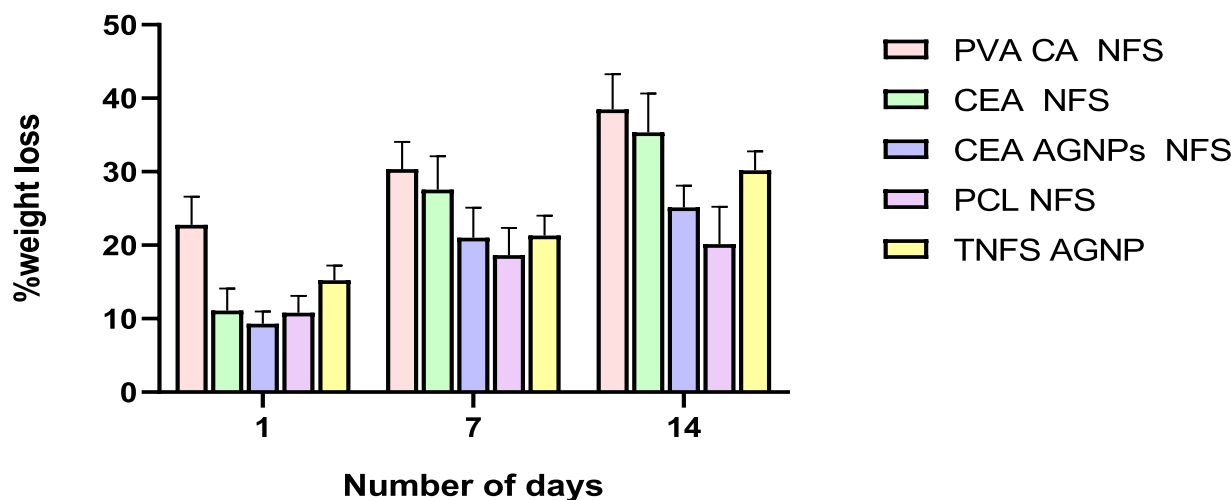


Fig. 4. Graphical Representation for *in vitro* degradation study of PVA CA NF, CEA NF, CEA AgNPs NF, PCL NF and TNF.

CEA NF mat exhibited a moderate degradation rate. The degradation rate for AgNPs loaded NF mat was lower than that of the CEA NF alone. This was due to the fact that the addition of nanoparticles produced intermolecular polymeric connections that shielded the polymer incision sites from the fluid seeping through the mats. As the nanocomposites increased, they acted as a diffusion barrier that hindered the swelling and prevented the degradation of NF mats [54]. The TNF showed faster degradation initially due to the direct interaction between the hydrophilic PVA layer with the medium. However, the presence of hydrophobic polymers in the TNF mat was able to prevent its rapid degradation. Unlike water uptake study, the degradation profile of PVA NF, CEA NF, CEA AgNPs, PCL NFs was not significantly different than that of the TNF AgNPs ( $P > 0.05$ ). Thus, there was a strong correlation between the water uptake investigation and the *in vitro* degradation study. It was also expected that the material's breakdown would facilitate the creation of fresh extracellular matrix (ECM) at the site of the wound, by creating space for tissue growth and differentiation.

### 3.11. Mechanical strength analysis

Until the wound heals, the wound dressing must shield it from all types of external stress. Furthermore, especially when treating wounds close to joints, the wound dressing needs to be flexible enough to move with the body while staying in place. To encourage the best possible healing of the injured tissues, it is essential to choose a dressing with the appropriate mechanical properties. The mechanical strength of the PVA NF, PVA CA NF, CEA NF, CEA AgNPs NF, PCL NF and TNF were studied using a electroforce 5500 model (TA, instruments USA). Several studies have reported varying values of tensile strengths, ranging from 0.7 to 18.0 MPa, as being sufficient for dermal cell culture [64,65]. The mechanical strength of PVA, PVA CA NF, CEA NF, CEA AgNPs NF, PCL NF and TNF were observed as  $2.88 \pm 0.25$  M. Pa,  $6.82 \pm 0.37$  M. Pa,  $1.22 \pm 0.0.35$  M. Pa,  $1.55, 1.55 \pm 0.45$  M. Pa,  $11.90 \pm 0.77$  M. Pa and  $12.70 \pm 0.606$  MPa, respectively. The mechanical strength for PVA CA NF and CEA AgNPs showed significant difference ( $P < 0.05$ ). Also the mechanical strength of middle CEA AgNPs, in comparison with TNF containing PCL layer, showed a significant difference ( $P < 0.05$ ) which confirmed that PCL imparted a high mechanical strength to TNF due to its super-hydrophobic nature which is required for tissue engineering applications. Asghar Eskandarian et al. investigated the mechanical strength of a single-layered, propolis embedded polyurethane-hyaluronic acid (PU-HA/1 % EEP) nanofibrous wound dressing and a bilayered wound dressing composed of dense polyurethane/propolis membrane and a biodegradable polycaprolactone/gelatin nanofibrous scaffold (PU/EEP-PCL/Gel). The mechanical strengths were observed as

$4.86 \pm 0.9$  MPa and  $5.6 \pm 0.6$  MPa, respectively [66,67]. However, the mechanical strength of triple-layered nanofiber dressing was significantly higher than the dressings reported earlier, which confirmed its suitability for healing chronic wounds like that due to diabetic foot ulcer etc. Thus, the triple-layer dressing was distinctly more advantageous for chronic wounds than other reported dressings due to the unique characteristics of each of its layers.

### 3.12. Evaluation of cellular toxicity using MTT assay

The *in-vitro* cytotoxicity of PVA NFs, PVA CA NFs CEA NFS, AgNPs loaded CEA NFs, PCL NFs and TNF were assessed using MTT assay. Human fibroblast cells and keratinocytes cells were used for these studies. Human fibroblast cells are present in dermal layer of skin, which play an imperative role in secretion of collagen and other proteins that maintain the extracellular structure of the skin. While the keratinocytes are present in the epidermal layer of the skin and prevent the skin from environmental damage due to heat, pathogenic bacteria. Thus, an ideal wound dressing should be biocompatible with these skin cells. The cytotoxicity of the fabricated mats have been depicted in Fig. 5A and B. The cell viability with PVA NFs, PVA CA NFs CEA NFS, AgNPs loaded CEA NFs, PCL NF sand TNF were observed as  $97.75112 \pm 2.33$  %,  $97.77661 \pm 2.8$  %,  $94.4028 \pm 1.48$  %,  $98.90055 \pm 1.07$  %,  $93.45327 \pm 2.6$  %,  $99.17 \pm 1.6$  %, respectively, in case of the HDF cells. While in case of the HeCat cell, these values were  $80.47337 \pm 1.01$  %,  $72.51 \pm 1.216$  %,  $78.6 \pm 4.2$  %,  $91.6 \pm 1.95$  %,  $79.0 \pm 1.52$  %,  $76.9 \pm 5.23$  %, respectively, for PVA NFs, PVA CA NFs CEA NFS, AgNPs loaded CEA NFs, PCL NF sand TNF. As per ISO 10993-5 [68], if a material shows cell viability of  $>70$  %, it is considered as non-toxic for medical application. Thus, the MTT data indicated that the fabricated nanofiber dressings were safe for application over the wound sites.

### 3.13. Cellular proliferation study using EZ blue assay

The cellular proliferation with PVA NFs, PVA CA NFs CEA NFS, AgNPs loaded CEA NFs, PCL NFs and TNF were assessed using EZ Blue assay and HaCaT and HDF cells, considering the end-application of NF mats in wound healing. The growth of HaCaT and HDF cells was studied on days 1, 2 and 3. In the EZ Blue™ cell assay, the mats were observed to serve as good templates for cell proliferation. The percentage of cell proliferation was calculated by comparing the proliferation of the cells recorded at 24 h with that observed at 48 and 72 h., as depicted in Fig. 6A and B. The proliferation data showed that all the samples showed significant increase in cell viability after 48 h, upto 150 %, in case of both the cell types. The cell proliferation for PCL layer was found to be



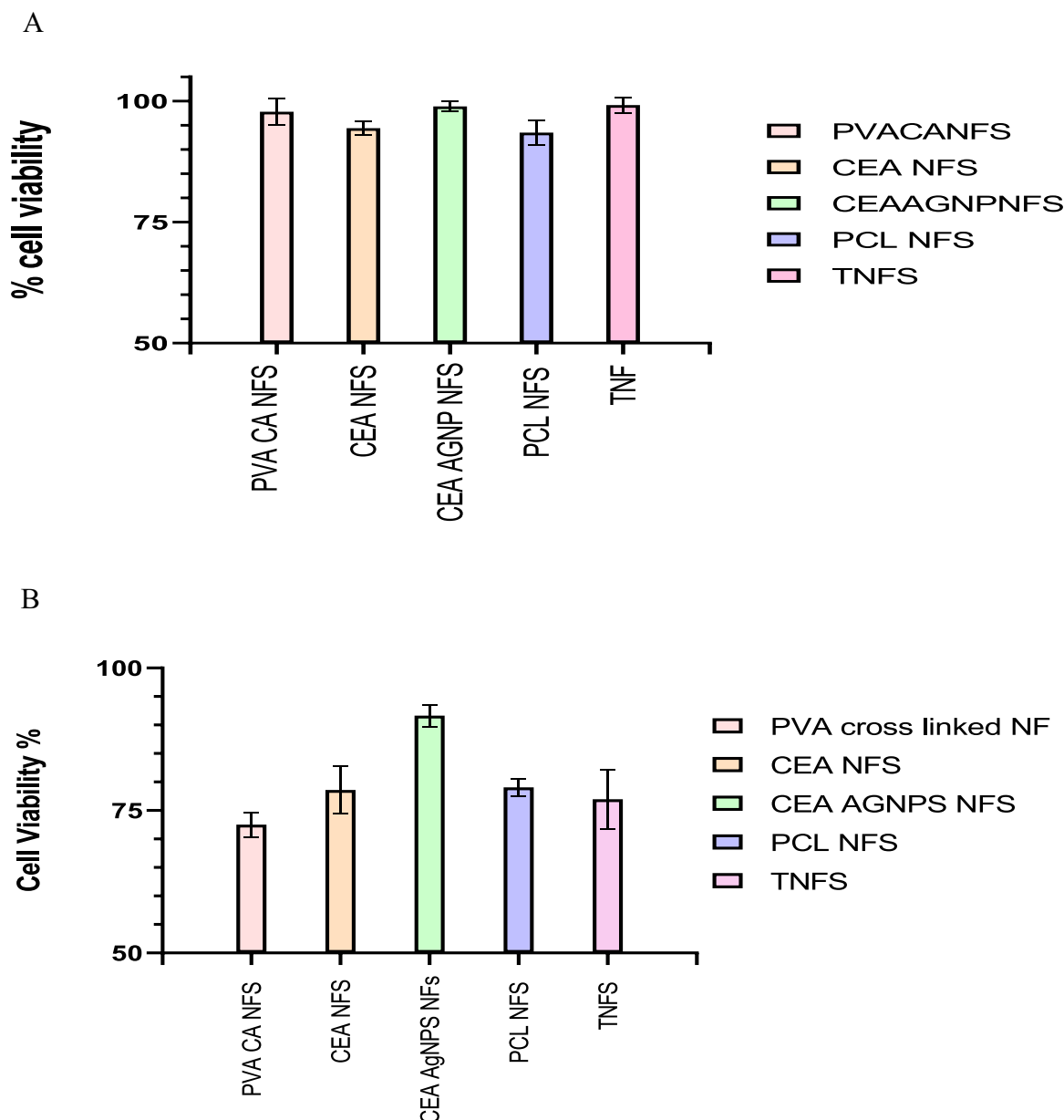


**Fig. 5.** A Graphical Representation for cellular cytotoxicity studies for PVA NF, PVA CA NF, CEA NF, CEA AgNPs NF, PCL NF and TNF against HDF cells  
**Fig. 5B** Graphical Representation for cellular cytotoxicity studies for PVA NF, PVA CA NF, CEA NF, CEA AgNPs NF, PCL NF and TNF against HecA cells.

maximum in comparison with the cross-linked PVA layer and CEA NF, possibly due to the superhydrophobic nature of PCL, which may have allowed the cells to adhere well and support their growth. The cell proliferation in case of TNF was comparable to the that of PCL, as PCL layer was used as the bottom layer in the TNF mat for its significant adhesion and painless removal. Thus, this investigation confirmed that the fabricated NF mats were appropriate for cell growth and proliferation and henceforth rapid wound healing [69].

#### 3.14. Thrombin generation assay to assess the haemostatic activity

A sensitive and precise marker used to analyse the thrombin production in blood over time is the thrombin-antithrombin (TAT) complex. The ELISA (Enzyme Linked Immunosorbent Assay) kit for thrombin-antithrombin complex (TAT) human *in vitro* is intended for the quantitative evaluation of thrombin-antithrombin complex quantities in plasma. Here, a specific antibody is pre-coated onto the 96-well plates and blocked. In this investigation, the quantification of the thrombin-

antithrombin complex was carried out to provide information about the coagulation process with the NF mats. The dressing material comes into direct contact with the wound and stops the blood flow *via* coagulation of blood at the wound sites. In order to ascertain how the developed dressing material will react to the coagulation process, the TAT test was carried out. Over the course of 1 h, the amount of thrombin produced by the plasma incubated with the dressing material was measured in ng/mL and compared to the standard, namely gauze. The TAT analysis results are shown in Fig. 7, which shows that the electrospun mats effectively generated thrombin in comparison to the untreated and gauze-treated blood samples. Accordingly, the study suggested that the presence of polymeric NF mats may enhance thrombin synthesis and cause blood clotting, which would then promote successful wound healing [70].

#### 3.15. Loading and release characteristics of AgNPs

Before examining the silver release properties from the TNF mat

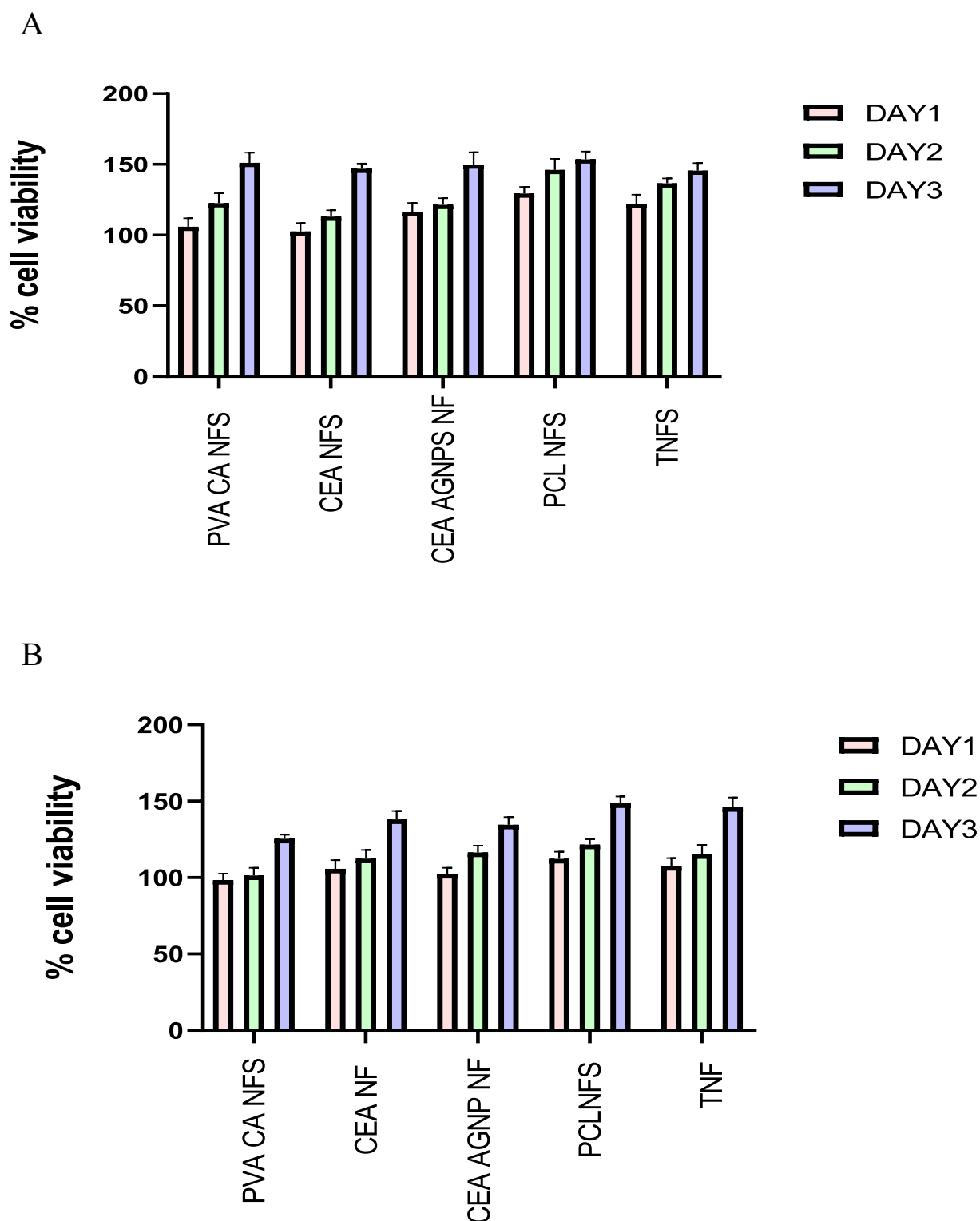


**Fig. 6.** A Graphical Representation for cellular proliferation studies for PVA CA NF, CEA NF, CEA AgNPs NF, PCL NF and TNF against HDF cells  
 B Graphical Representation for cellular proliferation studies for PVA CA NF, CEA NF, CEA AgNPs NF, PCL NF and TNF against HacaT cells.

containing AgNPs, the amount of silver loaded in the mats was calculated, and for the TNF mat made with 200 ppm of the AgNPs, the result was  $0.524 \text{ mg/mL}$  considered as  $99.89 \pm 1.10 \%$  of the initial AgNPs content added to the electrospinning solution was accounted for by this. The release characteristics of Ag<sup>+</sup> ions from TNF containing AgNPs was investigated by total immersion method, in PBS (pH 7.4) containing lysozyme (10,000 U/mL). The *in vitro* AgNPs release profile

from the NF mat was observed as shown in Fig. 8. The profile exhibited an initial burst release, followed by a controlled release of AgNPs from the CEA NF in PBS, over time. Over the first 8 h, 30–40 % of AgNPs were released, followed by a controlled release of upto 65 % till 7 days. Thus, controlled release of AgNPs from TNF may prevent the wound from bacterial infection and hence support in wound healing. As indicated in Table 2, the release parameters, namely *n*—release exponents—release

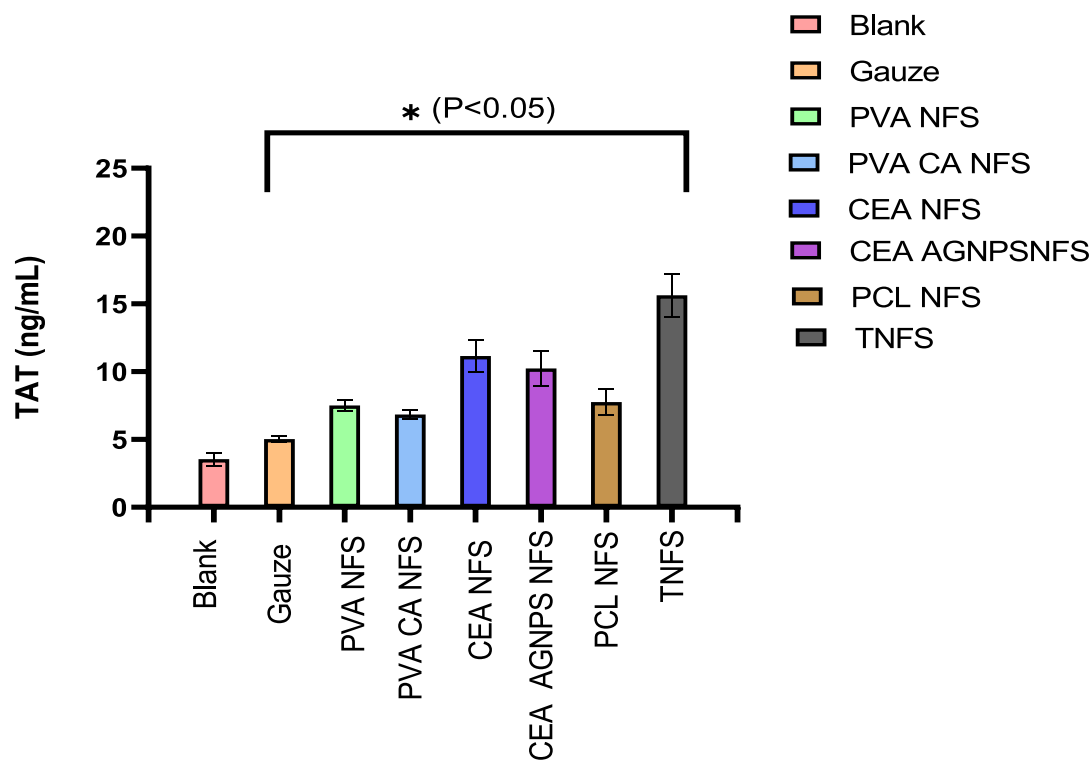


**Fig. 7.** Graphical Representation for thrombin generation using TAT assay for PVA, PVA NF, PVA CA NF, CEA NF, CEA AgNPs NF, PCL NF and TNF in comparison with gauze  
(\*) represented a *p* value of <0.05, indicating its significant difference as compared to the controls.

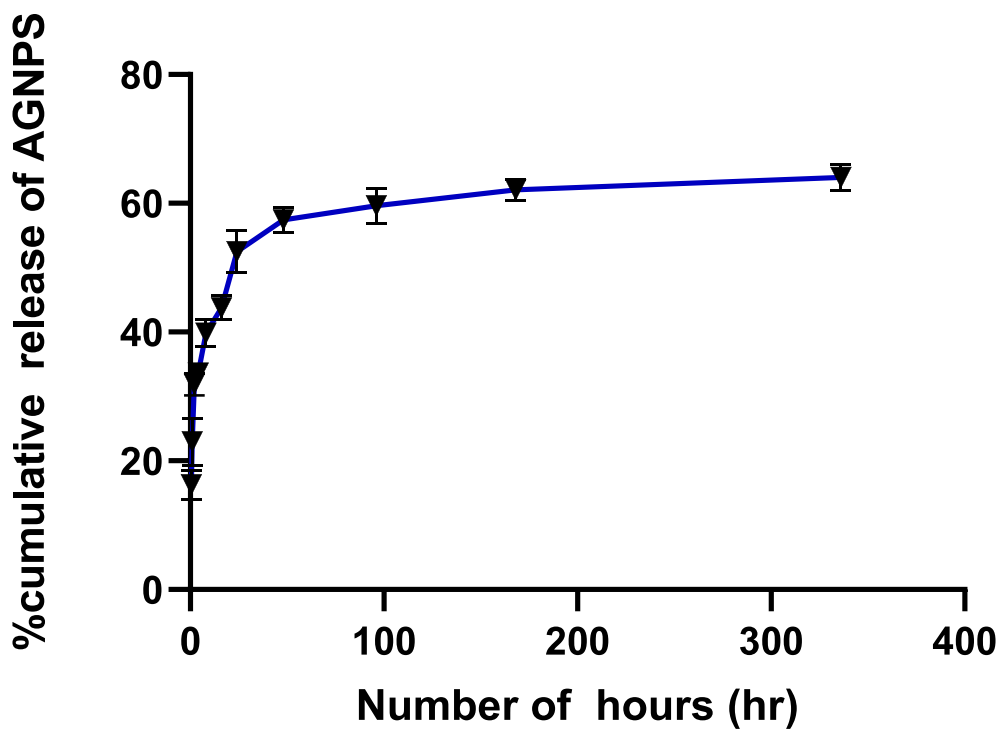


**Fig. 8.** Graphical representation for release of AgNPs through TNF.

rate constant; and  $r^2$ —regression coefficient, were primarily considered in order to comprehend the mechanism of AgNPs. The best fit model was chosen based on goodness of fit, and it explained the anomalous release by releasing, diffusing, and eroding the polymeric matrix in that order [71].

**3.16. Antibacterial evaluation**

Using the disc diffusion method, the bactericidal activity of TNF loaded with AgNPs (200 ppm) was evaluated. The activity was conducted against common wound-associated microbes namely *Escherichia*

**Table 2***In vitro* drug release kinetic models and regression output for AgNPs release from TNF.

Sample	Dissolution Medium	Percent Drug Released* (24 h)	Release Exponent (n)	Drug Transport Mechanism	Release Constant (k)	Regression ( $r^2$ )	Best Fit release Model
AgNPs in TNF	PBS (7.4)	52.47	0.6717	Anomalous Transport	12.1644	0.850	Hix. Crow

*coli* (*E. coli*) and *Staphylococcus aureus* (*S. aureus*). As a control, the activity of AgNPs suspension at a comparable concentration was employed. After analysis, it was discovered that the diameters of the zones of inhibition, which indicate the death of the organisms, were  $2.5 \pm 0.23$  for AgNPs and  $1.98 \pm 0.12$  for TNF against *E. coli*, and  $2.06 \pm 0.16$  for AgNPs and  $1.76 \pm 0.09$  for TNF against *S. aureus*, respectively. Three studies were conducted in duplicate. The anti-bacterial activity of single layered a propolis embedded polyurethane-hyaluronic acid (PU-HA/1 % EEP) and the bilayered wound dressing composed of a dense polyurethane/propolis membrane and a biodegradable polycaprolactone/gelatin nanofibrous acafold (PU/EEP-PCL/Gel) were investigated using disc diffusion method. Results indicated a zone of inhibition of  $5.4 \pm 0.3$  mm and  $2.36 \pm 0.33$  mm against *Staphylococcal aureus* and  $1.9 \pm 0.4$  mm and  $3.18 \pm 0.63$  mm against *Escherichia coli* with PU/EEP-PCL/Gel and PU-HA/1 % EEP dressings, respectively, which was comparable to our triple layered dressing [66,67]. The AgNPs may have acted through the following mechanism. Initially, the AgNPs were slowly released from the polymeric matrix of the triple layered dressing. Further, due to electrostatic interaction between the positively charged AgNPs and the negatively charged bacterial cell membrane, the AgNPs remains adhered to the membrane surface of the microbial cells, by modifying the lipid bilayer and increasing the membrane permeability, and were subsequently taken up by the cells. Further the AgNPs

were oxidized in the aqueous environment of cytoplasm, in presence of oxygen, and generated reactive oxygen species and free radicals, which could have caused damage to the intracellular micro-organelles like mitochondria, ribosomes and vacuoles, and also biomolecules including DNA, protein, and lipids and cause the cell death [72]. Additionally, the activity of AgNPs towards gram-negative and gram-positive bacteria differed due to differences in their structural hallmarks. The cell walls of gram-negative bacteria are mostly composed of lipopolysaccharide (LPS) and L-a-phosphatidyl-ethanolamine (PE), two amphiphilic macromolecules that are found in lesser amounts in the gram-positive bacteria. Since LPS and PE prevent AgNPs from interacting with cell membranes, these AgNPs were less effective against gram-negative bacterium than gram-positive bacterium used in our study. [73]

### 3.17. Wound area measurement

The effectiveness of artificially generated AgNP-loaded TNF nanofibrous mats for wound healing was assessed by contrasting them with commercially available cotton gauze, a conventional dressing. The rats with open wounds were considered the negative control group, and the rats treated with cotton gauze were considered the positive control group. The wound areas on days 0, 3, 7, 10 was measured for all the groups and the rate of wound healing was calculated as shown in Fig. 9.

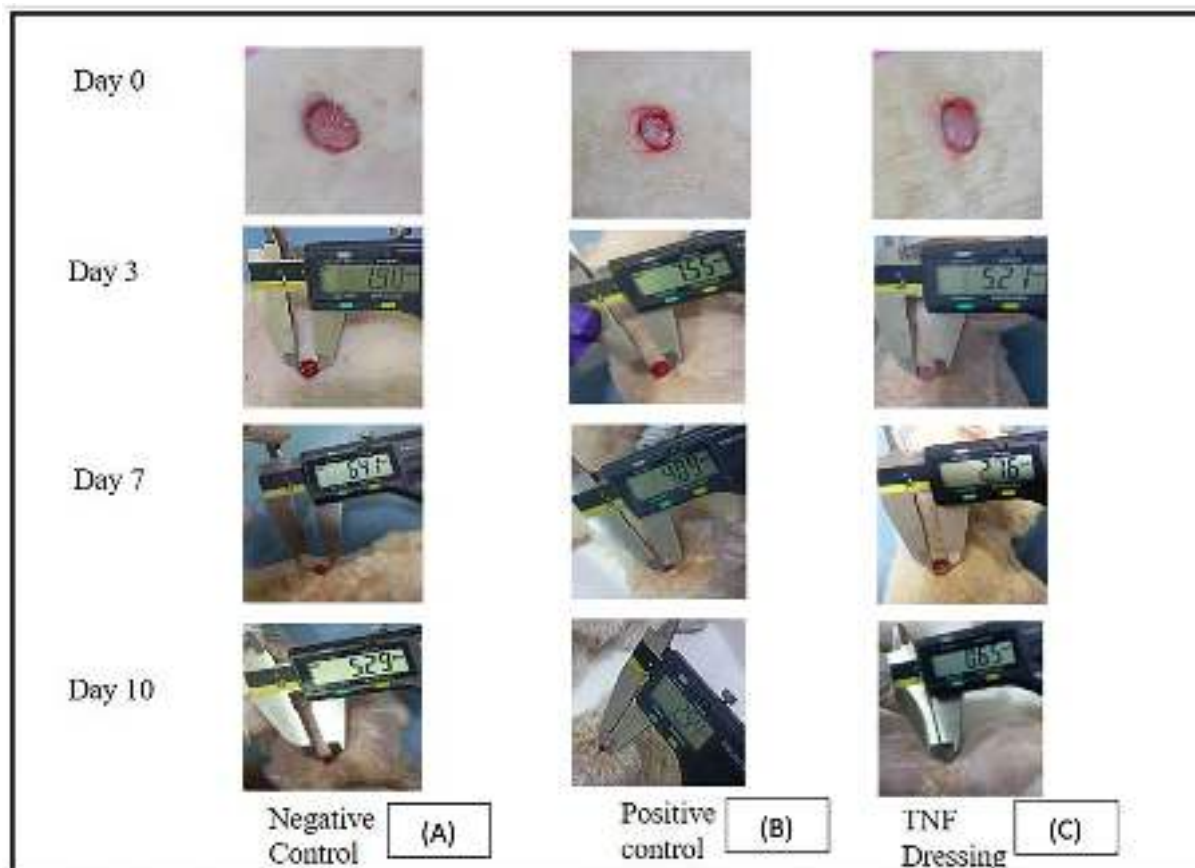


**Fig. 9.** Photographs of an *in vivo* wound healing study. A group is negative control, B group is positive control and C TNF with AgNPs.

On day three, the rate of wound healing with AgNPs loaded TNF dressing was 64.19 %, compared to 53.18 % and 10.54 % for the positive control group and negative control groups, respectively. On day 7, the positive control group (60.94 %) and the negative control (28.55 %) had worse wound healing rates than the AgNPs loaded TNF nanofibrous dressing (80.28 %). Day 10: The group with AgNPs loaded TNF nanofibrous dressing had the highest wound healing rate of all the groups, at 90.28 %. In Fig. 10, the wound healing rate was greater in the AgNPs loaded TNF dressing group than in the negative control group ( $p$ ,  $0.0160 < 0.005$ ). As a result, TNF nanofibrous dressing covered with AgNPs showed promise for usage as a wound dressing in contrast to cotton gauze, a conventionally marketed treatment. The dressing's high surface area-to-volume ratio and nanofibrous composition, which may have led to increased absorption of the wound exudates, were credited with promoting this better healing. Moreover, the hydrophilic polymer of the uppermost PVA CA NF layer more effectively absorbed the wound exudates. While the PCL layer's porous structure may have preserved optimal cellular respiration and water and gas permeability, preserving a moist environment at the wound site, the CEA layer containing AgNPs demonstrated a better degree of therapeutic efficacy. Consequently, when taken as a whole, the multipurpose nature of every TNF dressing layer. Thus collectively, the multifunctionality of each layer of the TNF dressing may have resulted in more effective wound healing as compared to the traditional gauze. Asghar Eskandarian et al. investigated the *in vivo*-efficacy of a single layered, propolis embedded, polyurethane-hyaluronic acid (PU-HA/1 % EEP) nanofibrous wound dressing in a Wistar rat wound model. A full thickness model was created and monitored for 21 days. After 21 days, the wounds treated with PU-HA/1 % EEP exhibited a higher closure of upto 97 %. Fascinatingly, wound specimen histologically examined on the 21st day, after treatment with PU-HA/1 % EEP, demonstrated well-developed dermis, with presence of hair follicles and lower number of inflammatory cells, in comparison with the other groups. Furthermore, PU-HA/1 % EEP resulted in formation of more densely packed collagen fibres, with a parallel arrangement in the extracellular matrix, in comparison with the other groups, which was confirmed by Masson's trichrome staining. Additionally, Asghar Eskandarian et al. also investigated the *in-vivo* efficacy of a bilayer wound dressing composed of a dense polyurethane/propolis membrane and a biodegradable polycaprolactone/gelatin nanofibrous scaffold (PU/EEP-PCL/Gel), in a Wistar rat wound model. Full-thickness defects (11 mm  $\times$  11 mm) were created on the back of the

mice and monitored for 15 days. On the 15th day, the bilayered PU/EEP-PCL/Gel wound dressing treated group exhibited approximately 100 % healed and closed wounds. Additionally, haematoxylin and eosin staining of bilayered PU/EEP-PCL/Gel group specimens exhibited a significantly developed dermis, in comparison with the control specimens, due to the presence of a lower number of inflammatory cells and development of more hair follicles. Also, the specimens stained with Masson's trichrome stain confirmed more collagen deposition, which may have played a critical role in the healing process, by providing a scaffold for skin cells [66,67].

### 3.18. Haematoxylin and eosin/Masson's trichrome staining

Haematoxylin, a complex form of aluminium ions, and oxidized haematoxylin, which imparts blue color to the cellular nuclei and keratohyalin granules, are used in the Haematoxylin and Eosin (H & E) staining procedure. After nuclear staining, eosin is used as a counter-stain, giving the eosinophilic and other structures pink and red hues. In order to stop the tissue from degrading, three samples of rat skin one from an open wound, one treated with AgNPs-loaded TNF, and one cotton gauze dressing were sliced into five-by-five centimetres and put in a 10 % formalin solution. After the tissue was embedded in paraffin blocks, paraffin slices were produced on slides for H&E staining. After then, these slides were examined under a microscope. The histological pictures of the injured tissue at day 10 are displayed in Fig. 11 for the following three groups: A) negative control (open wound), B) positive control (cotton gauze group), and C) AgNPs loaded TNF. Histological studies demonstrated that in the case of the negative control group Fig. 11 A, there was mild re-epithelization of the stratified squamous epithelium maturation with less formation of the keratinised layer. There was presence of a few fibroblast cells along with multifocal area of proliferation, focal area of re-epithelization, multifocal area of angiogenesis, focal area of proliferation fibroblast, which suggested that the wound was in proliferation stage. Fig. 11B shows moderate reepithelization of the stratified squamous epithelium with multifocal area of the stratified squamous epithelium maturation, with complete proliferation of fibroblasts and multifocal area of angiogenesis, along with slight formation of thin and thick bundle of collagens. While Fig. 11 C showed complete re-epithelization of stratified squamous epithelium along with complete maturation of collagen fibres, multi-focal area of angiogenesis with complete proliferation of fibroblasts. Furthermore, the

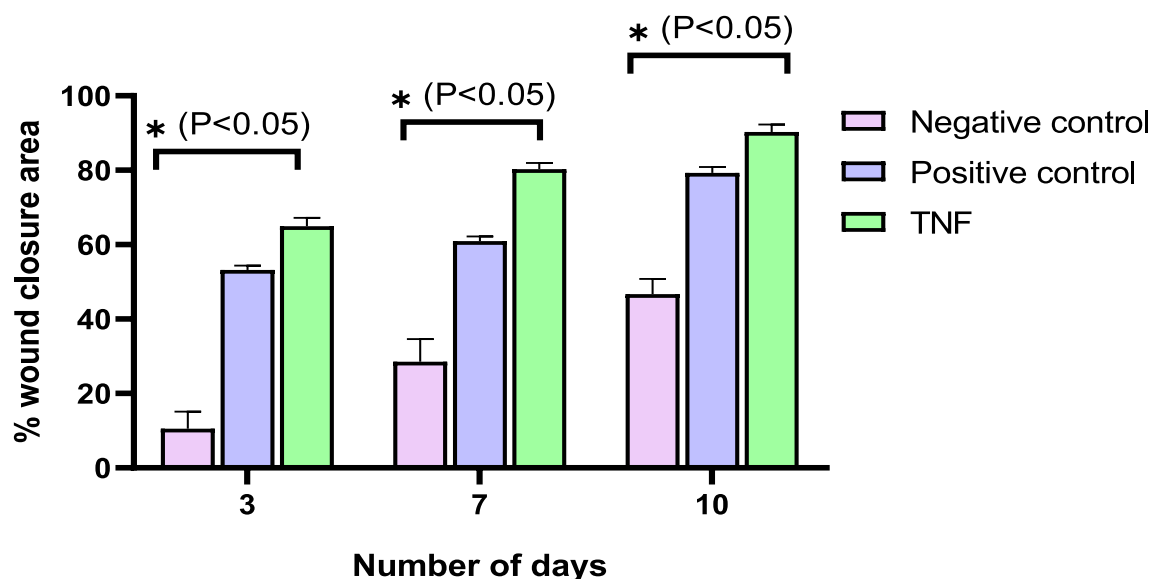


**Fig. 10.** Comparison of wound healing rate of TNF with AgNPs with positive control (cotton gauze) and negative control (open wound). Wound healing rate| (\*) represented a  $p$  value of  $< 0.05$ , indicating its significant difference as compared to the controls.



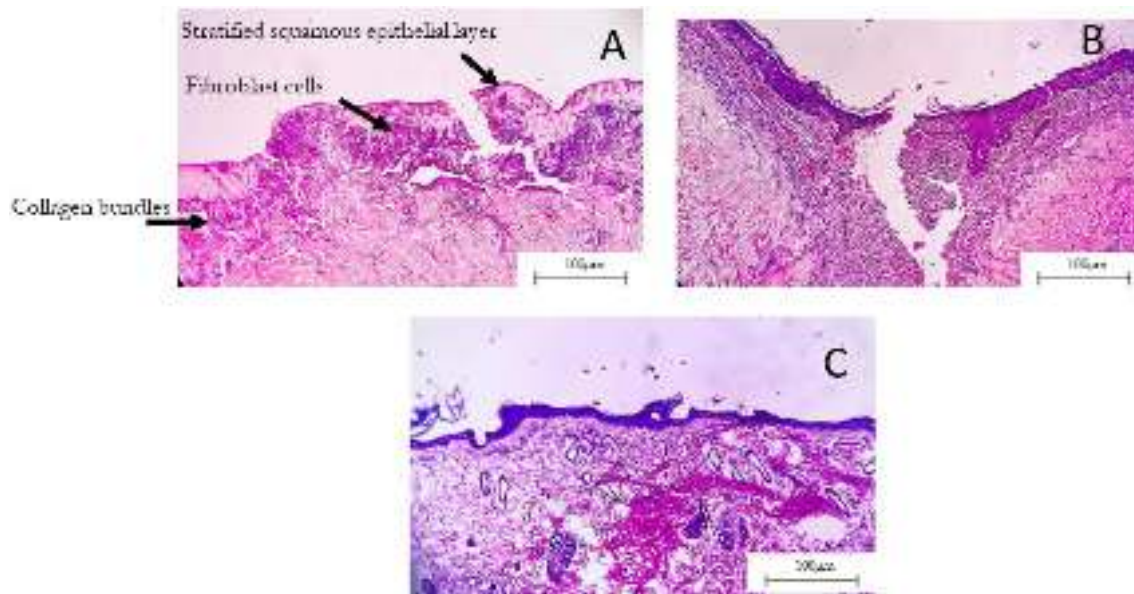


**Fig. 11.** Images for H and E staining of (A) negative control group, (B) positive control and (C) TNF with AgNPs. Group A) shows re-epithelization of the stratified squamous epithelium with angiogenesis, Group B) shows maturation of re-epithelization of the stratified squamous epithelium with multifocal area of proliferation of, formation thin and thick bundles of collagen Group C) shows complete re-epithelization of the stratified squamous epithelium, with proliferation of fibroblast, homogenous deposition of thin and thick collagen bundles with angiogenesis.

development of an unbroken keratinized layer in the epidermis indicated that the wound healing maturation stage had complete. [74]. Thus, the study concluded that AgNPs loaded TNF exhibited the fastest and the most efficient wound-healing, much superior to the traditional dressing material, via a natural healing mechanism (Fig. 11).

In addition, the wound site's collagen deposition (blue) was evaluated using Masson's Trichrome staining (Fig. 12). Fig. 12 A shows that there was initiation of formation of thin and thick bundle of collagen

fibres with no inflammatory cells, it showed the presence of collagen (blue), probably because of the presence fibroblast cells and the collagen deposition was scanty and still in nascent stages which indicated that the wound was at proliferation phase, which was complimentary to the results of the H and E staining. While Fig. 12 B showed complete maturation of collagen fibres, and more pronounced and homogenous collagen deposition was observed, with highest collagen deposition along with the formation of myofibroblast formation at the wound site.

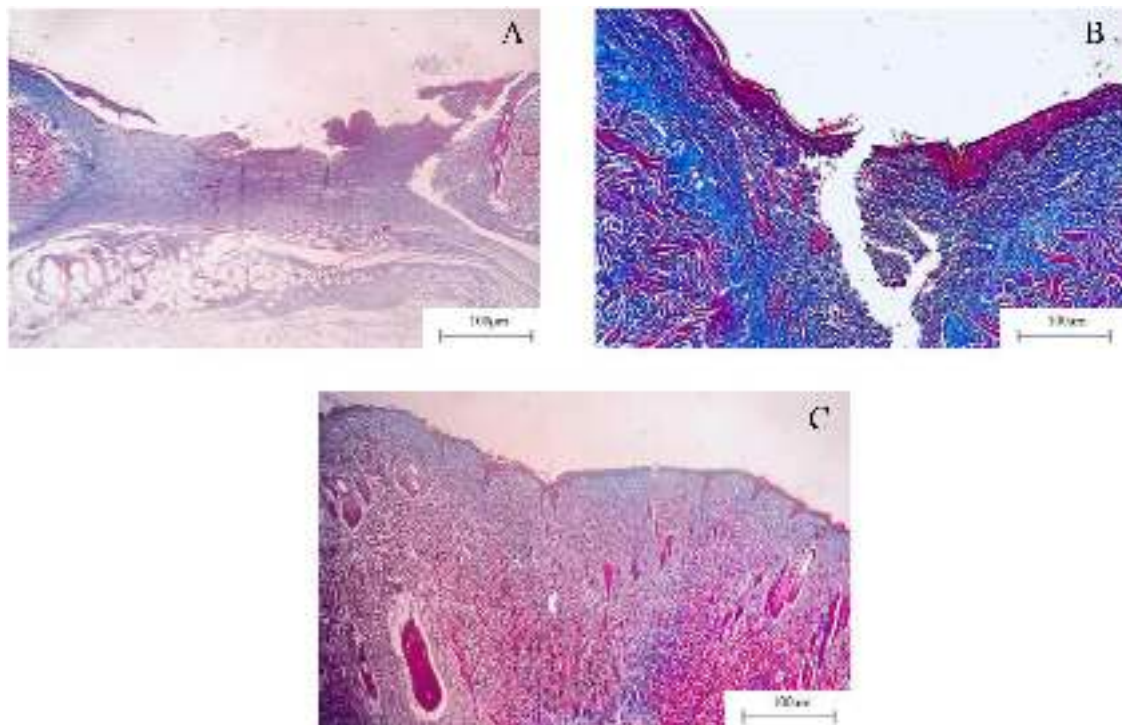


**Fig. 12.** Images for Masson's Trichrome staining of (A) negative control group, (B) positive control and (C) TNF with AgNPs. Group A) shows formation of thin and thick bundle of collagen fibres with no inflammatory cells Group B) shows complete maturation of collagen fibres, and more pronounced and homogenous collagen deposition Group C) shows mature collagen formation and more hair follicles.

In comparison to the open wound and the wound treated with gauze, the wound treated with AgNPs loaded TNF (Fig. 12 C) showed lower collagen content at the wound area, which might be due to more mature collagen formation and more hair follicles being regenerated, additionally formation of muscle tissue (red) was also observed which also indicated the initiation of the remodelling phase [75]. Thus, overall, the study confirmed that the novel TNF dressing containing AgNPs could be a promising candidate for wound healing applications, as an “all-in-one” solution.

#### 4. Conclusion

In conclusion, we have fabricated a highly biocompatible, hemocompatible, biodegradable, antibacterial, atraumatic nanoengineered triple layered wound dressing bandage to exhibit multiple healing functions. The top-most PVA CA layer was able to prevent dehydration and provide excellent mechanical strength to the middle therapeutic layer. The middle layer, loaded with AgNPs, showed controlled drug release. Use of CEA in the middle layer resulted in controlled water uptake, vapor evaporation to maintain moist environment at the wound site by absorbing and retaining wound exudates, and promoted excellent oxygen permeability and fluid drainage to speed up wound healing. While the PCL layer resulted in better adhesion to the skin cells and exhibited potential to avoid painful removal. The NF mats demonstrated highly effective antibacterial activity against Gram-positive (*S. aureus*) and Gram-negative (*E. coli*) bacteria; additionally, the porous structure of the PCL layer may mimic the properties of the skin's extracellular matrix. The potential of the nanofibrous mat in full-thickness wound healing was further confirmed by H&E, Masson's trichrome staining and *in vivo* excisional wound contraction. Thus, a triple layered AgNPs loaded PVA/CEA/PCL nanofibrous mat acted as a multi-functional dressing to accelerate wound healing and also demonstrated potential for other tissue engineering applications.

#### CRedit authorship contribution statement

**Shailesh Dugam:** Writing – original draft, Methodology, Investigation, Formal analysis, Conceptualization. **Ratnesh Jain:** Supervision, Resources. **Prajakta Dandekar:** Writing – review & editing, Supervision, Resources, Conceptualization.

#### Declaration of competing interest

The authors declare that they have no known competing financial interests or personal relationships that would influence the work reported in this paper.

#### Data availability

Data will be made available on request.

#### Acknowledgements

The authors are thankful to the Department of Science and Technology, Government of India for providing the funds under scheme DST - Nanomission [DST/NM/NB/2018/122(C) 16-12-20 19] for the execution of the project and for funding instruments (Electroforce 5500, NanoDSC). The authors are also thankful to DSTC-PURSE (PURSE program 2020; TPN-57255 for laboratory instruments and infrastructure. The authors are thankful to Prof. Ravindra Adivarekar from the Department of Fibres and Textile Processing Technology, ICT Mumbai, for allowing access to FTIR and TGA analysis. Shailesh Dugam is thankful to DST-India for the Inspire Fellowship.

#### Appendix A. Supplementary data

Supplementary data to this article can be found online at <https://doi.org/10.1016/j.ijbiomac.2024.133837>.

#### References

- [1] J. Zhong, et al., Reversibly immortalized keratinocytes (iKera) facilitate re-epithelization and skin wound healing: potential applications in cell-based skin tissue engineering, *Bioact. Mater.* 9 (2022) 523–540.
- [2] R.F. Pereira, et al., Advances in bioprinted cell-laden hydrogels for skin tissue engineering, *Bio-manuf. Rev.* 2 (2017) 1–26.
- [3] R. Hao, et al., Rational design and preparation of functional hydrogels for skin wound healing, *Front. Chem.* 9 (2022) 839055.
- [4] S.A. Guo, L.A. DiPietro, Factors affecting wound healing, *J. Dent. Res.* 89 (3) (2010) 219–229.
- [5] V. Jones, J.E. Grey, K.G. Harding, Wound healing: a cellular perspective, *Bmj* 332 (7544) (2006) 777–780.
- [6] D. Kong, et al., Adhesion loss mechanism based on carboxymethyl cellulose-filled hydrocolloid dressings in physiological wounds environment, *Carbohydr. Polym.* 235 (2020) 115953.
- [7] H.S. Kim, et al., Advanced drug delivery systems and artificial skin grafts for skin wound healing, *Adv. Drug Deliv. Rev.* 146 (2019) 209–239.
- [8] Y. Zhao, et al., Preparation of nanofibers with renewable polymers and their application in wound dressing, *Int. J. Polym. Sci.* 2016 (2016).
- [9] H. Choudhury, et al., Silver nanoparticles: advanced and promising technology in diabetic wound therapy, *Mater. Sci. Eng. C* 112 (2020) 110925.
- [10] Q. Zhang, et al., Electrospun polymeric micro/nanofibrous scaffolds for long-term drug release and their biomedical applications, *Drug Discov. Today* 22 (9) (2017) 1351–1366.
- [11] A. Varesano, R.A. Carletto, G. Mazzuchetti, Experimental investigations on the multi-jet electrospinning process, *J. Mater. Process. Technol.* 209 (11) (2009) 5178–5185.
- [12] V.P. Nirwan, et al., Advances in electrospun hybrid nanofibers for biomedical applications, *Nanomaterials* 12 (11) (2022) 1829.
- [13] K.A. Rieger, N.P. Birch, J.D. Schiffman, Designing electrospun nanofiber mats to promote wound healing—a review, *J. Mater. Chem. B* 1 (36) (2013) 4531–4541.
- [14] X. Hu, et al., Electrospinning of polymeric nanofibers for drug delivery applications, *J. Control. Release* 185 (2014) 12–21.
- [15] C.T. Lim, Nanofiber technology: current status and emerging developments, *Prog. Polym. Sci.* 70 (2017) 1–17.
- [16] M.Q. Khan, et al., Fabrication of antibacterial electrospun cellulose acetate/silver-sulfadiazine nanofibers composites for wound dressings applications, *Polym. Test.* 74 (2019) 39–44.
- [17] G. Dabiri, E. Damstetter, T. Phillips, Choosing a wound dressing based on common wound characteristics, *Adv. Wound Care* 5 (1) (2016) 32–41.
- [18] Gorain, B. and S.P. Sisinthy, Delivery of therapeutics from layer-by-layer electrospun nanofiber matrix for wound healing: An update.
- [19] S. Tort, F. Acartürk, A. Beşikci, Evaluation of three-layered doxycycline-collagen loaded nanofiber wound dressing, *Int. J. Pharm.* 529 (1–2) (2017) 642–653.
- [20] V. Natarajan, et al., Preparation and properties of tannic acid cross-linked collagen scaffold and its application in wound healing, *J. Biomed Mater Res B Appl Biomater* 101 (4) (2013) 560–567.
- [21] C. Helary, et al., Evaluation of dense collagen matrices as medicated wound dressing for the treatment of cutaneous chronic wounds, *Biomater. Sci.* 3 (2) (2015) 373–382.
- [22] E.A. Kamoun, E.-R.S. Kenawy, X. Chen, A review on polymeric hydrogel membranes for wound dressing applications: PVA-based hydrogel dressings, *J. Adv. Res.* 8 (3) (2017) 217–233.
- [23] Q. Chen, K. Zhou, Acetic acid use in chronic wound healing: a multiple case series, *J. Wound Ostomy Cont. Nurs.* 49 (3) (2022) 286–289.
- [24] X. Liu, et al., Antimicrobial electrospun nanofibers of cellulose acetate and polyester urethane composite for wound dressing, *J. Biomed Mater Res B Appl Biomater* 100 (6) (2012) 1556–1565.
- [25] S. Fahimrad, M. Ghorbanpour, Omics approaches in developing abiotic stress tolerance in rice (*Oryza sativa* L.), in: *Advances in Rice Research for Abiotic Stress Tolerance*, Elsevier, 2019, pp. 767–779.
- [26] D.D. Do Pham, et al., Novel lipophosphonoxin-loaded polycaprolactone electrospun nanofiber dressing reduces *Staphylococcus aureus* induced wound infection in mice, *Sci. Rep.* 11 (1) (2021) 17688.
- [27] J. Balucho, D.M. Narváez, J.L. Castro-Mayorga, Antimicrobial and biocompatible polycaprolactone and copper oxide nanoparticle wound dressings against methicillin-resistant *Staphylococcus aureus*, *Nanomaterials* 10 (9) (2020) 1692.
- [28] A. Asiri, et al., Epidermal and fibroblast growth factors incorporated polyvinyl alcohol electrospun nanofibers as biological dressing scaffold, *Sci. Rep.* 11 (1) (2021) 5634.
- [29] D. Nataraj, R. Reddy, N. Reddy, Crosslinking electrospun poly (vinyl) alcohol fibers with citric acid to impart aqueous stability for medical applications, *Eur. Polym. J.* 124 (2020) 109484.
- [30] K.A.G. Katsogiannis, G.T. Vladislavjević, S. Georgiadou, Porous electrospun polycaprolactone (PCL) fibres by phase separation, *Eur. Polym. J.* 69 (2015) 284–295.

- [31] G. Pandey, et al., Multilayered nanofibrous scaffold of Polyvinyl alcohol/gelatin/poly (lactic-co-glycolic acid) enriched with hemostatic/antibacterial agents for rapid acute hemostatic wound healing, *Int. J. Pharm.* 638 (2023) 122918.
- [32] W. Lin, et al., Near-infrared light-responsive nanofibrous membranes for treatment of bacterial wound infections, *ACS Appl. Nano Mater.* 6 (21) (2023) 20298–20309.
- [33] S. Nangare, et al., Silk industry waste protein: isolation, purification and fabrication of electrospun silk protein nanofibers as a possible nanocarrier for floating drug delivery, *Nanotechnology* 32 (3) (2020) 035101.
- [34] J. Hankiewicz, E. Swierczek, Lysozyme in human body fluids, *Clin. Chim. Acta* 57 (3) (1974) 205–209.
- [35] V.S. Waghmare, et al., Starch based nanofibrous scaffolds for wound healing applications, *Bioact. Mater.* 3 (3) (2018) 255–266.
- [36] P. Mistry, et al., Fabrication and characterization of starch-TPU based nanofibers for wound healing applications, *Mater. Sci. Eng. C* 119 (2021) 111316.
- [37] P. Wadke, et al., Silver-embedded starch-based nanofibrous mats for soft tissue engineering, *Surf. Interfaces* 8 (2017) 137–146.
- [38] Y. Feng, et al., Antibiofouling zwitterionic gradational membranes with moisture retention capability and sustained antimicrobial property for chronic wound infection and skin regeneration, *Biomacromolecules* 20 (8) (2019) 3057–3069.
- [39] P. Vashisth, V. Pruthi, Synthesis and characterization of crosslinked gellan/PVA nanofibers for tissue engineering application, *Mater. Sci. Eng. C* 67 (2016) 304–312.
- [40] S. Wu, et al., Improving the water resistance and mechanical properties of feather keratin/polyvinyl alcohol/tris (hydroxymethyl) aminomethane blend films by cross-linking with transglutaminase, *cacl2*, and genipin, *Materials* 11 (11) (2018) 2203.
- [41] M. Samnani, H. Rathod, H. Raval, A novel reverse osmosis membrane modified by polyvinyl alcohol with maleic anhydride crosslinking, *Mater. Res. Express* 5 (3) (2018) 035304.
- [42] R. Rudra, V. Kumar, P.P. Kundu, Acid catalysed cross-linking of poly vinyl alcohol (PVA) by glutaraldehyde: effect of crosslink density on the characteristics of PVA membranes used in single chambered microbial fuel cells, *RSC Adv.* 5 (101) (2015) 83436–83447.
- [43] D. Gyawali, et al., Citric acid-derived in situ crosslinkable biodegradable polymers for cell delivery, *Biomaterials* 31 (34) (2010) 9092–9105.
- [44] A.D. Sekar, et al., Electrospinning of Fe-doped ZnO nanoparticles incorporated polyvinyl alcohol nanofibers for its antibacterial treatment and cytotoxic studies, *Eur. Polym. J.* 118 (2019) 27–35.
- [45] K. Wilpiszewska, A.K. Antosik, M. Zdanowicz, The effect of citric acid on physicochemical properties of hydrophilic carboxymethyl starch-based films, *J. Polym. Environ.* 27 (2019) 1379–1387.
- [46] W. Xiao, et al., Antibacterial hybrid materials fabricated by nanocoating of microfibril bundles of cellulose substance with titania/chitosan/silver-nanoparticle composite films, *J. Mater. Chem. B* 1 (28) (2013) 3477–3485.
- [47] R. Augustine, N. Kalarikkal, S. Thomas, Effect of zinc oxide nanoparticles on the in vitro degradation of electrospun polycaprolactone membranes in simulated body fluid, *Int. J. Polym. Mater. Polym. Biomater.* 65 (1) (2016) 28–37.
- [48] F. Reguieg, et al., Thermal characterization by DSC and TGA analyses of PVA hydrogels with organic and sodium MMT, *Polym. Bull.* 77 (2) (2020) 929–948.
- [49] C.K. Poh, et al., Citric acid functionalized carbon materials for fuel cell applications, *J. Power Sources* 176 (1) (2008) 70–75.
- [50] H.S. Barud, et al., Thermal behavior of cellulose acetate produced from homogeneous acetylation of bacterial cellulose, *Thermochim. Acta* 471 (1–2) (2008) 61–69.
- [51] K. Saeed, et al., Preparation of electrospun nanofibers of carbon nanotube/polycaprolactone nanocomposite, *Polymer* 47 (23) (2006) 8019–8025.
- [52] A.K. Patel, R. Bajpai, J. Keller, On the crystallinity of PVA/palm leaf biocomposite using DSC and XRD techniques, *Microsyst. Technol.* 20 (2014) 41–49.
- [53] J.-Q. Mei, et al., Effects of citric acid esterification on digestibility, structural and physicochemical properties of cassava starch, *Food Chem.* 187 (2015) 378–384.
- [54] J. Prakash, et al., In-vitro evaluation of electrospun cellulose acetate nanofiber containing Graphene oxide/TiO<sub>2</sub>/Curcumin for wound healing application, *Colloids Surf. A Physicochem. Eng. Asp.* 627 (2021) 127166.
- [55] W. Zeng, et al., Electrospun polycaprolactone nanofibrous membranes loaded with baicalin for antibacterial wound dressing, *Sci. Rep.* 12 (1) (2022) 10900.
- [56] G. Chen, T. Ushida, T. Tateishi, Development of biodegradable porous scaffolds for tissue engineering, *Mater. Sci. Eng. C* 17 (1–2) (2001) 63–69.
- [57] H. Liang, et al., Fabrication of tragacanthin gum-carboxymethyl chitosan bio-nanocomposite wound dressing with silver-titanium nanoparticles using freeze-drying method, *Mater. Chem. Phys.* 279 (2022) 125770.
- [58] H.U. Zaman, et al., Physico-mechanical properties of wound dressing material and its biomedical application, *J. Mech. Behav. Biomed. Mater.* 4 (7) (2011) 1369–1375.
- [59] J. Tavakoli, Y. Tang, Honey/PVA hybrid wound dressings with controlled release of antibiotics: structural, physico-mechanical and in-vitro biomedical studies, *Mater. Sci. Eng. C* 77 (2017) 318–325.
- [60] C. Kimna, S. Tamburaci, F. Tihminlioglu, Novel zein-based multilayer wound dressing membranes with controlled release of gentamicin, *J. Biomed Mater Res B Appl Biomater* 107 (6) (2019) 2057–2070.
- [61] R. Xu, et al., Controlled water vapor transmission rate promotes wound-healing via wound re-epithelialization and contraction enhancement, *Sci. Rep.* 6 (1) (2016) 24596.
- [62] S.Z. Razavi, et al., Polycaprolactone/cress seed mucilage based bilayer antibacterial films containing ZnO nanoparticles with superabsorbent property for the treatment of exuding wounds, *Int. J. Biol. Macromol.* 256 (2024) 128090.
- [63] M. Karimi, et al., Fabrication of shapeless scaffolds reinforced with baghdadite-magnetite nanoparticles using a 3D printer and freeze-drying technique, *J. Mater. Res. Technol.* 14 (2021) 3070–3079.
- [64] B. Barua, M.C. Saha, Influence of humidity, temperature, and annealing on microstructure and tensile properties of electrospun polyacrylonitrile nanofibers, *Polym. Eng. Sci.* 58 (6) (2018) 998–1009.
- [65] H. Itoh, et al., Morphology and mechanical properties of PVA nanofibers spun by free surface electrospinning, *Polym. Bull.* 73 (2016) 2761–2777.
- [66] A. Eskandarinia, et al., A propolis enriched polyurethane-hyaluronic acid nanofibrous wound dressing with remarkable antibacterial and wound healing activities, *Int. J. Biol. Macromol.* 149 (2020) 467–476.
- [67] A. Eskandarinia, et al., A novel bilayer wound dressing composed of a dense polyurethane/propolis membrane and a biodegradable polycaprolactone/gelatin nanofibrous scaffold, *Sci. Rep.* 10 (1) (2020) 3063.
- [68] D. Dharavath, R. Maddi, ISO standards of medical devices, *World J. Curr. Med. Pharm. Res.* (2022) 33–39.
- [69] J. O'brien, et al., Investigation of the Alamar Blue (resazurin) fluorescent dye for the assessment of mammalian cell cytotoxicity, *Eur. J. Biochem.* 267 (17) (2000) 5421–5426.
- [70] S.-Y. Ong, et al., Development of a chitosan-based wound dressing with improved hemostatic and antimicrobial properties, *Biomaterials* 29 (32) (2008) 4323–4332.
- [71] S. Dugam, et al., Crystallinity modulated silk fibroin electrospun nanofibers based floating scaffold as a candidate for controlled release of felodipine, *Int. J. Polym. Mater. Polym. Biomater.* 71 (18) (2022) 1393–1406.
- [72] S.H. Lee, B.-H. Jun, Silver nanoparticles: synthesis and application for nanomedicine, *Int. J. Mol. Sci.* 20 (4) (2019) 865.
- [73] M.A. Ansari, et al., Interaction of silver nanoparticles with *Escherichia coli* and their cell envelope biomolecules, *J. Basic Microbiol.* 54 (9) (2014) 905–915.
- [74] R. Chhabra, et al., In vivo studies of 3D starch–gelatin scaffolds for full-thickness wound healing, *ACS Appl. Bio Mater.* 3 (5) (2020) 2920–2929.
- [75] Z. Xie, et al., Dual growth factor releasing multi-functional nanofibers for wound healing, *Acta Biomater.* 9 (12) (2013) 9351–9359.



## Crystallinity modulated silk fibroin electrospun nanofibers based floating scaffold as a candidate for controlled release of felodipine

Shailesh Dugam, Sopan Nangare, Anil Gore, Sarika Wairkar, Pramod Patil, Latika Choudary & Namdeo Jadhav

To cite this article: Shailesh Dugam, Sopan Nangare, Anil Gore, Sarika Wairkar, Pramod Patil, Latika Choudary & Namdeo Jadhav (2022) Crystallinity modulated silk fibroin electrospun nanofibers based floating scaffold as a candidate for controlled release of felodipine, International Journal of Polymeric Materials and Polymeric Biomaterials, 71:18, 1393-1406, DOI: [10.1080/00914037.2021.1981318](https://doi.org/10.1080/00914037.2021.1981318)

To link to this article: <https://doi.org/10.1080/00914037.2021.1981318>



Published online: 03 Oct 2021.



Submit your article to this journal [↗](#)



Article views: 203



View related articles [↗](#)



View Crossmark data [↗](#)




Citing articles: 5 View citing articles [↗](#)





## Crystallinity modulated silk fibroin electrospun nanofibers based floating scaffold as a candidate for controlled release of felodipine

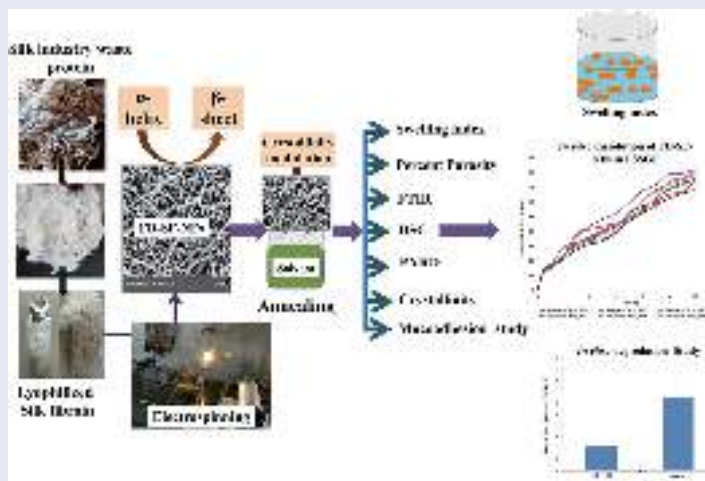
Shailesh Dugam<sup>a</sup>, Sopan Nangare<sup>b\*</sup>, Anil Gore<sup>c</sup>, Sarika Wairkar<sup>d</sup> , Pramod Patil<sup>e</sup>, Latika Choudary<sup>e</sup>, and Namdeo Jadhav<sup>a</sup>

<sup>a</sup>Department of Pharmaceutics, Bharati Vidyapeeth College of Pharmacy, Kolhapur, India; <sup>b</sup>Department of Pharmaceutical Chemistry, H. R. Patel Institute of Pharmaceutical Education and Research, Shirpur, India; <sup>c</sup>Institute of Chemical Science, UKA Tarsadia University, Bardoli 394350, Gujarat, India; <sup>d</sup>Shobhaben Pratapbhai Patel School of Pharmacy & Technology Management, SVKM's NMIMS, Mumbai, India; <sup>e</sup>School of Nanoscience and Technology, Shivaji University, Kolhapur, India

### ABSTRACT

Floating gastro-retentive delivery approach provides a significant pathway for controlled release of drug with increase gastric residence. In this study, we report crystallinity modulated electrospun silk fibroin nanofibers (SF-NFs) floating scaffolds for the controlled release of felodipine (FD). The alteration in the crystallinity behavior due to changes in the structural conformation of SF helps to customize the release kinetics of FD-loaded SF-NFs scaffolds. Additionally, FD-loaded SF scaffolds system having a density less than the acidic gastric fluid explore as a new tactic for floating drug delivery system. The prepared FD-loaded SF nanofibers (FD-loaded SF-NFs) were characterized by spectral, thermal, and diffractometric techniques, scanning electron microscopy, floating profile, *in-vitro* degradation, mucoadhesion, and *in-vitro* dissolution studies, etc. The optimized batch had the least porosity and swelling, was annealed with ethanol and water for crystallinity modulation of SF-NFs to get controlled release of FD. Spectral, thermal, and diffractometric analyses could unveil the molecular dispersion of FD, coupled with amorphous form stabilization in NF. Excellent floating profile and satisfactory mucoadhesion of FD-SF-NFs also endorsed the formation of a novel floating drug delivery system. Temporal control over FD release was elucidated by *in-vitro* dissolution, demonstrating controlled release due to crystallinity modulation of SF-NFs. In conclusion, crystallinity-modulated electrospun NFs fabricated from SF waste could be used as a customizable carrier for drug delivery to the gastric region.

### GRAPHICAL ABSTRACT



Crystallinity modulated silk fibroin electrospun nanofibers based floating scaffold as a candidate for controlled release of felodipine

### ARTICLE HISTORY

Received 15 June 2021  
Accepted 7 September 2021

### KEYWORDS

Silk fibroin; electrospun nanofibers; crystallinity modulation; felodipine; floating drug delivery; controlled release



## 1. Introduction

Gastroretentive drug delivery systems have received significant interest in the past few decades owing to their regio-selective and targeted drug delivery<sup>[1]</sup>. Principally, it helps to deliver a drug to the upper part of the gastrointestinal tract (GIT) for the local treatment of hyperacidity, ulcers, *Helicobacter pylori* infection. Additionally, it offers improved bioavailability of drugs having an absorption window from the stomach<sup>[1,2]</sup>. To date, numerous approaches have been adopted for the design of gastroretentive drug delivery systems<sup>[2]</sup>. Mainly, high density (sinking), and hydrodynamically balanced/swellable/low-density systems (floating); bioadhesive/mucoadhesive and magnetic systems; altered shape/expandable systems, etc. are extensively researched by scientific fraternities<sup>[3,4]</sup>. It has been reported that the novel gastroretentive drug delivery systems viz. tablets, granules, powders, capsules, hollow microspheres, laminated films, etc. have been tried in the literature, and even a few are at the marketplace<sup>[5,6]</sup>. Amongst those, floating drug delivery system holds a major share of clinically used formulations. Drugs like ciprofloxacin, metformin hydrochloride, tramadol, etc. count clinically as floating drug delivery systems<sup>[7]</sup>. Floating drug delivery systems can be developed using effervescent material wherein, carbon dioxide gas is generated which get entrapped in swollen hydrocolloids providing buoyancy to the dosage form, whilst non-effervescent system includes the use swelling system and low-density material<sup>[8]</sup>. Electrospun nanofibers (NFs) with homogenous or complex structures offer low density, high pore volume, high charge to volume ratio, high drug payload, and high surface to volume ratio for the solvation and dissolution process, provide an excellent tool for controlled release of drugs and another functional molecule<sup>[9]</sup>. Several NFs based floating drug delivery systems have been developed to keep NFs in the stomach for a sustained drug release. Darbasizadeh et al. developed tripolyphosphate cross-linked nanofibrous mats based on chitosan which remains floated on gastric fluid for more than 48 h with a sustained release profile at pH 1.2<sup>[10]</sup>. Tort et al. reported for self-inflating effervescence-based electrospun NFs membranes embedding polyethylene oxide/sodium bicarbonate. The prepared NFs when came in contact with gastric fluid resulting in gas bubbles being entrapped within the swollen network of NFs. The system remains floated for more than 72 h with initial burst release and then followed by sustained release pattern<sup>[11]</sup>.

Interestingly, no reports are available on crystallinity modulated floating electrospun NFs for controlled or sustained release of a drug. Hence, we planned to fabricate crystallinity modified electrospun Felodipine (FD) loaded floating NFs using low-density silk-fibroin (SF) polymer. Mainly, SF was a protein waste recycled from reeling houses, processing cocoons of *Bombyx mori*. Concerning the polar and non-polar regions of SF<sup>[12]</sup>, it demonstrates good mucoadhesion properties. Possibly, it may be due to the secondary bond interaction among skin underlining tissue and SF polar functional groups<sup>[13]</sup>. From the perspective of SF chemistry, SF comprising of an amorphous state called silk I due to  $\alpha$ -helices conformation and a crystalline state termed

silk II due to high  $\beta$ -sheets content. The  $\beta$ -sheets conformation of SF plays an imperative role to tune the physicochemical properties of SF like mechanical strength, water-solubility, biodegradability, etc. The transition of SF from  $\alpha$  helix conformation to  $\beta$  sheet conformation can be favored by using alcohols or via water annealing<sup>[14]</sup>. The crystallinity manipulation of SF was used as a processing tactic to tune the biodegradability and thereof to control the release profile of the drug. The *in-vitro* degradation study, executed on SF fibrous scaffolds revealed that SF has shown the slower degradation of scaffolds with higher crystallinity. Thus, crystallinity modulation opportunities of SF enable the control of the degradation of scaffolds manifesting prolonged and controlled delivery of active factors<sup>[15]</sup>. Additionally, the process parameters for FD-loaded SF-NFs could be optimized by a Process Analytical Technology (PAT) tool, aiming fine-tuning of NFs crystallinity, for modeling controlled release profile. In addition, the PAT study confirmed first time, the effect of electrospinning parameters on the crystallinity of SF-NFs. The suitability of FD (calcium channel blocker) was zeroed down from its poor aqueous solubility, absorption window from the stomach, pKa (5.07), log D (3.44), elimination half-life (up to 5–8 h), poor bio-availability, etc.<sup>[16]</sup>. Finally, the FD-loaded SF-NFs were further evaluated for percentage drug content and entrapment efficiency, spectral and thermal characters, scanning electron microscopy, floating profile, porosity, uptake of 0.1 hydrochloric acid (HCl), *in-vitro* degradation, mucoadhesion, and *in-vitro* dissolution.

## 2. Experimental

### 2.1. Materials

FD was availed as a gift sample from Cipla Pvt. Ltd. Mumbai, Maharashtra, (India), and formic acid was purchased from Research Lab. Fine Chem. Industries, Mumbai, Maharashtra (India). Calcium chloride and ethanol were purchased from Molychem Pvt. Ltd. Mumbai, Maharashtra (India). Sodium bicarbonate, hydrochloric acid was purchased from Lobachem Pvt. Ltd. Mumbai, Maharashtra, and (India). Ascorbic acid was purchased from Fine Chemicals Limited, Ahmedabad, Gujrat (India). Potassium dihydrogen phosphate was purchased from Merck Specialties Pvt. Ltd. Mumbai Maharashtra, (India), Silk waste was collected locally from Islampur, Sangli Maharashtra, and (India). Dialysis Membrane-110 was purchased from Himedia Lab. Pvt. Ltd. Mumbai, Maharashtra (India).

### 2.2. Methods

#### 2.2.1. Extraction of silk fibroin (SF)

The extraction of SF was carried out from recycled waste of silk reeling houses (units processing cocoons of *Bombyx mori*). In brief, the collected silk waste was initially immersed in the boiling solution of 0.5% sodium carbonate for 20 min with continuous stirring. Herein, the glue-like sericin was dissolved in the 0.5% sodium carbonate

containing aqueous solution. After that, the remaining whole mass was repeatedly washed with distilled water so that the degummed silk obtained is completely freed from sericin<sup>[7]</sup>. From the same, 10 g of degummed silk was added to a ternary solvent system comprising calcium chloride, ethanol, and water (CWC) in a 1:2:8 molar ratio at 70°C for 6 h, followed by dialysis with cellulose tubular membranes (molecular weight cutoff, 12,000; Sigma) against distilled water for 3 days. Subsequently, SF concentrate obtained was subject to centrifugation at 9000 rpm. The clear solution obtained was a deep freeze at -40°C, for 2 days and then lyophilized (0.013 mbar pressure, -49°C temperature for primary drying and at 10°C for 8 h and was followed by drying at 25°C for 4 h with a gradual increase in temperature at 1°C/min for secondary drying) to get SF powder<sup>[17]</sup>.

### 2.2.2. Electrospinning process

In this study, the polymer concentration was optimized based on initial trials on the electrospinning unit. Then, optimized SF solutions (10% w/v) were prepared by dissolving 1 g of freeze-dried SF in 10 mL of formic acid (98%) with stirring up to 3 h. The resulting solution was electrospun as per process parameters given in Table 1. The process optimization parameters for electrospinning were flow rate (0.5–1 mL/h.), the distance between syringe nozzles to the collector (8–12 cm), voltage (17–23 kV), collector drum speed (400–500 rpm), and spinneret speed (50–100 cycles/min). So as to enunciate the effect of critical process parameters (CPP) on critical quality attributes (CQA) of drug-loaded NFs/scaffolds, one parameter was changed at a time, and the rest were kept constant to get SF-NFs. For the preparation of FD-loaded SF-NFs, 10 mg of the FD has been loaded in 10% w/v SF electrospinning solution with constant stirring at 400 rpm for proper mixing and uniform distribution of the drug in polymeric electrospinning solution. Further, FD-loaded SF-NFs were spun using electrospinning process parameters given in Table 1. The effect of electrospinning process parameters on the crystallinity of FD-

loaded SF-NFs was investigated by calculating the degree of crystallinity of prepared scaffolds (FD1–FD6) depicted in Table 2. Out of six batches of FD-loaded NFs (FD1–FD6), the optimized batch FD4 demonstrating desired performance in terms of unbeaded NFs with the least porosity and swelling was annealed with two solvents namely ethanol (FDE) and water (FDW) for achieving desired release behavior. The annealing treatment was optimized in a vacuum oven at 40°C/40–60% relative humidity, at different time intervals (2, 4, 6, 8 h).

### 2.2.3. Application of process analytical technology (PAT)

Application of PAT was carried out to design NFs with a tailor-made FD release profile. From the previously mentioned process parameters, the critical process parameters (CPP) were identified during the electrospinning process and evaluation of NFs. More importantly, the effect of CPP was investigated on critical quality attributes (CQA) and quality target product profile (QTPP).

## 3. Spectral, thermal, diffractographic, morphological, and physicochemical characterization

### 3.1. Fourier transform infrared spectrophotometry (FTIR)

The ATR-FTIR spectra of dry powder of SF, FD, SF-NFs, SF and FD physical mixture, FD loaded SF-NFs (FD1–FD6), FDE and FDW were recorded using an Infrared spectrophotometer (Jasco-V-530 model, Japan). Briefly, two mg of sample was taken and thoroughly ground with KBr in a mortar using a pestle, for uniform mixing. Subsequently, the homogeneous powder obtained was placed in a sample holder, and recorded the spectra were over the wavenumber 400–4,000 cm<sup>-1</sup> for analysis<sup>[18]</sup>.

**Table 1.** Formulation and process parameters for electrospinning of FD-SF-NFs.

Batchcode	Polymer concentration (%) w/v	FD (mg)	Voltage (kV)	Spinneret speed	Flow rate (mL/min)	Distance between collector to needle tip (cm)	Needle diameter (mm)
FD1	10	10	22	30	0.5	10	0.7
FD2	10	10	22	50	0.5	10	0.7
FD3	10	10	22	70	0.5	10	0.7
FD4	10	10	22	50	0.4	10	0.7
FD5	10	10	22	50	0.5	08	0.7
FD6	10	10	22	50	0.5	12	0.7

**Table 2.** Principle wave number values from ATR-FTIR spectra, and degree of crystallinity for SF.

Type of peak	Wavenumber (cm <sup>-1</sup> ) and crystallinity							
	FD1	FD2	FD3	FD4	FD5	FD6	FDW	FDE
N-H Stretching	3274.52	3277.30	3295.25	3289.10	3284.79	3294.27	3293.59	3286.41
C-O Stretching	1651.78	1643.80	1631.77	1651.45	1651.93	1643.78	1632.12	1621.76
N-H Deformation	1525.26	1514.06	1514.40	1525.12	1528.59	1518.66	1515.20	1515.10
N-H Bending	1238.94	1232.06	1232.49	1232.38	1239.26	1238.01	1230.89	1231.50
Degree of crystallinity (tangent baseline method)	0.875	1.10	1.47	1.25	1.21	1.25	1.81	1.53
Degree of crystallinity (deconvolution of amide II peak)	1.02	1.15	1.46	1.04	1.29	1.26	1.90	1.69

### 3.2. Calculation of the degree of crystallinity of SF-NFs using Fourier transform infrared spectrophotometry

The same recorded FTIR spectra were used for the calculation of the degree of crystallinity of SF-NFs and FD-loaded SF-NFs by the tangent baseline method<sup>[14,19]</sup>. The intensity of two successive peaks for amide I and amide II of SF were considered for crystallinity calculations. The tangent was drawn to the successive peak of amide I and amide II. Then, the perpendicular line was drawn from the tip of a peak to the midpoint of the tangent and the intensity of peaks was measured in terms of height (cm). The degree of crystallinity was calculated according to the following formula (Eq. 1):

$$\text{Degree of crystallinity} = \frac{a}{b} \quad (1)$$

Where,  $a/b$ —the ratio of the peak intensity of amide I to the peak of amide II in  $\text{cm}^{-1}$ . Secondly, the degree of crystallinity was calculated by deconvolution of amide II, wherein, the intensity of amide II peak of standard (neat, without drug SF-NFs) and the intensity of amide II peak of the sample (FD-SF-NFs) were measured for calculation of the degree of crystallinity. (The intensity ratio of the amide II peak at  $1,510 \text{ cm}^{-1}$  for a sample and  $1,528 \text{ cm}^{-1}$  for the standard was used).

### 3.3. Differential Scanning calorimetry (DSC)

Thermal behavior of dry powder of SF, FD, SF-NFs, SF, and FD/SF physical mixture, FD loaded SF-NFs, FDE, FDW was analyzed by DSC (Shimadzu, TA instruments, model SDT 2960, USA) equipped with intra cooler and refrigerated cooling system<sup>[20]</sup>. In DSC analysis, we obtained DSC curves at a scanning rate of  $10^\circ\text{C}/\text{min}$  conducted over a temperature range of  $25\text{--}370^\circ\text{C}$  followed by generalized cooling. In this regard, an empty aluminum pan was used as a standard reference, and results were obtained in triplicates for each sample followed by a single cycle.

### 3.4. Powder X-ray diffraction studies (PXRD)

The PXRD patterns of dry powder of SF, FD, SF, and FD physical mixture, SF-NFs, FD loaded SF-NFs (FD4), FDE, and FDW were recorded at room temperature by X-ray diffractometer (Philips analytical XRD, PW 3710, Switzerland) using  $\text{CuK}\alpha$  radiation ( $1.54 \text{ \AA}$ ), at  $40 \text{ kV}$ ,  $40 \text{ mA}$  and passing through a nickel filter. The diffractometer was equipped with a  $2\theta$  compensating slit and calibration for the accuracy to the position of peaks was done with pellets of silicon. Then the samples were allowed to X-ray powder diffraction analysis in continuous mode with a step size of  $0.01^\circ$  and a step time of  $1 \text{ s}$  over an angular range of  $3\text{--}40^\circ 2\theta$ . The sample holder has rotated in a parallel plane with a rotation speed of  $30 \text{ rpm}$  during analysis<sup>[7]</sup>.

### 3.5. Scanning electron microscopy (SEM)

The surface morphology of pristine SF-NFs and FD-loaded SF-NFs (FD-FD6) was studied by SEM (LEO 435 VP,

Eindhoven, and The Netherlands). For the preparation of the sample, a double-adhesive tape was stuck to an aluminum stub and then further removed to achieve an adhesive-coated aluminum stub. Then, 1–2 drops of FD-SF-NFs dispersion were applied on the stub and allowed to dry. The stubs were then coated with gold to a thickness of  $\sim 300 \text{ \AA}$  under a high vacuum evaporator in presence of an argon atmosphere. Then the coated stub was subject to an accelerating voltage of  $15 \text{ kV}$  for the  $90 \text{ s}$  under  $0.1 \text{ torr}$  pressure of argon. Images for different batches for FD-loaded SF-NFs were acquired at different magnifications using an SEM<sup>[7]</sup>. Additionally, the average NFs diameter size was determined from SEM micrographs considering about 100 different NFs using Image J (NIH) software. Even, SEM images of exhausted sheets of FD-loaded SF-NFs (collected and dried after completion of *in vitro* dissolution study), were taken as aforesaid.

### 3.6. Percentage entrapment efficiency and percentage drug content

The percentage entrapment efficiency (%EE) was carried out by taking  $30 \text{ mg}$  of FD-SF-NFs (FD1–FD6) followed by dispersing in  $50 \text{ mL}$  of methanol and magnetically stirring for about two hours, and sonication for  $15 \text{ min}$ . The resulting dispersion was centrifuged (Remi, Mumbai, India) at  $2,000 \text{ rpm}$  for  $10 \text{ min}$ , and the supernatant was filtered using Whatman filter paper no. 45. The filtrate was assayed for FD content by a UV-visible spectrophotometer at  $\lambda_{\text{max}}$   $360 \text{ nm}$ <sup>[7]</sup>. The percent entrapment efficiency was performed in triplicate and calculated using Eq. 2.

$$\%EE = \frac{\text{Theoretical drug content} - \text{Practical drug content}}{\text{Theoretical drug content}} \times 100 \quad (2)$$

For determination of percentage drug content,  $30 \text{ mg}$  of FD-loaded SF-NFs (FD1–FD6) equivalent to  $10 \text{ mg}$  of FD were taken and filled in capsule ( $n=20$ ) and placed in separate volumetric flasks containing  $100 \text{ mL}$  of  $\text{pH } 1.2 \text{ HCl}$  buffer and stirred continuously up to  $24 \text{ h}$ . Subsequently, the solutions were filtered, diluted suitably, and analyzed at  $360 \text{ nm}$  using a UV-visible spectrophotometer (Shimadzu UV 1800, Japan). The drug content in FD-loaded SF-NFs was calculated using slope and  $y$ -intercept values of the calibration curve for FD, in triplicate<sup>[7]</sup>.

### 3.7. Porosity, 0.1 N hydrochloric acid (HCl) uptake kinetics, and swelling study

The porosity of SF, SF-NFs, and FD-loaded SF-NFs was measured by the liquid displacement method (ethanol as a displacement media). Ethanol penetrates through the aforesaid samples without swelling them. In a graduated cylinder SF, SF-NFs, and FD-loaded SF-NFs (FD1–FD6) were immersed separately in a known volume of ethanol ( $v_1$ ) for  $5 \text{ min}$ . Subsequently, the total volume of ethanol and

ethanol-impregnated SF, SF-NFs, and FD-loaded SF-NFs (FD1-FD6) were noted as volume ( $v_2$ ). The ethanol-impregnated SF, SF-NFs, and FD-loaded SF-NFs were removed from the cylinder and the remaining volume of ethanol was recorded ( $v_3$ )<sup>[7]</sup>. The porosity was calculated using the following equation,

$$\text{Porosity (\%)} = \frac{V_1 - V_3}{V_2 - V_3} \times 100 \quad (3)$$

For 0.1 N HCl uptake kinetics and swelling study, the 20 mm × 80 mm pre-weighed FD loaded SF-NFs (FD1-FD6) NFs sheets and dry powder of SF were immersed in 0.1 N HCl for 1, 2, 3, 4, 5, 6, and 24 h respectively. An excess amount of 0.1 N HCl was removed and the weight of wet FD loaded SF-NFs and wet powder of SF was recorded as ( $W_s$ ) and. All the samples were dried overnight at 60 °C and the weight of dry FD loaded SF-NFs and SF was recorded as  $W_d$ <sup>[7]</sup>. Further, calculated the 0.1 N HCl uptake and swelling ratio of FD loaded SF-NFs (FD1-FD6) and dry powder of SF separately for samples using formulae,

$$0.1\text{NHCl uptake (\%)} = \frac{W_s - W_d}{W_s} \times 100 \quad (4)$$

$$\text{Swelling ratio} = \frac{W_s - W_d}{W_d} \quad (5)$$

### 3.8. In-vitro degradation study of felodipine loaded silk fibroin (FD-loaded SF-NFs)

Accurately weighed 30 mg of FD-loaded SF-NFs equivalent to 10 mg of FD were incubated in 10 mL of fasted state simulated gastric fluid (FSSGF) at 37°C for 24 h. As a control group, FD-loaded SF-NFs were incubated in 0.1 N HCl (pH 1.2), without enzymes, for 24 h. The degradation products and the remaining NFs were collected for analysis. The quantitative changes in weight were expressed as the percentage of the NFs weight remaining compared to its initial weight<sup>[21]</sup>.

### 3.9. Floating profile studies

#### 3.9.1. Floating lag time

Accurately weighed 30 mg of FD loaded SF-NFs equivalent to 10 mg of FD (FD4) were taken and kept in a 250 mL capacity beaker containing 150 mL of simulated gastric fluid having pH 1.2. The time required for FD-loaded SF-NFs to come on the surface of simulated gastric fluid and the floated remains were recorded as floating lag time recorded<sup>[7]</sup>.

#### 3.9.2. Percent buoyancy of felodipine loaded silk fibroin (FD-loaded SF-NFs)

Accurately weighed 30 mg of FD-loaded SF-NFs equivalent to 10 mg of FD (FD4) were kept in a 250 mL capacity beaker containing 150 mL of simulated gastric fluid having pH 1.2. In this study, the amount of FD-loaded SF-NFs floated concerning the total amount NFs added into the beaker was

taken as percent buoyancy. Percent buoyancy was calculated using the following formula (Eq. 6).

$$\text{Percent buoyancy} = \frac{\text{Total amount of nanofibers floated (mg)}}{\text{Total amount of nanofibers added (mg)}} \times 100 \quad (6)$$

#### 3.9.3. Total floating time

For the controlled and sustained release of the drug, the floating system should exhibit maximum total floating time. This study was performed by using the USP paddle apparatus (type II) at 37 ± 0.5°C, wherein, accurately weighted 30 mg FD loaded SF-NFs equivalent to 10 mg of FD kept in 900 mL of 0.1 N HCl (pH 1.2) and stirred at 50 rpm<sup>[7]</sup>. In this, the time up to which the NFs remain float on the surface of the 0.1 N HCl medium was measured as total floating time.

#### 3.10. Ex-vivo mucoadhesion test

The Mucoadhesion test demonstrates the force of attraction and residence time of NFs on the mucosal surface. For the determination of mucoadhesive strength of FD-loaded SF-NFs, goat stomach mucosa was used. The underlying mucosa of the goat stomach was separated using a surgical blade and then cut into fixed dimensions 2 cm (w) x 4 cm (L). Later, washings to goat mucosa were given using gastric fluid (0.1 N HCl). For the actual test, accurately weighed 30 mg of FD loaded SF-NFs equivalent to 10 mg of FD sheet was kept on mucosa for 5 min for preloading, to enable adhesion bonding between sheet and mucosa. The mucosa was fixed by using thread after the successful preloading of FD-loaded SF-NFs. Afterward; water was dropped on the FD-loaded SF-NFs sheet at a constant rate (100 drops per min). When the sheet gets detached from the mucosal layer, the addition of water droplets was stopped and recorded as a mucoadhesion time. The amount of water required to detach the sheet from the mucosal layer was noted as mucoadhesive strength (g) of FD-loaded SF-NFs. A force of adhesion was calculated from mucoadhesion strength as follows<sup>[7]</sup>.

$$\text{Force of adhesion (N)} = \frac{\text{Mucoadhesive Strength} \times 9.81}{1,000} \quad (7)$$

#### 3.11. In-vitro dissolution studies

Hard gelatin capsules filled with FD-loaded SF-NFs (equivalent to 10 mg FD) were placed in the USP apparatus-I (basket method) containing 900 mL of 0.1 N HCl and FSSGF separately. Processing conditions including temperature (37 ± 0.5°C) and basket rotation speed (50 rpm) were maintained throughout the dissolution study. At each sampling time point, 5 mL of dissolution media was withdrawn and the same amount of buffer solution was added as a replacement, to maintain sink condition. Sample withdrawn were filtered through Whatman filter paper (0.22 µm, Whatman Inc., USA) and further diluted to 10 mL using a buffer solution. The prepared sample was analyzed by a UV-visible



spectrophotometer at 360 nm and the percent cumulative drug release was calculated. The dissolution profile FD loaded SF-NFs was analyzed by PCP-Disso-V3.08 software. In which Zero-order, First-order, Higuchi, Hixson-Crowell, Korsmeyer, and Peppas equation were selected as a model-dependent approach to characterize the dissolution profile<sup>[22,23]</sup>. For the study of release mechanism, mainly three important parameters were taken into consideration, n-release exponent, k-release rate constant,  $r^2$ -correlation coefficient<sup>[7,24]</sup>. The practically observed value for the release of FD from FD-SF-NFs filled capsule was tabulated in Table 3. By comparing the  $R^2$  values of the kinetic model, the best-fit model was selected. In addition, the dissolution profile for each batch of FD loaded SF-NFs (FD1–FD6) and FDE, FDW was performed similarly and the effect of electrospinning parameters, solvent vapor annealing treatment, and thereof crystallinity of NFs on the release profile of the drug was compared and analyzed.

4. Result and discussion

4.1. Extraction of silk fibroin (SF)

Collected silk waste comprised of small pieces of cocoons and waste silk fibers (short and tiny). Relatively, fibers were more in silk waste, thus, after the degumming process, they could yield SF up to 80–84%. The degummed SF dissolved in a ternary solvent system, dialyzed, and freeze-dried to produced lyophilized SF powder from SF solution. The UV-visible spectra, melting point, and physicochemical tests confirmed the extracted SF. The melting point of SF was found to be 269–285°C. whereas; freeze-dried SF was showed a strong UV absorption band ( $\lambda_{max}$ ) at around 271 nm wavelength. Based on the above-mentioned preliminary studies, the successful extraction of SF protein was confirmed.

4.2. Optimization of electrospun silk fibroin (SF-NFs)

The SF-NFs with electrospinning parameters (SF concentration: 10%w/v, flow rate: 0.5 mL/h, voltage: 22 kV and spinneret speed: 50 cycles/min, collector drum speed: 500 rpm, the distance between collector drum and needle of tip: 10 cm) gives uniform, fine and smooth fibers with no formation of beads witnessed by SEM images (Figure 1a). Hence, these parameters were considered as optimized parameters for the preparation of SF-NFs.

4.3. Application of process analytical technology (PAT)

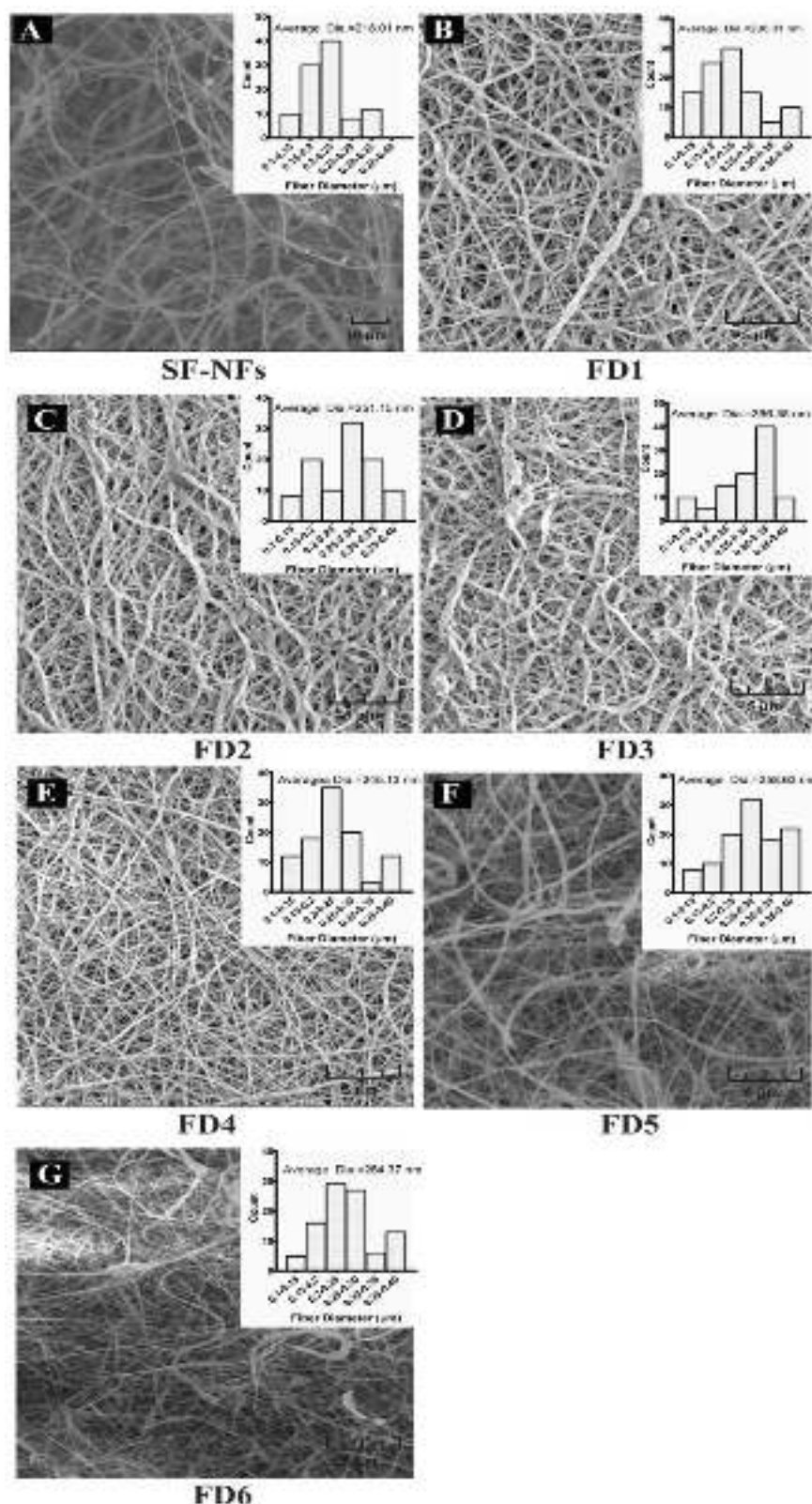
Application of PAT tool is an established tool to integrate the formulation design and further control the process performance of a product throughout its life cycle. Based on the literature, initial trials, and optimization process, it was revealed that the process of FD-loaded SF-NFs was predominantly dependent on CPP like SF concentration, flow rate, spinneret speed, and voltage applied. Annealing treatment to FD-loaded SF-NFs was also treated as a CPP. The careful optimization of CQA for FD loaded SF-NFs done

Table 3. In-vitro drug release kinetic models and regression output.

Batch code	Dissolution medium	Percent drug released* (24 h)	Release exponent (n)	Drug transport mechanism	Release constant (k)	Regression ( $r^2$ )	Best fit release model
FD-SF-NFs (FD4)	0.1N HCl	73.36 ± 0.68	0.5582	Anomalous transport	13.52	0.9733	Zero-order
FDE	0.1N HCl	58.65 ± 0.85	0.5822	Anomalous transport	9.97	0.9786	Zero-order
FDW	0.1N HCl	60.23 ± 0.27	0.6650	Anomalous transport	8.71	0.9701	Zero-order
FD-SF-NFs (FD4)	FSSGF	82.54 ± 0.98	0.9447	Anomalous transport	9.33	0.9972	Zero-order
FDE	FSSGF	68.22 ± 1.39	0.9803	Anomalous transport	7.32	0.9967	Zero-order
FDW	FSSGF	75.69 ± 1.23	1.033	Anomalous transport	8.85	0.9994	Zero-order

\*Mean ± SD (n = 3).





**Figure 1.** SEM images of SF-NFs (a), FD1 (b), FD2 (c), FD3 (d), FD4 (e), FD5 (f), FD5 (g), FD6 (h).

concerning drug loading, percentage drug content and percentage entrapment efficiency, floating characters, percentage crystallinity, appearance, could generate desired NFs. Finally, control over CPP and CQA could generate FD-loaded SF-NFs with essential QTPP (unbeaded NFs morphology, FD strength, and controlled release profile).

#### 4.4. Fourier transform infrared spectrophotometry

The ATR-FTIR spectra of SF showed (Figure 2a) the characteristic vibration bands around  $1651.78\text{ cm}^{-1}$  assigned to amide I and at  $1525.26\text{ cm}^{-1}$  for amide II<sup>[25]</sup>. An ATR-FTIR spectrum of FD shows characteristic peaks at  $3368.389\text{ cm}^{-1}$

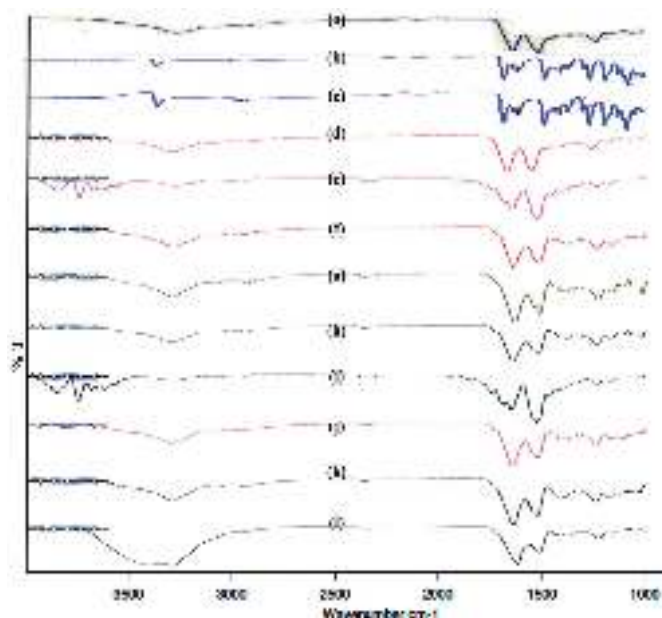


**Figure 2.** FTIR spectra of SF (a), FD (b), physical mixture of SF and FD (c), plane SF (d), FD-SF-NFs (FD1) (e), FD2 (f), FD3 (g), FD4 (h), FD5 (i), FD6 (j), and FD-SF-NFs annealed with ethanol (k), and water (l).

(N-H stretching aliphatic),  $2950.484\text{ cm}^{-1}$  (Aromatic C-H stretching aromatic),  $2677.031\text{ cm}^{-1}$  (C-H stretching),  $1688.965\text{ cm}^{-1}$  (C=O stretching),  $1619.95\text{ cm}^{-1}$  (C=C ring substituent),  $1095.663\text{ cm}^{-1}$  (C-O-C Stretching),  $860.956\text{ cm}^{-1}$  (substituted benzene ring) (Figure 2b). The IR spectrum of the physical mixture indicated principal peaks belonging to amide I at  $1637.52\text{ cm}^{-1}$  and for amide II at  $1525.45\text{ cm}^{-1}$ . It was enunciated from the spectra of FD and SF physical mixture that, the absorption peak of amide I and II are nearly the same as that of SF, confirming no significant interaction between FD and SF (Figure 2c). Characteristic vibration bands of SF-NFs observed at  $1635.908\text{ cm}^{-1}$  were assigned to amide I, whilst amide II was noted at  $1510.45\text{ cm}^{-1}$ . As the spinneret speed increases the principle wave number of amide I and amide II shifted (Figure 2d). As learned from the IR spectrum, FD1 shows the principle wave number for amide I at  $1651.78\text{ cm}^{-1}$  and for amide II at  $1525.26\text{ cm}^{-1}$  (Figure 2e). For FD2 (Figure 2f),  $1643.80\text{ cm}^{-1}$  (amide I),  $1514.06\text{ cm}^{-1}$  (amide II), and for FD3 (Figure 2g),  $1631.77\text{ cm}^{-1}$  (amide I),  $1514.40\text{ cm}^{-1}$  (amide II) were visible. With a decrease in flow rate, the principle wave number for amide I and amide II bands were shifted to  $1651.96\text{ cm}^{-1}$ ,  $1525.12\text{ cm}^{-1}$  respectively as shown in the IR spectrum of the FD4 batch (Figure 2h). The batch FD5 (Figure 2i) and FD6 (Figure 2j) showed vibration bands for amide I and amide II at  $1651.93\text{ cm}^{-1}$ ,  $1528.59\text{ cm}^{-1}$ , and  $1643.78\text{ cm}^{-1}$ ,  $1518.66\text{ cm}^{-1}$  respectively, unveiling slight shifting of the principle wave number of amide I and amide II with a change in distance between drum and collector syringe. Annealing of FD-SF-NFs with ethanol (Figure 2k), exhibited IR vibration bands at  $1632.63\text{ cm}^{-1}$  (amide I),  $1515.20\text{ cm}^{-1}$  (amide II). Whereas, water vapor annealing could show IR peaks (Figure 2l) at  $1621.76\text{ cm}^{-1}$  (amide I) and  $1515.10\text{ cm}^{-1}$  (amide II)<sup>[26]</sup>.

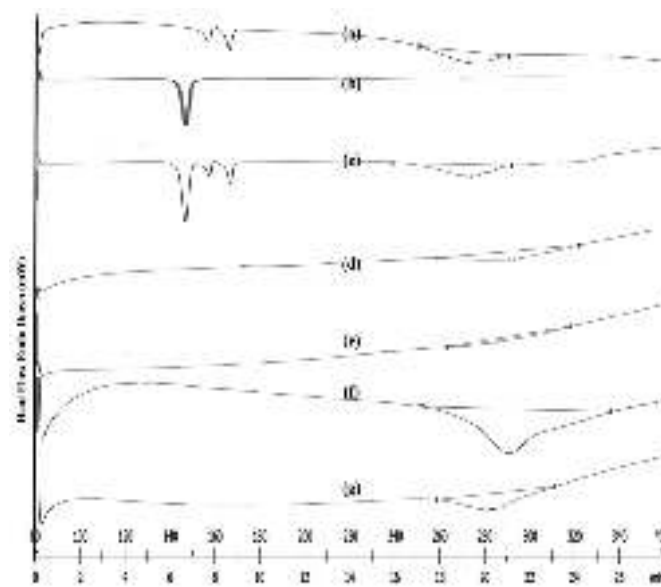


**Figure 3.** Thermograms of dry SF (a), FD (b), physical mixture of SF and FD (c), plane SF-NFs (d), FD loaded SF NFs/FD4 (e) FD loaded SF NFs annealed with ethanol (f), water (g).

#### 4.5. Effect of electrospinning parameters and vapor annealing treatment on the crystallinity of nanofibers

From the observed values of wavenumbers and calculation of the degree of crystallinity for FD-SF-NFs, it was revealed that changes in electrospinning parameters modify the crystallinity to a significant extent. Annealing treatment of solvents demonstrated a profound effect on the crystallinity of NFs. Divulgence of the effect of spinneret speed on an increase in the crystallinity of NFs was evidenced. The decrease in the crystallinity of NFs with a reduction in flow rate was also divulged. Distance between the collector drum and syringe demonstrated no significant effect on the crystallinity of NFs. Post annealing, the crystallinity of NFs was increased due to the transformation of random coil conformation to  $\beta$  sheet conformations, as confirmed from the wavenumbers, corresponding to the characteristic vibration bands of SF (Table 2)<sup>[25,27]</sup>.

#### 4.6. Differential scanning calorimetry (DSC)

In this section, the DSC thermogram of the dry powder of SF (Figure 3a) showed a broad endothermic peak at  $291.64^\circ\text{C}$  ( $\Delta H = -69.51\text{ J/g}$ ) corresponding to its melting point<sup>[7]</sup>. The thermogram of neat FD (Figure 3b) exhibited a sharp melting endotherm at  $146.96^\circ\text{C}$  ( $\Delta H = -70.41\text{ J/g}$ )<sup>[28]</sup>. As anticipated, the physical mixture (SF and FD) showed a sharp melting endotherm of FD at  $146.96^\circ\text{C}$  and that of SF at  $272.36^\circ\text{C}$  (broad), implying no significant interactions and solid-state compatibility (Figure 3c). Compared to SF, little change in enthalpy was observed in the case of a thermogram of SF-NFs (Figure 3d), which demonstrated a broad melting endothermic transition at  $292.03^\circ\text{C}$  ( $\Delta H = -73.76\text{ J/g}$ ). The thermogram of FD-SF-NFs (FD4, Figure 3e) did not show any deep peak corresponding to the melting point of

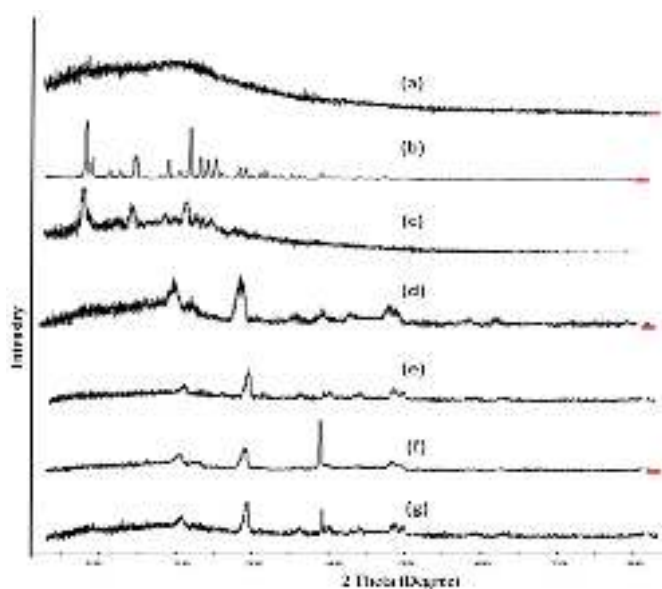


**Figure 4.** Diffractograms of dry powder of SF (a), FD (b), physical mixture of SF and FD (c), plane SF NF (d), FD loaded SF-NFs/FD4 (e), FD loaded SF NFs annealed with ethanol (f) and water (g).

FD divulging its amorphous/molecular level dispersion in fibroin matrix, whilst, broad endothermic peak at  $283.34^{\circ}\text{C}$  ( $\Delta H = -10.90\text{ J/g}$ ) was indicative of reduced crystallinity of SF in FD-SF-NFs, compared to SF-NFs. The thermogram of FDE (Figure 3f) and FDW (Figure 3g) showed broad and high-intensity endothermic transitions at  $289.73^{\circ}\text{C}$  ( $\Delta H = -16.71\text{ J/g}$ ) and  $282.71^{\circ}\text{C}$  ( $\Delta H = -12.24\text{ J/g}$ ) respectively, divulging change from random to  $\beta$  sheet conformation of SF after the annealing treatment (Figure 3). Especially, the crystallinity of FD-loaded SF-NFs annealed with ethanol outweighed FD-loaded SF-NFs annealed with water, due to better orientation of hydrophobic protein domains inside when hydrophilic domains are exposed outside for interaction with water vapors<sup>[29]</sup>.

#### 4.7. Powder X-ray diffraction study (P-XRD)

The PXRD patterns of dry powder of SF, FD, SF, and FD physical mixture, SF-NFs, FD-SF-NFs (FD4), and FD loaded SF-NFs annealed with ethanol and water were obtained to study the crystallinity and possible polymorphic transformations (Figure 4). The diffractogram of dry powder SF (Figure 4a) has shown low-intensity diffraction peaks indicating amorphous nature<sup>[20,30]</sup>. The diffractogram of neat FD (Figure 4b) showed high intensity and sharp characteristic peaks at  $2\theta$   $11.09^{\circ}$ ,  $20.65^{\circ}$ ,  $23.18^{\circ}$ , and  $25.31^{\circ}$  revealing the crystalline nature of FD<sup>[7]</sup>. The diffractogram of the SF and FD physical mixture (Figure 4c) demonstrated a slight reduction in the intensity of the FD peak. Diffractogram of electrospun SF-NFs (Figure 4d) has shown broad hump-like diffraction peaks at ( $2\theta$ )  $20.6^{\circ}$ ,  $29.42^{\circ}$ , unlike SF, which are in partial agreement with the findings of Kim et al.<sup>[29]</sup>. This could divulge little crystallinity induction in SF-NF, due to the conversion of the random coil to the  $\beta$ -sheet conformation of SF<sup>[25–27,29]</sup>. In the case of FD-SF-NFs, all diffraction

peaks of FD were disappeared, whilst characteristic peaks of SF were predominant in the diffractogram. This confirmed molecular level dispersion of FD in the fibroin matrix, disrupting drug crystallinity. The PXRD spectra of FD-SF-NFs (FD4) formulation demonstrated a reduction in FD crystallinity (Figure 4e) and an increase in SF crystallinity due to the electrospinning process. Diffractogram of FD loaded SF-NFs annealed with ethanol (Figure 4f) and water (Figure 4g) showed broad and hump-like  $2\theta$  at  $20.6^{\circ}$  and  $29.42^{\circ}$  with enhanced intensity as observed in FD-SF-NFs, before annealing treatment. This could evince that crystallinity was induced due to vapor annealing treatment with ethanol and water. This might have happened due to the orientation of hydrophobic domains of fibroin toward the interior, while hydrophilic domains are exposed to hydrophilic annealing solvents. As the intensity of peaks observed in FD loaded SF-NFs annealed with ethanol was greater than FD loaded SF-NFs annealed with water, ethanol-induced crystallinity was more than water. This could be attributed to a difference in hydrophilicity of both annealing solvents.

#### 4.8. Scanning electron microscopy (SEM)

The SEM images of pristine FD-loaded SF-NFs show different types of the morphology of SF-NFs concerning their size and shape. Additionally, the data evinced that the various factor (electrospinning process and environmental) having a significant effect on the morphology of scaffolds<sup>[17]</sup>. It has been mentioned that the polymer concentration, molecular weight, surface tension of electrospinning solution plays an imperative role in NFs fabrication. In the present study, the optimized SF concentration was kept as a key parameter for the electrospinning process. The SF concentration (10% w/v) at constant optimized process parameters including voltage, temperature, current, etc, were demonstrated smooth, uniform, bead-less, and cylindrical surface morphology of SF-NFs (Figure 1a). The NFs size was found in the range of  $100.23\text{ nm}$  to  $335.79\text{ nm}$  (average diameter:  $218.01 \pm 2.54\text{ nm}$ ). Hence, it concludes that the optimized constant process parameter with SF optimized concentration has played a crucial role in the NFs fabrication process. SEM images for FD-SF-NFs (Figure 1b–d) shown that 10 mg loading of FD into SF solution with concentration range (10% w/v) did not affect significantly the surface morphology of electrospun NFs which concludes that there is good polymeric and drug dispersion in electrospinning solution. The FD-loaded SF-NFs images (Figure 1b–d) for batch FD1, FD2, and FD3 with an increase in spinneret speed showed the formation uniform, un-beaded morphology with an increase in NFs diameters of higher crystallinity, due to improved polymer chain alignment addition. The SEM image of FD-SF-NFs (FD4) (Figure 1e) with a decrease in flow rate showed the formation of uniform scaffolds with a decrease in average diameter. Whilst the SEM images for batch FD5 and FD6 (Figure 1f and g) shown a change in distance between collector drum and syringe not significantly affect and morphology and size of prepared scaffolds. Whereas, coagulated and eroded polymeric FD-SF-NFs, with



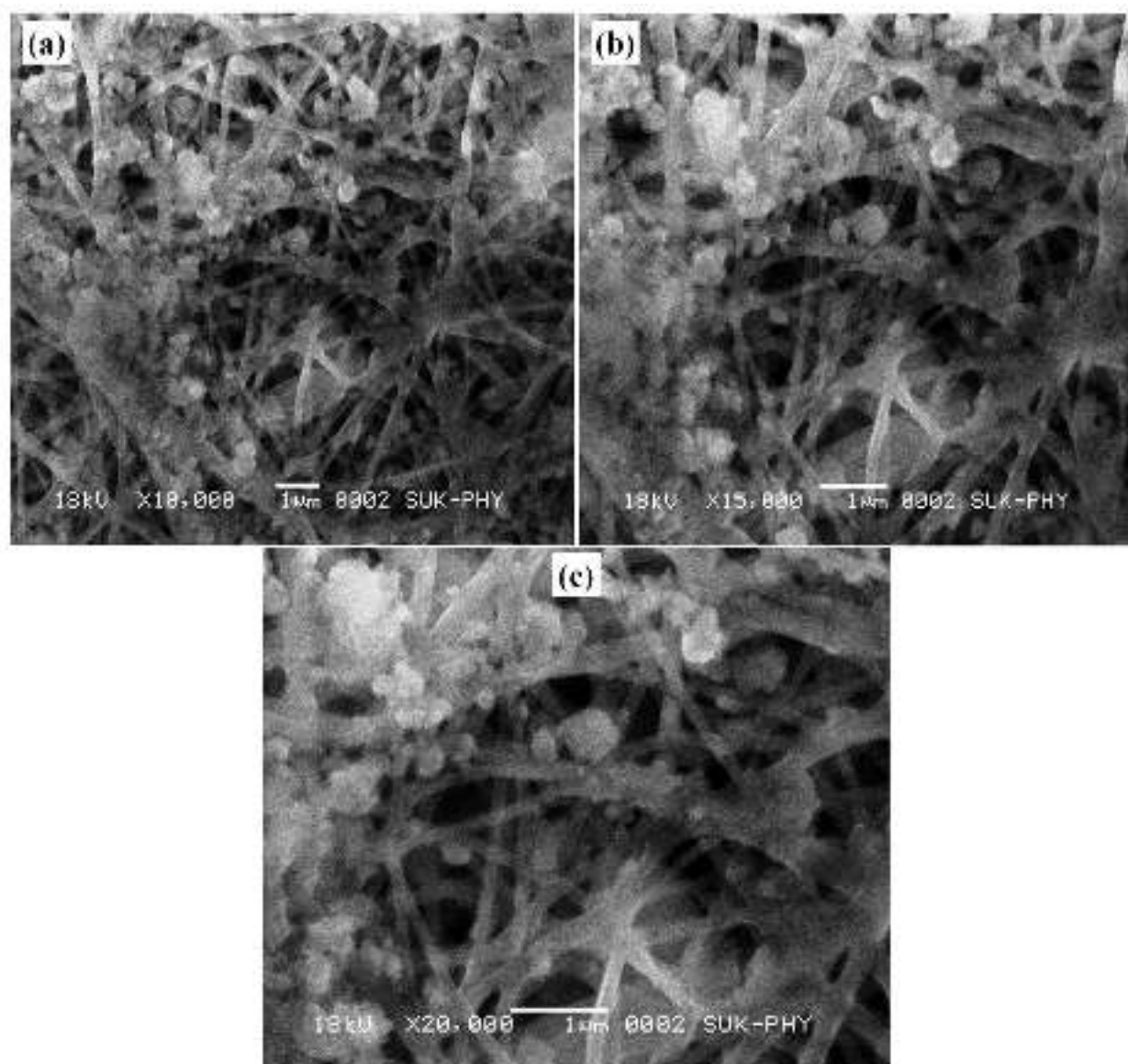


**Figure 5.** SEM images of post-dissolution study of FD-SF-NFs/FD4 (a–c).

uneven surface morphology, were observed after *in vitro* dissolution study (Figure 5a–c). The fibers were seen bridged during the dissolution process, as evident from the SEM images<sup>[27]</sup>.

#### 4.9. Percent entrapment efficiency and percent drug content

The amount of drug entrapped in polymeric carriers is called entrapment efficiency whereas drug content is the number of drugs available for the release of drugs in the drug delivery system. Therefore, percent entrapment efficiency is an important parameter for the delivery system. All the formulation batch FD loaded SF-NFs (FD1–FD6) was tested for percentage entrapment efficiency and percentage drug content. The result of FD-loaded SF-NFs is tabulated in Table 4. The batch FD4 showed significantly high percent entrapment efficiency compared to the other NFs batches (FD1, FD2, FD3, FD5, and FD6). In addition, the percentage

drug content of FD4 was found to be uniform in all dosage forms. Since dependent on the methods for drug incorporation, fibers with different morphologies are generated, which potentially impact drug distribution and thereof percent entrapment efficiency and percent drug content. In the present study, for all batches (FD1–FD6) drug was incorporated in the polymeric solution in the same way; whilst the electrospinning parameters for the formation of drug-loaded SF-NFs were changed to divulge the effect of electrospinning parameters on the crystallinity of SF-NFs. In the case of, of FD4 batch the flow rate was reduced leads to form SF-NFs with a decrease in diameters; evidenced by SEM image Figure 1e, and with a decrease in pore volume (least porosity) evidenced by (Table 4). Both pore volume and surface area played an imperative role in drug loading capacity and thereof on drug content of SF-NFs. Literature witnessed that enhanced porosity due to smaller pore size does not allow the drug to access the available surface area<sup>[31]</sup>. Thus, the FD4 batch with a narrow diameter, and hence with

**Table 4.** Data for drug entrapment efficiency, percent drug content, percent porosity, 0.1 N HCl uptake and swelling ratio of FD-SF-NFs.

Batch code	Drug content	Drug entrapment efficiency	Percent porosity	Uptake of 0.1NHCl	Swelling ratio
FD1	77.02 ± 0.45	42.05 ± 0.41	69.67 ± 0.53	81.09 ± 0.38	6.04 ± 0.34
FD2	61.05 ± 0.22	23.87 ± 0.91	67.02 ± 0.41	84.99 ± 0.72	4.03 ± 0.40
FD3	72.15 ± 0.45	51.06 ± 0.84	72.08 ± 0.59	83.08 ± 0.81	5.06 ± 0.44
FD4	74.52 ± 0.43	59.15 ± 0.57	52.41 ± 0.57	79.11 ± 0.42	3.15 ± 0.28
FD5	68.41 ± 0.39	33.06 ± 0.81	56.53 ± 0.63	85.12 ± 0.33	6.12 ± 0.26
FD6	82.21 ± 0.59	42.05 ± 0.34	60.08 ± 0.48	85.90 ± 0.54	6.72 ± 0.54

Note. Data are presented as mean ± SD (n = 3).

increased pore diameter with least porosity showed high percent entrapment efficiency and high drug content as compared with other batches having greater porosity with small pore size.

#### 4.10. Porosity, 0.1 N HCl uptake kinetics, and swelling study

The porosity, uptake kinetics, and swelling of material are interdependent phenomena. Porosity is the measure of the void spaces in the material, it imparts a significant effect on the swellability of the polymer. The porosity of SF and SF-NFs was found  $54.53 \pm 0.02$  and  $56.11 \pm 0.41$  respectively, whilst, the porosity of FD-SF-NFs (FD1-FD6) was in the range of  $52.41 \pm 0.57$  to  $72.08 \pm 0.59$  as were tabulated in Table 4. The percent porosity of FD-loaded SF-NFs (FD4) was found to be the least compared to others. HCl uptake ability and swelling ratio of FD-SF-NFs (FD4) was found to be the least amongst all. Overall, the data evinced the SF having significant porosity; but during the ES process, the configurationally changes in SF lead to the formation of NFs with greater porosity. The swelling behavior in polymeric nanocarrier used in drug delivery systems plays a crucial role for diffusion with both the penetrant into the matrix and the drug throughout the layer of the matrix<sup>[32]</sup>. The use of more than a single polymer in a nanocarrier system leads to enhancement in swelling property and also decreases the reproducibility in the release pattern of drug from the matrix system<sup>[11]</sup>. The experimental demonstration for 0.1 N HCl uptake and swelling ratio comes with findings that; SF has shown 0.1 N HCl uptakes and swelling ratio equivalent to  $80.79 \pm 0.07$  and  $5.02 \pm 0.56$ , respectively, whereas, SF-NFs showed  $86.13 \pm 0.81$  and  $4.85 \pm 0.92$ , respectively. The details of 0.1NHCl uptake and swelling ratio of FD-SF-NFs have been given in Table 4. Thus overall; porosity, 0.1 N HCl uptake kinetics, and swelling study data evinced that change in the electrospinning parameters tunes the crystallinity of scaffolds and thereof of the morphological structure of scaffolds like diameter of NFs, its pore size, etc. These morphological properties play an imperative role in porosity, 0.1 N HCl uptake kinetics, and swelling study of scaffolds and hence in modification of release profile drug<sup>[33]</sup>.

#### 4.11. Floating profile studies

Gastroretentive drug delivery systems require short floating lag time and long total floating time values<sup>[11]</sup> for excellent floating behavior. Thus, SF being a low-density polymer than the gastric fluid demonstrating excellent floating

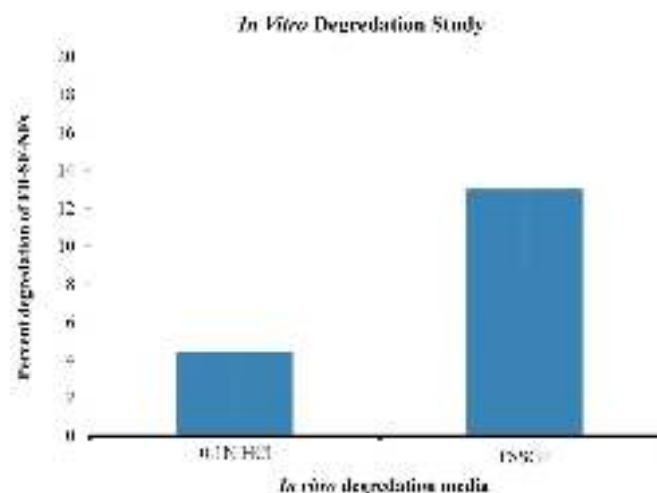


Figure 6. In-vitro degradation study of FD-SF-NFs in 0.1NHCl and FSSGF.

behavior<sup>[7]</sup>. The time required FD-loaded SF-NFs to rise to the surface and float was determined as floating lag time. All batches of FD-loaded SF-NFs floated within 10 s. The amount of FD-loaded SF-NFs (FD4) rose to the surface, compared to the initial amount of FD-loaded SF-NFs added, which was taken as percent buoyancy. The percent buoyancy of FD-loaded SF-NFs was found to be 98.05%w/w. The total floating time of FD-loaded SF-NFs NFs was found to be more than 12 h. In conclusion, FD-loaded SF-NFs being a low-density polymer than the gastric fluid demonstrating excellent floating behavior more than 12 h.

#### 4.12. In-vitro degradation study of FD loaded SF-NFs

For a close simulation of degradation of FD-loaded SF-NFs (FD4) in the body, *in vitro* degradation in FSSGF (enzymatic or hydrolysis) was carried out that revealed an additional 9% degradation takes place, compared to 0.1 N HCl (Figure 6). Enzymes play a significant role in the degradation of SF. Degradation of SF occurs due to adsorption of the enzyme and hydrolysis. The degradation behavior of SF is also influenced by other physiological factors like pH of fluid, molecular weight of SF, the chemical method used for extraction of SF, etc.<sup>[34]</sup>.

#### 4.13. Mucoadhesion test

Mucoadhesion is a promising strategy for controlled drug delivery. Regardless of the specific molecular mechanism, it may prove more effective than other controlled delivery's strategies based on, the intimate contact provided by the



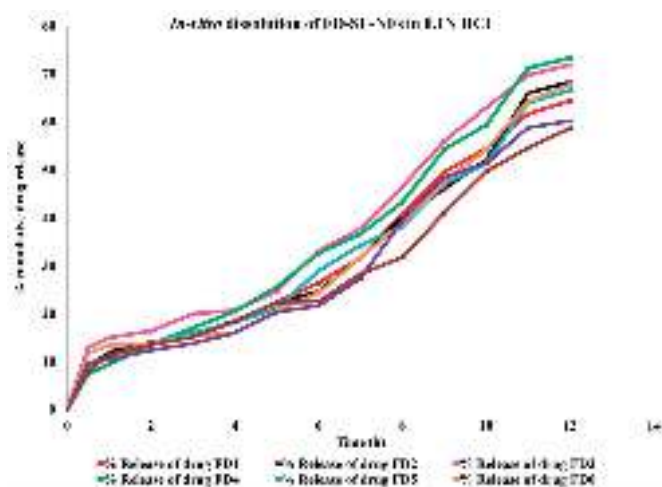


Figure 7. *In-vitro* dissolution study profile of FD-SF-NFs in 1.0 N HCl (dissolution media).

adhesive with an absorptive membrane, the enhanced retention at the site of action, the potential protection of sensitive biological molecules, and the improved bioavailability<sup>[13]</sup>. Interestingly, FD-SF-NFs sheet tested showed mucoadhesion time up to 8 h. whilst, mucoadhesion strength was found to be 2,520 g, and force of adhesion 24.72 N. Thus, FD-SF-NFs show satisfactory mucoadhesion, enabling the residence of the drug in the stomach for a reasonable time<sup>[35]</sup>. Since SF polar region consisting of proteoglycan and glycoproteins to adhere with the mucosal layer due to secondary bond interactions (hydrogen bonds and van der Waals interactions)<sup>[13]</sup>.

#### 4.14. *In-vitro* dissolution studies

From *In-vitro* dissolution studies, it was seen that FD-SF-NFs filled capsule shells were completely dissolved within 10–13 min, leaving behind NFs mat floated. The overall release of FD was found to be more from dissolution media FSSGF (Figure 7, pH 1.2), than 0.1 N HCl (Figure 8, pH 1.2), which might be due to significant NFs degradation in the former ( $p < 0.05$ ). In 0.1 N HCl, *in-vitro* dissolution studies revealed that optimized batch FD4 releases drug up to  $73.36 \pm 0.68\%$  in 12 h, as it had a low degree of crystallinity. After annealing with solvents (ethanol and water) degree of crystallinity increases; thus shows more retardation of the drug release. Interestingly, water-treated FD-SF-NFs showed drug release up to  $60.23 \pm 0.27\%$  and that of ethanol-treated  $58.65 \pm 0.85\%$ . Studies carried out in FSSGF demonstrated more FD release from batch FD4 ( $82.54 \pm 0.98\%$ ) and it followed USFDA guidelines for dissolution criteria of controlled release. The batch FD1 showed the lowest drug release ( $74.13 \pm 1.32\%$ ) as compared to other batches studied in FSSGF. It also showed that drug release from annealed FD-SF-NFs was also decreased in FSSGF, due to more crystallinity of NFs leading to more retardation of drug release in the dissolution media. Thus, tailoring the crystallinity SF NFs can be considered as a tool to customize drug release. To our surprise, the release of FD from all batches of FD-SF-NFs was found to follow a zero-order release. For

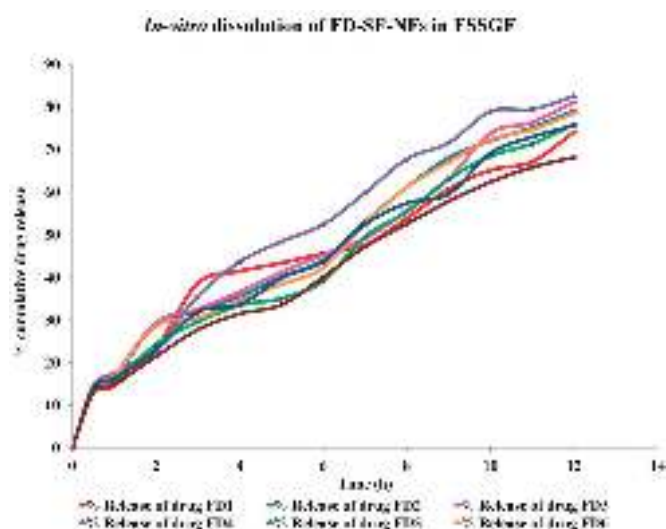


Figure 8. *In-vitro* dissolution study profile of FD-SF-NFs in 0.1 N FSSGF (dissolution media).

interpretation of the drug release mechanism, mainly three release parameters viz.  $n$ —release exponent;  $k$ —release rate constant;  $r^2$ —regression coefficient, were taken into account (Table 3). The best fit model was decided based on goodness of fit, describing the anomalous release as a combination of release, diffusion, and erosion<sup>[35]</sup>. Even, SEM images of FD-SF-NFs, taken post-dissolution, showing eroded and uneven surfaces could support the same findings. Thus, overall by observing various findings from *in vitro* studies, spectral and dissolution data it evidenced that the mechanism involved in the release of drug pointing toward diffusion and polymer degradation followed by erosion. Also, the dissolution studies of FD1–FD6 batch show a different amount of drug release depends upon the crystallinity of NFs, evinced that crystallinity of SF polymer matrix is also the control point of dissolution profiles. Since the crystallinity of SF is physicochemical properties having a significant effect on diffusion coefficient and thus the release exponent of SF<sup>[36]</sup>. *In vitro* data divulged that as the crystallinity of SF increases the rate of diffusion release profile approaches zero ordered (linear). In addition, the spectral studies evinced that ethanol and water annealing have also been used toward similar goals. Thus, by observing the relationship between these physicochemical properties and diffusion coefficients it became more clear that a more robust diffusion-based model can be formed to simulate release before experimentation and to determine optimal device formulations for desirable release patterns<sup>[36]</sup>.

## 5. Conclusion

The present work is a successful attempt to prepare crystallinity modulated SF-NFs floating scaffolds that demonstrating controlled drug release for 12 h, compliant with pharmacopeial specifications for extended-release dosage forms. Prepared electrospun scaffolds (FD1–FD6) show excellent percent entrapment efficiency and drug content with admirable porosity and swelling property for controlled release application. As an outcome of PAT, the role of

electrospinning parameters in altering the crystallinity of SF-NFs and thereby modified drug release has been elucidated the first time. FTIR study divulged that change in electrospinning parameters leads to conformational changes in SF and thereof the crystallinity of NFs, witnessed by shifting of wavenumber for amide I and amide II group respectively. Whilst thermal and diffractometric analysis revealed that molecular dispersion of FD, coupled with amorphous form stabilization in NFs. Additionally, crystallinity changes are also coupled with the annealing of NFs using a solvent like ethanol and water. Also, FD-SF scaffolds showed excellent floating profiles including floating time (total floating time up to 12 h), percent buoyancy (98.05% w/w), etc. In addition, mucoadhesion studies demonstrate the satisfactory mucoadhesion of FD-SF-NFs. *In vitro* dissolution study for all the scaffold batches, FD-loaded SF-NFs annealed with ethanol and water was performed in dissolution medium 0.1HCl and FSSGF. It reveals that optimized batch FD4 shows drug release up to (73.36 ± 0.68%) in 0.1 N HCl whereas (82.54 ± 0.98%) in FSSGF. Whilst, FD loaded SF-NFs annealed with ethanol and water showed more retardation of the drug; and hence less drug release in both mediums respectively due to conformational changes in SF from random coil to  $\beta$ -sheet during annealing treatment. *In vitro* study in FSSGF reveals that it shows more drug release than in 0.1 N HCl, as FSSGF contain enzymes that might cause the degradation of polymer SF allowed to more drug release from FD-SF-NFs scaffolds. Thus, the controlled release (12 h) of the FD from SF-NFs (devoid of other polymers) could be successfully modeled to zero-order type, despite reports on diffusion-based drug release from SF-NFs. Such NFs belong to FDDS of low-density type, which may have the least chances of failure due to sinking, as evident from floating profile studies data. Thus, tuned crystallinity, extraordinary environmental/storage polymeric stability, biodegradable and biocompatible nature, satisfactory mechanical strength, etc. may prove this system as a novel floating protein-based drug delivery system for controlled release application.

## Acknowledgment

The authors are thankful to Principal, Bharati Vidyapeeth College of Pharmacy, Kolhapur for providing the necessary facilities.

## Disclosure statement

The authors declare no conflict of interest.

## ORCID

Sarika Wairkar  <http://orcid.org/0000-0002-0124-1741>

## References

- [1] Bardonnet, P.; Faivre, V.; Pugh, W.; Piffaretti, J.; Falson, F. Gastroretentive Dosage Forms: Overview and Special Case of *Helicobacter pylori*. *J. Control Release* **2006**, *111*, 1–18. DOI: [10.1016/j.jconrel.2005.10.031](https://doi.org/10.1016/j.jconrel.2005.10.031).
- [2] Hooda, A. Gastroretentive Drug Delivery Systems: A Review of Formulation Approaches. *The Pharma. Innovation* **2012**, *1*, 79–707.
- [3] Gupta, P.; Gnanarajan, P. K. Floating Drug Delivery System: A Review. *Int. J. Pharm. Res. Rev.* **2015**, *4*, 37–44.
- [4] Bhavsar, D. N. Advances in GRDDS: Raft Forming System a Review. *J. Drug Deliv. Ther.* **2012**, *2*, 123–128.
- [5] Sharma, A. R.; Khan, A. Gastroretentive Drug Delivery System: An Approach to Enhance Gastric Retention for Prolonged Drug Release. *Int. J. Pharm. Sci. Res.* **2014**, *5*, 1095.
- [6] Garg, K.; Bowlin, G. L. Electrospinning Jets and Nanofibrous Structures. *Biomicrofluidics* **2011**, *5*, 13403. DOI: [10.1063/1.3567097](https://doi.org/10.1063/1.3567097).
- [7] Rathod, P.; More, H.; Dugam, S.; Velapure, P.; Jadhav, N. Fibroin-Alginate Scaffold for Design of Floating Microspheres Containing Felodipine. *J. Pharm. Innov.* **2021**, *16*, 226–236. DOI: [10.1007/s12247-020-09440-6](https://doi.org/10.1007/s12247-020-09440-6).
- [8] Malik, R.; Garg, T.; Goyal, A. K.; Rath, G. Polymeric Nanofibers: Targeted Gastro-Retentive Drug Delivery Systems. *J. Drug Target.* **2015**, *23*, 109–124. DOI: [10.3109/1061186X.2014.965715](https://doi.org/10.3109/1061186X.2014.965715).
- [9] Nangare, S.; Jadhav, N.; Ghagare, P.; Muthane, T. Pharmaceutical Applications of Electrospinning. *Ann. Pharm. Fr.* **2020**, *78*, 1–11. DOI: [10.1016/j.pharma.2019.07.002](https://doi.org/10.1016/j.pharma.2019.07.002).
- [10] Darbasizadeh, B.; Motasadizadeh, H.; Foroughi-Nia, B.; Farhadnejad, H. Tripolyphosphate-Crosslinked Chitosan/Poly (Ethylene Oxide) Electrospun Nanofibrous Mats as a Floating Gastro-Retentive Delivery System for Ranitidine Hydrochloride. *J. Pharm. Biomed. Anal.* **2018**, *153*, 63–75. DOI: [10.1016/j.jpba.2018.02.023](https://doi.org/10.1016/j.jpba.2018.02.023).
- [11] Tort, S.; Han, D.; Steckl, A. J. Self-Inflating Floating Nanofiber Membranes for Controlled Drug Delivery. *Int. J. Pharm.* **2020**, *579*, 119164. DOI: [10.1016/j.ijpharm.2020.119164](https://doi.org/10.1016/j.ijpharm.2020.119164).
- [12] Shitole, M.; Dugam, S.; Tade, R.; Nangare, S. Pharmaceutical Applications of Silk Sericin. *Ann. Pharm. Fr.* **2020**, *78*, 469–486. DOI: [10.1016/j.pharma.2020.06.005](https://doi.org/10.1016/j.pharma.2020.06.005).
- [13] Brooks, A. E. The Potential of Silk and Silk-like Proteins as Natural Mucoadhesive Biopolymers for Controlled Drug Delivery. *Front. Chem.* **2015**, *3*, 65.
- [14] Qi, Y.; Wang, H.; Wei, K.; Yang, Y.; Zheng, R.-Y.; Kim, I. S.; Zhang, K.-Q. A Review of Structure Construction of Silk Fibroin Biomaterials from Single Structures to Multi-Level Structures. *Int. J. Mol. Sci.* **2017**, *18*, 237. DOI: [10.3390/ijms18030237](https://doi.org/10.3390/ijms18030237).
- [15] Pignatelli, C.; Perotto, G.; Nardini, M.; Cancedda, R.; Mastrogiacomo, M.; Athanassiou, A. Electrospun Silk Fibroin Fibers for Storage and Controlled Release of Human Platelet Lysate. *Acta Biomater.* **2018**, *73*, 365–376. DOI: [10.1016/j.act-bio.2018.04.025](https://doi.org/10.1016/j.act-bio.2018.04.025).
- [16] Edgar, B.; Regårdh, C. G.; Lundborg, P.; Romare, S.; Nyberg, G.; Rönn, O. Pharmacokinetic and Pharmacodynamic Studies of Felodipine in Healthy Subjects after Various Single, Oral and Intravenous Doses. *Biopharm. Drug Dispos.* **1987**, *8*, 235–248. DOI: [10.1002/bdd.2510080305](https://doi.org/10.1002/bdd.2510080305).
- [17] Park, Y. R.; Ju, H. W.; Lee, J. M.; Kim, D.-K.; Lee, O. J.; Moon, B. M.; Park, H. J.; Jeong, J. Y.; Yeon, Y. K.; Park, C. H. Three-Dimensional Electrospun Silk-Fibroin Nanofiber for Skin Tissue Engineering. *Int. J. Biol. Macromol.* **2016**, *93*, 1567–1574. DOI: [10.1016/j.ijbiomac.2016.07.047](https://doi.org/10.1016/j.ijbiomac.2016.07.047).
- [18] Sony, A.; Jain, S. Formulation and Evaluation of Floating Microspheres of Flupirtine Maleate. *Int. J. Pharm. Life Sci.* **2013**, *4*, 2535–2540.
- [19] Hu, X.; Kaplan, D.; Cebe, P. Determining Beta-Sheet Crystallinity in Fibrous Proteins by Thermal Analysis and Infrared Spectroscopy. *Macromolecules* **2006**, *39*, 6161–6170. DOI: [10.1021/ma0610109](https://doi.org/10.1021/ma0610109).
- [20] Dhole, R.; Patil, U.; Jadhav, N. Stabilization of Hydrochlorothiazide Nanocrystals Using Fibroin. *Marmara Pharm. J.* **2019**, *23*, 997–1008.

- [21] Wang, A.; Xu, C.; Zhang, C.; Gan, Y.; Wang, B. Experimental Investigation of the Properties of Electrospun Nanofibers for Potential Medical Application. *J. Nanomater.* **2015**, *2015*, 1–8. DOI: [10.1155/2015/418932](https://doi.org/10.1155/2015/418932).
- [22] Begum, S. R.; Varma, M. M.; Raju, D.; Prasad, R.; Phani, A.; Jacob, B.; Salins, P. C. Enhancement of Dissolution Rate of Piroxicam by Electrospinning Technique. *Adv. Nat. Sci.: Nanosci. Nanotechnol.* **2012**, *3*, 045012. DOI: [10.1088/2043-6262/3/4/045012](https://doi.org/10.1088/2043-6262/3/4/045012).
- [23] Prasanth, A. G.; Kumar, A. S.; Shruthi, B. S.; Subramanian, S. Kinetic Study and in Vitro Drug Release Studies of Nitrendipine Loaded Arylamide Grafted Chitosan Blend Microspheres. *Mater. Res. Express* **2020**, *6*, 125427. DOI: [10.1088/2053-1591/ab5811](https://doi.org/10.1088/2053-1591/ab5811).
- [24] Karade, P. G.; Jadhav, N. R. Colon Targeted Curcumin Microspheres Laden with Ascorbic Acid for Bioavailability Enhancement. *J. Microencapsul.* **2018**, *35*, 372–380. DOI: [10.1080/02652048.2018.1501111](https://doi.org/10.1080/02652048.2018.1501111).
- [25] Magoshi, J.; Magoshi, Y.; Nakamura, S.; Kasai, N.; Kakudo, M. Physical Properties and Structure of Silk. V. Thermal Behavior of Silk Fibroin in the Random-Coil Conformation. *J. Polym. Sci. Polym. Phys. Ed.* **1977**, *15*, 1675–1683. DOI: [10.1002/pol.1977.180150915](https://doi.org/10.1002/pol.1977.180150915).
- [26] Magaz, A. n.; Roberts, A. D.; Faraji, S.; Nascimento, T. R.; Medeiros, E. S.; Zhang, W.; Greenhalgh, R. D.; Mautner, A.; Li, X.; Blaker, J. J. Porous, Aligned, and Biomimetic Fibers of Regenerated Silk Fibroin Produced by Solution Blow Spinning. *Biomacromolecules* **2018**, *19*, 4542–4553. DOI: [10.1021/acs.biomac.8b01233](https://doi.org/10.1021/acs.biomac.8b01233).
- [27] Liu, Z.; Zhang, F.; Ming, J.; Bie, S.; Li, J.; Zuo, B. Preparation of Electrospun Silk Fibroin Nanofibers from Solutions Containing Native Silk Fibrils. *J. Appl. Polym. Sci.* **2015**, *132*, 41236. DOI: [10.1002/app.41236](https://doi.org/10.1002/app.41236).
- [28] Le, T.-T.; Elyafi, E.; Khaliq, A.; Mohammed, A. R.; Al-Khattawi, A. Delivery of Poorly Soluble Drugs via Mesoporous Silica: Impact of Drug Overloading on Release and Thermal Profiles. *Pharmaceutics* **2019**, *11*, 269. DOI: [10.3390/pharmaceutics11060269](https://doi.org/10.3390/pharmaceutics11060269).
- [29] Kim, S. H.; Nam, Y. S.; Lee, T. S.; Park, W. H. Silk Fibroin Nanofiber. Electrospinning, Properties, and Structure. *Polym. J.* **2003**, *35*, 185–190. DOI: [10.1295/polymj.35.185](https://doi.org/10.1295/polymj.35.185).
- [30] Ki, C. S.; Lee, K. H.; Baek, D. H.; Hattori, M.; Um, I. C.; Ihm, D. W.; Park, Y. H. Dissolution and Wet Spinning of Silk Fibroin Using Phosphoric Acid/Formic Acid Mixture Solvent System. *J. Appl. Polym. Sci.* **2007**, *105*, 1605–1610. DOI: [10.1002/app.26176](https://doi.org/10.1002/app.26176).
- [31] Bavnhoj, C. G.; Knopp, M. M.; Madsen, C. M.; Löbmann, K. The Role Interplay between Mesoporous Silica Pore Volume and Surface Area and Their Effect on Drug Loading Capacity. *Int. J. Pharm. X.* **2019**, *1*, 100008. DOI: [10.1016/j.ijpx.2019.100008](https://doi.org/10.1016/j.ijpx.2019.100008).
- [32] Nangare, S. N.; Dugam, S. S.; Patil, P. O.; Tade, R. S.; Jadhav, N. Silk Industry Waste Protein: Isolation, Purification and Fabrication of Electrospun Silk Protein Nanofibers as a Possible Nanocarrier for Floating Drug Delivery. *Nanotechnology* **2021**, *32*, 035101. DOI: [10.1088/1361-6528/abb8a9](https://doi.org/10.1088/1361-6528/abb8a9).
- [33] Luo, Z.; Zhang, Q.; Shi, M.; Zhang, Y.; Tao, W.; Li, M. Effect of Pore Size on the Biodegradation Rate of Silk Fibroin Scaffolds. *Adv. Mater. Sci. Eng.* **2015**, *2015*, 1–7. DOI: [10.1155/2015/315397](https://doi.org/10.1155/2015/315397).
- [34] Cao, Y.; Wang, B. Biodegradation of Silk Biomaterials. *Int. J. Mol. Sci.* **2009**, *10*, 1514–1524. DOI: [10.3390/ijms10041514](https://doi.org/10.3390/ijms10041514).
- [35] Mottaghitlab, F.; Farokhi, M.; Shokrgozar, M. A.; Atyabi, F.; Hosseinkhani, H. Silk Fibroin Nanoparticle as a Novel Drug Delivery System. *J. Control Release* **2015**, *206*, 161–176. DOI: [10.1016/j.jconrel.2015.03.020](https://doi.org/10.1016/j.jconrel.2015.03.020).
- [36] Hines, D. J.; Kaplan, D. L. Mechanisms of Controlled Release from Silk Fibroin Films. *Biomacromolecules* **2011**, *12*, 804–812. DOI: [10.1021/bm101421r](https://doi.org/10.1021/bm101421r).